Process Control Applications in Microbial Fuel Cells(MFC)

by

Rakesh Joshi

A Dissertation Presented in Partial Fulfillment
of the Requirements for the Degree
Doctor of Philosophy

Approved April 2018 by the
Graduate Supervisory Committee:

Konstantinos Tsakalis, Chair
Armando Rodriguez
Cesar Torres
Andreas Spanias

ARIZONA STATE UNIVERSITY

May 2018

ABSTRACT

Microbial fuel cells(MFC) use micro-organisms called anode-respiring bacteria(ARB) to convert chemical energy into electrical energy. This process can not only treat wastewater but can also produce useful byproduct hydrogen peroxide(H_2O_2). Process variables like anode potential and pH play important role in the MFC operation and the focus of this dissertation are pH and potential control problems.

Most of the adaptive pH control solutions use signal-based-norms as cost functions, but their strong dependency on excitation signal properties makes them sensitive to noise, disturbances, and modeling errors. System-based-norm(H_∞) cost functions provide a viable alternative for the adaptation as they are less susceptible to the signal properties. Two variants of adaptive pH control algorithms that use approximate H_∞ frequency loop-shaping (FLS) cost metrics are proposed in this dissertation.

A pH neutralization process with high retention time is studied using lab scale experiments and the experimental setup is used as a basis to develop a first-principles model. The analysis of such a model shows that only the gain of the process varies significantly with operating conditions and with buffering capacity. Consequently, the adaptation of the controller gain (single parameter) is sufficient to compensate for the variation in process gain and the focus of the proposed algorithms is the adaptation of the PI controller gain. Computer simulations and lab-scale experiments are used to study tracking, disturbance rejection and adaptation performance of these algorithms under different excitation conditions. Results show the proposed algorithm produces optimum that is less dependent on the excitation as compared to a commonly used L_2 cost function based algorithm and tracks set-points reasonably well under practical conditions. The proposed direct pH control algorithm is integrated with the combined activated sludge anaerobic digestion model (CASADM) of an MFC and it is shown pH control improves its performance.

Analytical grade potentiostats are commonly used in MFC potential control, but, their

high cost (>$6000) and large size, make them nonviable for the field usage. This dissertation proposes an alternate low-cost($\approx$ $200) portable potentiostat solution. This potentiostat is tested using a ferricyanide reactor and results show it produces performance close to an analytical grade potentiostat.

To my father and mother, who encouraged me to pursue doctorate degree in engineering.

To my brother for his constant support.

ACKNOWLEDGEMENTS

I owe my gratitude to all the people who have advised, assisted, encouraged or inspired me during the course of this work. While dedicating a few words to them in this brief chapter would do little justice to their support, I must mention that I will forever be indebted to them.

I am very grateful to my advisor, Dr. Konstantinos Tsakalis for guiding me through out my research. His constant support, suggestions, and patience helped me towards the greater understanding of the control theory. I am thankful to Dr. Sachi Dash and Dr. J Ward MacArthur for helping me understand pH control processes and for having very insightful discussions with me. I am also grateful to SERDP team, Dr Cesar Torres, Dr Bruce Rittmann, Dr Sudeep Popat, Michelle N. Young and Dr Dongwon Ki for introducing me to microbial fuel cells and for their constant guidance in the lab. I am very thankful to my committee members Dr. Armando Rodriguez and Dr. Andreas Spanias for their guidance, time and support for my research. Their exceptional co-operation helped me with a smoother dissertation process.

I would also like to thank my friends Dr. Ashfaque Bin Shafique, Dr. Victoria Rodriguez, Garett Scott, Yiqiu Liu, Vishwam Aggarwal, Dapan Saha and Vignesh Raghuraman for having intense intellectual discussions. I am thankful to many other faculty in Arizona State University, who made a significant impact on my learning process.

My special thanks to my current room-mates and former roommates Jagjot, Manveer, Iknoor, Hiten and Jaspreet for their support and giving me a leg up whenever I was feeling down.

Monetary support for this work has been provided by the SERDP environmental restoration project 2239.

TABLE OF CONTENTS

CHAPTER Page

LIST OF TABLES

LIST OF FIGURES

Figure Page

Figure Page

Figure Page

Figure Page

Chapter 1

INTRODUCTION

1.1 Microbial fuel cells

Global warming has become an existential crisis for humanity and the usage of fossil fuel has accelerated this crisis. To solve this crisis it is important to decrease the carbon footprint by moving away from fossil fuels to renewable energy sources. Different forms of renewable energy sources like solar, wind and bio-energy fuels have been explored as a potential replacement for fossil fuels. One such source is the organic waste like activated sludge, black water(BW) and livestock manure. Anaerobic digestion is widely used to break organic waste to produce CH_4, that can be used to generate heat or electricity[43]. Microbial fuel cells (MFC) are one such anaerobic digestion mechanism that converts bio-fuel(like wastewater) into energy source.

In MFC, anaerobic digestion converts chemical energy present in the organic matter into electric current with the help of microorganisms called anode-respiring bacteria (ARB)[36]. The ARB form a biofilm that enables electron transfer to the anode from organic materials, such as glucose, ethanol, acetic acid, wastewater, animal wastes, and others during oxidation. These electrons pass through an external circuit and at the cathode, they reduce O_2. The type of oxygen reduction reaction depends upon the cathode material and catalysts. To maximize electricity production metal catalysts can be used, where $4e^-$ reduction of O_2 of produces H_2O. However, metal catalysts are expensive. Alternatively, relatively less expensive electrodes like carbon cathodes can be used to carry out $2e^-$ reduction of O_2 to produce a useful byproduct H_2O_2.

$$O_2 + 2e^- + 2H^+ \quad \rightarrow \quad H_2O_2 \tag{1.1}$$

This $2e^-$ reaction produces less current as compared to $4e^-$ however it requires relatively

less expensive material and produces useful byproduct H_2O_2.

The strong oxidizing properties of H_2O_2 makes it a very useful chemical in the wastewater treatment process as it is can be readily used in the tertiary treatment and disinfection of the treated water. This property makes it a more useful MFC output in the wastewater treatment process as compared to other outputs like electricity or H_2 gas. Also, this H_2O_2 production method is less toxic as compared to traditional H_2O_2 production methods and it also saves chemical transportation costs.

There is a growing interest in the use of MFC with the domestic wastewater as a fuel. This setup not only helps in the treatment of the wastewater but also produces electricity. Papers [69][38],[37], [39] and [13] provide a good review on MFC with the wastewater as fuel. Utilization of MFC in the production of hydrogen peroxide is discussed in [16][51][5][12][44] and a schematic diagram of one such MFC with hydrogen peroxide production is shown in Fig. 1.1.

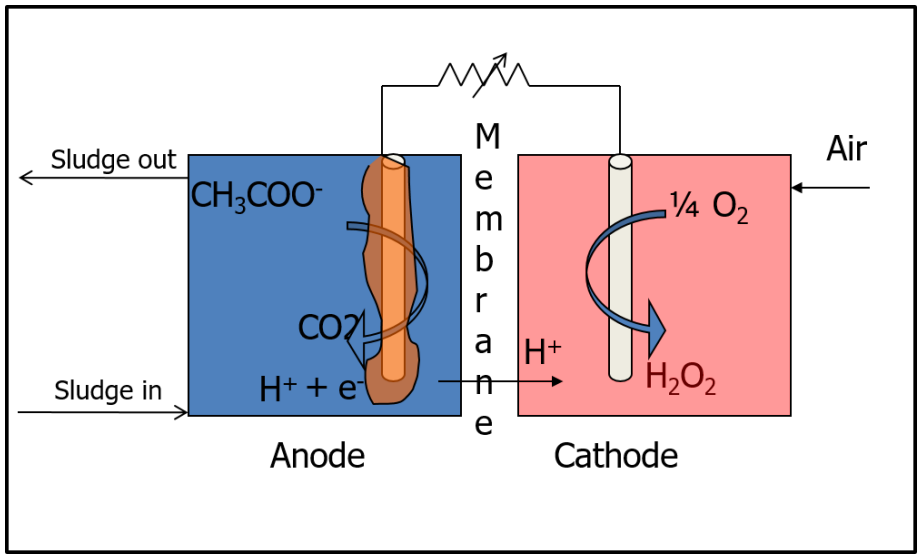

Figure 1.1: Schematic diagram of an MFC for hydrogen peroxide generation

The oxidation reaction carried by ARB in an MFC produce current and releases $[H^+]$ into the anode. This results in a decrease in the anode pH, which in turn inhibits the performance of an MFC [60]. So to improve the efficiency of an MFC anode operation, it is very important to control pH in the anode at the desired set-point. The effect of pH on

an MFC operation and the desired optimal pH values are described in [49], [52], [40],[41] and[48]. Similarly, electrode potentials also play an important role in the production of hydrogen peroxide in an MFC [51]. This work focus on the study of pH and potential control problems. Introduction of these control problems is discussed in the following sections.

1.2 pH control

The pH control plays an important role in various industrial processes. Some of its applications include wastewater treatment, biotechnology processes, and electrochemical cells. Because of its highly nonlinear nature and its dependence on exogenous signals (e.g., time-varying buffer concentrations), pH control of a wastewater treatment process is a very challenging process control problem. These characteristics also make it a benchmark problem to test nonlinear controllers [2].

The nonlinear nature of the process implies that linear controllers are ineffective to control pH over a wide range and the time-varying nature of certain problems make it futile to control even around a given pH value [32][33]. There are different versions of nonlinear controllers proposed, for example [20], [34], [1], [17] and [28], to name a few. However, it is shown in [28] the nonlinear control algorithms fail to compensate the time-varying behavior (buffering capacity) and thereby making adaptive control the best-suited solution.

Adaptive control is an extensively researched area and there are many adaptive control schemes studied in the literature. Some of them are gain scheduling and multi-model adaptive control [58][4][29][30][3], model reference adaptive control and indirect adaptive control, e.g., [54], [31].

Different versions of adaptive control schemes have been proposed for pH control and we briefly discuss the more relevant ones below. [19] considers the usage of gain-scheduling, adaptive control for the bio-reactors, in which controllers are scheduled using pH and carbon dioxide measurements. A nonlinear adaptive pH control method is described in [28], that uses a nonlinear model of the process and estimate of the variation of buffer flow rate from the online data to perform feedback linearization. [47] and [9] discuss the usage of

indirect multi-model adaptive control and indirect adaptive schemes. These methods collect plant input-output data during closed-loop operation, over an interval of the open-loop time constant, to fit a linear model and use the linear model to update controller parameters. An improved version of multi-model adaptive control for the noisy environment is presented in [8]. All these versions either rely on a nonlinear model with a parameter estimator or a local linear model estimated using online data. They all use some version of signal-based adaptation cost metric derived from the online data for the estimation or selection of the controller parameters and a general form of such metric can be written as follows

$$\theta^* = arg \min_{\theta} J(C(\theta); x) \tag{1.2}$$

Where $C(\theta)$ denotes controller with parameters θ, x denotes measured signals and $J(C(\theta); x)$ is the cost function used in the adaptation. Typical cost functions are the mean square error or exponentially weighted mean square error, where the error represents the difference between expected and actual(ex. predication error, control error etc.). Optimization of these cost functions produce optimal performance if the signals are persistently exciting and there is no noise or disturbances. However, perturbations such as sensor noise and disturbances result in a cost function whose minimum can be significantly different depending on the signals at hand (e.g., see [65]). In such a case, the result is often poor performance or adaptation bursts since the parameter adaptation cannot keep up with the variation of the disturbances. Furthermore, the worst-case performance depends on the parametric uncertainty and the problem is not easily detected with a "noisy simulation".

In an effort to design an adaptation cost functional that provides a better description of our control objective, hence resulting in a weaker dependence on signal properties, we propose the approximation of the norm of an error system(not signal). Our ultimate objective is to achieve comparable performance to the off-line designs under reasonable practical conditions. Although we cannot expect that such a goal is achievable without some constraints, e.g., on excitation and operating conditions, we do allow for the possibility of setting up monitoring conditions under which good performance can be expected, or,

alternatively, conditions offering no guarantees and which may require the use of a "safe" controller. A key instrument in our effort is the use of normalized metrics that describe the gain of a suitable error operator, instead of the more customary signal errors that are often used in adaptive control and that are prone to errors under weak excitation conditions. A general description of one such cost functional can be broadly described as follows

$$\theta^* = arg \min_{\theta} \max_{x} J(C(\theta); x) \tag{1.3}$$

The above structure allows us to describe cost functional in terms of the worst-case behavior and the selection of the controller parameters that produces minimum worst-case behavior. Motivated by the results of the H_∞ robust control theory, we consider the decomposition of the cost function in terms of the frequency components of the signal x:

$$\theta^* = arg \min_{\theta} \max_{j} J(C(\theta); x_j) \tag{1.4}$$

where now x_j represents the energy of measured signals at different frequency directions and $J(\cdot)$ is a system norm. The former can be achieved under a linearity assumption by processing the input and output signals through a "filter bank" (FB), an example of which is shown in Fig. 1.2. Thus, the proposed approach enables the approximation of a H_∞ cost functional using a single data sequence. In this manner, the signal decomposition may only approximate its frequency content, but it is exact at all times and does not suffer the usual windowing effects of Fast Fourier transforms (FFT). On the other hand, a system norm computation would require the normalization of the system output RMS power by the corresponding input power, something that is achievable by requiring excitation that is persistent and of sufficient magnitude. This is not a major problem as excitation is often present in practical problems, or can be requested for short time periods, and can at least be verified by a monitoring program before adapting the controller parameters. The same monitoring logic can also limit the use of excitation directions to the ones that contain sufficient excitation, e.g., through the use of an adaptation dead-zone. It is our view that the critical part of the adaptive control is the ability of the adaptation to take advantage

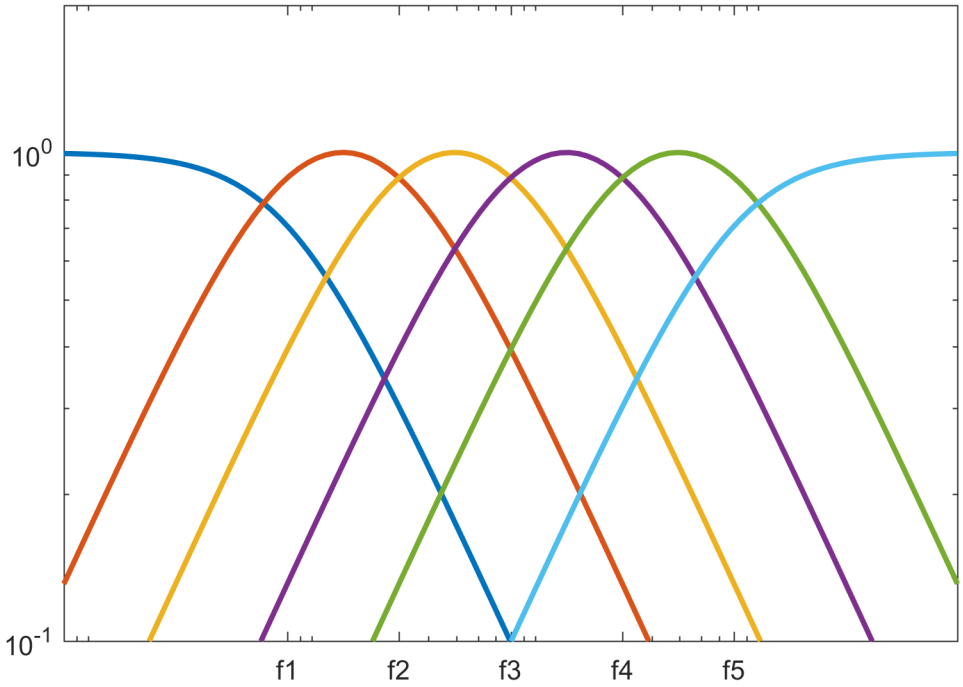

Figure 1.2: Bode diagram of a filter bank

of short or occasional excitation periods in the most efficient way, instead of attempting to operate with the least assumptions but opening the door to undesirable nonlinear behavior like bursting.

Interest in multi-model adaptive control (MMAC) has gained traction significantly in recent past. In this scheme, the controller used in the closed-loop system is selected from a bank of controllers based on metrics derived from online data. In a brief review, the theoretical framework of the data-driven MMAC algorithms seeking robust stability and safe switching is discussed in [58], [10], [11], [53]. A multi-variable MMAC algorithm using an estimator and a controller that can tolerate structural uncertainties is discussed in [59]. The application of MMAC in pH control is discussed in [9] and refinement of this algorithm for a noisy environment is discussed in [8]. All these MMAC methods use error signals that represent prediction or control error or their combination, to compute the metric used in the controller switching and their cost functionals are signal-norms (L_2 or L_∞) of the error

signals. This dissertation discusses the development of an alternative to the usual update laws that is based on the approximation of system norms as cost functionals, instead of signal norms.

Taking motivation form the above-described system norm metric (Eq. 1.4), H_∞ metric derived from the on-line data is used in the selection of the controller from a bank of controllers C_i and it can be written in a general form as follows

$$C^* = arg \min_{C_i} \max_j J(C_i; x_j) \tag{1.5}$$

where now x_j represents the energy of measured signals at different frequency directions and $J(\cdot)$ is a system norm. Frequency decomposition of signals can be done similar to the Eq. 1.4 using filter banks.

The motivating application for this work is the development of adaptive pH control algorithms that can be readily extended to pH control of microbial fuel cell (MFC) anode. The experimental setup with high retention time and with variable buffer flow mimics the MFC anode, therefore the adaptive control algorithms developed for this reactor can be readily extended to the MFC anode case. In our recent papers [32] and [33], it was shown for a given practical problem, essentially only the gain of the system changes with the operating point and that nonlinear/adaptive control is necessary to control pH. One standard adaptive control method used in the industry is gain-scheduling, in which controllers are scheduled based on a measured signal. In the MFC problem, pH is the only available measurement but the process gain depends also on the buffering capacity of the system. As a result, scheduling based only on the pH measurement is not sufficient to compensate for time-variations in the buffers. An example of such a gain-scheduling scheme failure using the model in Chapter 2 with variation in buffing capacity is shown in Fig. 1.3

Controllers with proportional-integral-derivative (PID) structure are commonly used in the process control industry. PID tuning is a very well researched topic and some of commonly used methods are discussed in [6] [7] [50]. There is a large number of publications with PID tuning methods for a variety of academic and industrial applications. Some of

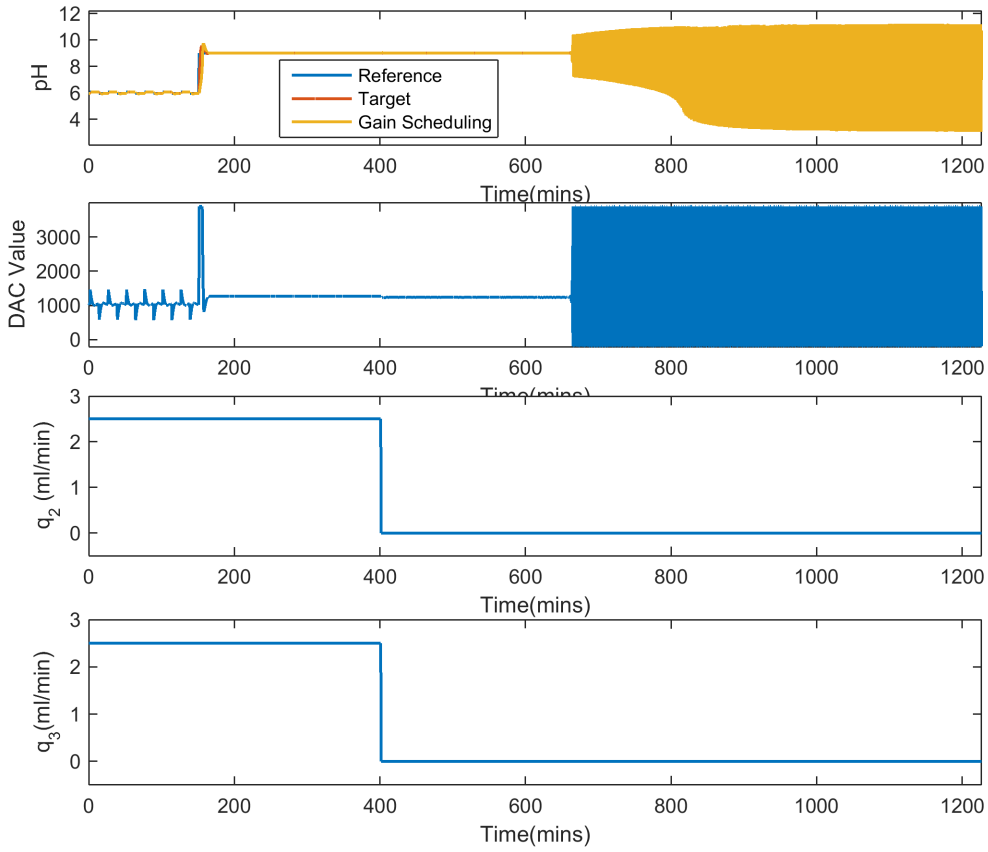

(a)

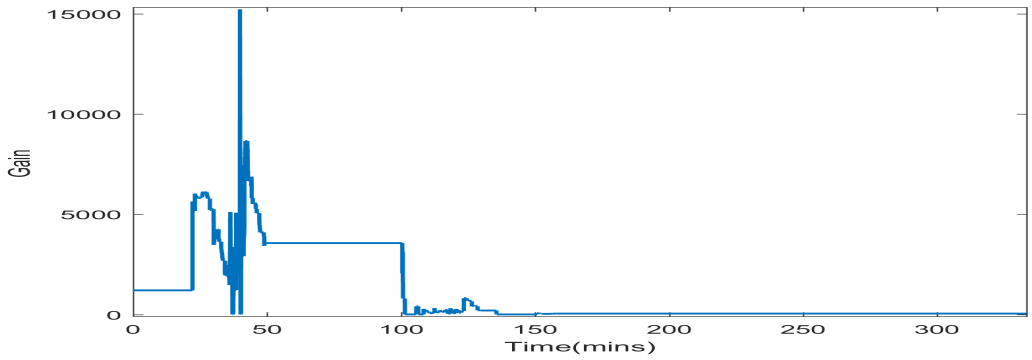

(b)

Figure 1.3: Closed-loop results for gain scheduling controller (a)input-output plot (b) controller gain plot. Here, there is a changing buffering capacity that causes the process gain to increase without a reduction of the controller gain. The instability is due to the discrete implementation of the high gain controller. This scenario is practically meaningful since a conservative controller tuning to stabilize all possible plants would have very sluggish response at the rest of the operating conditions.

them use lower order approximation of plant model like [68] [21] and others solve PID tuning as an optimization problem with a time or frequency domain performance measure [27] [45]. Even though low dimensionality of the PID tuning makes it a tractable problem, because of vast applications it is still a very actively researched field with a constant stream of publications. For this work we have chosen PID tuning using frequency loop shaping (FLS) as it is well defined in terms of robust control and also can be easily extended for the online adaptation of PID parameters.

Over the past two decades, we have employed the FLS approach for PID controller tuning with excellent results in a variety of practical problems. In a PID FLS parameter tuning, control systems specifications are described in terms of a target loop and PID parameters are tuned by minimizing a H_∞ distance measure(RSC) between the actual and the target loop. Examples of offline FLS PID tuning for continuous time systems using this distance measure is described in [62] [23] [25][22] [24] and for discrete-time systems is discussed in [56]. Computation of this distance measure using online data for the PID parameter adaptation is described in [67] and for the performance monitoring is discussed in [61]. The adaptive control algorithms described in this dissertation use RSC computed from the online data to tune PI controller parameters used in pH control. Outline of pH control part of this dissertation is described below.

First, the pH neutralization process used in the lab scale experiment is modeled using reaction invariants and the model is analyzed thoroughly at different pH operating points and including variation in the buffer flows. It is shown that only the gain of the process changes significantly and it is only necessary to adapt the controller gain in order to maintain good closed-loop performance throughout the entire operating range. Second, an RSC-based direct adaptive control algorithm is proposed for pH control. Test results from computer simulations and experimental evaluation under "sufficiently excitating inputs" are presented. Advantages of system-norm based adaptation over commonly used L_2 signal based adaption is demonstrated for the pH control using results from the computer

simulations. Third, a so-called "multi-model adaptive control" (MMAC) variant of the adaptive controller is proposed. In this, the same RSC metric is optimized but the controller is selected from a discrete set of controllers. The test results from computer simulations indicate that reasonable and comparable performance is obtained, as long as the set of controllers is sufficiently dense to contain an appropriate controller for all possible gains of the plant. Fourth, application of the proposed pH control solution for a CASADM model ([70]) is carried out using computer simulations and it is shown pH control improves the efficiency of the MFC operation. Finally, a summary of observations and concluding remarks on the industrial implementation of adaptive pH control is presented.

1.3 Potential control

The anode potential plays an important role in the operation of an MFC [16] [51] and a potentiostat is a device that helps in controlling electrode potentials at their desired values. Commercially available analytical grade potentiostats are expensive with the cost of one unit around $6000. Analytical grade potentiostats are widely used in research labs and offer excellent control performance, which is often an "overkill" for an industrial application. They are rarely used in the field because the practical limitations on performance (noise, disturbances) do not justify their high cost and large size. In the recent past, some researchers have proposed low-cost potentiostat alternatives [15] and [46]. These potentiostats use op-amps to drive potentials of the cell and use analog to digital (A/D) and digital to analog (D/A) channels of an embedded microcontroller to measure or to adjust set-points. Some drawbacks of these potentiostat designs are their low current rating and low measured signal accuracy. In this work, we developed a low-cost potentiostat solution that can deliver high current and can read electrode potentials with higher accuracy as compared to other low-cost solutions. We tested our potentiostat and compared it against an analytical grade potentiostat (BioLogic Science Instruments-VMP3). It is shown the proposed potentiostat results in a performance comparable to BioLogic Science Instruments-VMP3 potentiostat. It is further tested with a 1 ohm resistor and it is

shown potentiostat follows voltage set-points with a current delivery of 1 amp. Construction and implementation details of this potentiostat along with results from experimental testing are presented in Chapter 7.

Chapter 2

ANALYSIS OF PH NEUTRALIZATION PROCESS

This chapter focuses on the construction of a first-principles model(mass balance and charge balance) of the pH neutralization process that represents the lab experimental setup. It also presents an analysis of this model, where the nonlinear model is linearized around different operating points(pH) and for variations in buffering capacity.

2.1 Reaction Invariant Model

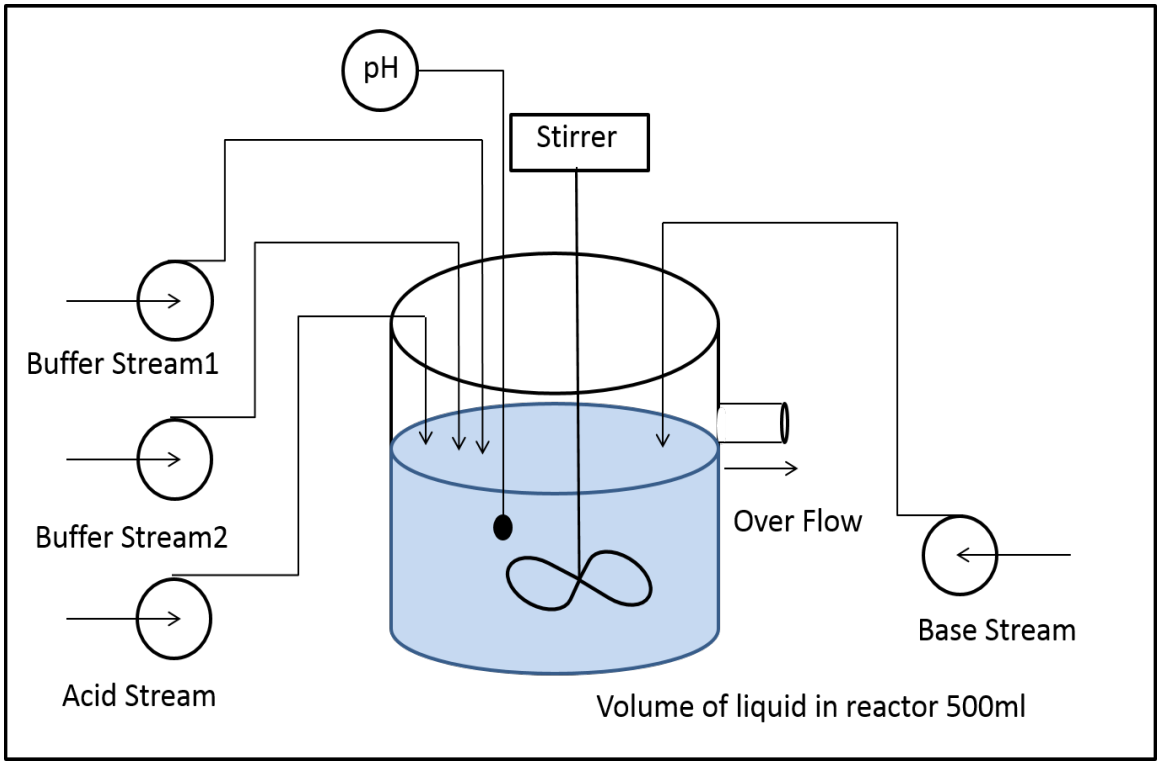

Figure 2.1: Schematic diagram of pH neutralization process CSTR

Consider a 500mL-continuous stirred tank reactor (CSTR) with inlet streams of strong acid ($1M\ HCl$), weak acid 1($100mM\ H_2CO_3$), weak acid 2 ($100mM\ H_3PO_4$) and strong base ($1M\ NaOH$) and q_1,q_2,q_3 and q_4 being their flow rates respectively. The schematic

diagram of the reactor is shown in Fig. 2.1 . The combination of strong acid, weak acid 1 and weak acid 2 simulates a waste water and flow rate of the strong base is manipulated to control the pH of the liquid in the reactor. A variation of the buffering capacity of the wastewater is simulated by varying flow rates of the weak acids. The volume of the liquid in the reactor and its temperature are kept constant. The pH of the liquid in the reactor is measured directly by a pH probe inserted into the reactor. It is assumed that perfect mixing occurs in the reactor and ions are completely soluble. The goal of pH control is to regulate pH of the liquid in the reactor by manipulating the base flow rate. The reaction invariant model is developed using reaction invariants of the reversible reaction components

The reversible reactions in the CSTR are listed below

$$H_2CO_3 \leftrightarrow H^+ + HCO_3^- \tag{2.1}$$

$$HCO_3^- \leftrightarrow H^+ + CO_3^{2-} \tag{2.2}$$

$$H_3PO_4 \leftrightarrow H^+ + H_2PO_4^- \tag{2.3}$$

$$H_2PO_4^- \leftrightarrow H^+ + HPO_4^{2-} \tag{2.4}$$

$$HPO_4^{2-} \leftrightarrow H^+ + PO_4^{3-} \tag{2.5}$$

$$H_2O \leftrightarrow H^+ + OH^- \tag{2.6}$$

Reaction constants of the above reversible reactions are stated below

$$Ka_1 = \frac{[HCO_3^-][H^+]}{[H_2CO_3]} \tag{2.7}$$

$$Ka_2 = \frac{[CO_3^{2-}][H^+]}{[HCO_3^-]} \tag{2.8}$$

$$Ka_3 = \frac{[H_2PO_4^-][H^+]}{[H_3PO_4]} \tag{2.9}$$

$$Ka_4 = \frac{[HPO_4^{2-}][H^+]}{[H_2PO_4^-]} \tag{2.10}$$

$$Ka_5 = \frac{[PO_4^{3-}][H^+]}{[HPO_4^{2-}]} \tag{2.11}$$

$$K_w = [H^+][OH^-] \tag{2.12}$$

The pH of the solution is the negative logarithm of the hydrogen ion concentration:

$$pH = -log_{10}([H^+]) \tag{2.13}$$

The chemical equilibrium is modeled based on the concept of reaction invariants [26] [42][28]. Three reaction invariants (W_a is a charge-related quantity, W_b refers to the concentration of carbonate ions and, W_c refers to the concentration of phosphate ions) are involved for each stream (i = 1 to 4) in this system. The analytic expressions of the reaction invariants are listed below

$$\begin{aligned} W_{ai} &= [H^+]_i - [OH^-]_i - [HCO_3^-] - 2[CO_3^{2-}] \\ &\quad -[H_2PO_4^-] - 2[HPO_4^{2-}] - 3[PO_4^{3-}] \end{aligned} \tag{2.14}$$

$$W_{bi} = [H_2CO_3] + [HCO_3^-] + [CO_3^{2-}] \tag{2.15}$$

$$\begin{aligned} W_{ci} &= [H_3PO_4] + [H_2PO_4^-] + [HPO_4^{2-}] \\ &\quad +[PO_4^{3-}] \end{aligned} \tag{2.16}$$

The relationship between hydrogen ion concentration and reaction invariants is given as follows:

$$\begin{aligned} W_{ci}\frac{\frac{K_{a3}}{[H^+]} + \frac{2K_{a3}K_{a4}}{[H^+]^2} + \frac{3K_{a3}K_{a4}K_{a5}}{[H^+]^3}}{1 + \frac{K_{a3}}{[H^+]} + \frac{K_{a3}K_{a4}}{[H^+]^2} + \frac{K_{a3}K_{a4}K_{a5}}{[H^+]^3}} \\ +W_{bi}\frac{\frac{K_{a1}}{[H^+]} + \frac{2*K_{a1}K_{a2}}{[H^+]^2}}{1 + \frac{K_{a1}}{[H^+]} + \frac{K_{a1}K_{a2}}{[H^+]^2}} \\ +W_{ai} + \frac{K_w}{[H^+]} - [H^+] = 0 \end{aligned} \tag{2.17}$$

A dynamic model for the pH neutralization process can be derived from the component material balance for the reaction invariants (W_{a5}, W_{b5} and W_{c5}) and the algebraic equation relating the pH and reaction invariants. The nonlinear process model can be described by mass- and charge-balance equations (Eq. 2.18 - 2.20) and algebraic equations (Eq. 2.17

Table 2.1: Model parameters

Symbol	Value	Symbol	Value
K_{a1}	4.47×10^{-7}	W_{a3}	$-0.181M$
K_{a2}	5.62×10^{-11}	W_{a4}	$-1M$
K_{a3}	0.0072	W_{b1}	$0M$
K_{a4}	1.6982×10^{-7}	W_{b2}	$0.1M$
K_{a5}	2.6915×10^{-12}	W_{b3}	$0M$
q_1	$2.45ml/min$	W_{b4}	$0M$
q_2	$2.45ml/min$	W_{c1}	$0M$
q_3	$2.4051ml/min$	W_{c2}	$0M$
q_4	$2.4051ml/min$	W_{c3}	$0.1M$
W_{a1}	$1M$	W_{c4}	$0M$
W_{a2}	$-0.1M$	V	500 ml

and Eq.2.13).

$$\begin{aligned}
\frac{dW_{a5}}{dt} &= \frac{1}{V}[q_1(W_{a1} - W_{a5}) + q_2(W_{a2} - W_{a5}) \\
&\quad +q_3(W_{a3} - W_{a5}) + +q_4(W_{a4} - W_{a5})] \qquad (2.18) \\
\frac{dW_{b5}}{dt} &= \frac{1}{V}[q_1(W_{b1} - W_{b5}) + q_2(W_{b2} - W_{b5}) \\
&\quad +q_3(W_{b3} - W_{b5}) + +q_4(W_{b4} - W_{b5})] \qquad (2.19) \\
\frac{dW_{c5}}{dt} &= \frac{1}{V}[q_1(W_{c1} - W_{c5}) + q_2(W_{c2} - W_{c5}) \\
&\quad +q_3(W_{c3} - W_{c5}) + +q_4(W_{c4} - W_{c5})] \qquad (2.20)
\end{aligned}$$

Nominal operating conditions of the plant are listed in Table 2.1 and a delay of 10 seconds is introduced to account for transportation and sensor quantization. In lab setup, a peristaltic pump is used to pump base into the reactor and its flow rate is controlled by varying voltage across the control terminal. The pump is interfaced with the microcontroller using a digital to analog converter (DAC). The DAC converts digital signal between 1-4095(12-bit resolution) from the microcontroller to 0-5V signal. The relation between

the base stream flow rate and DAC value is described by the following equation.

$$Baseflow(mL/min) = 7.45 \times \frac{DACValue}{4095} \tag{2.21}$$

Hereafter, plant input means DAC value and plant output means the pH of the liquid in the reactor. Analysis of this model for pH control is discussed in the next section.

2.2 Analysis of reaction invariant model

To analyze the nonlinear model for pH control it is linearized at different operating pH set points and buffer flow combinations. Various buffer flow rate combinations used to simulate variation in buffering capacity are listed below.

- Case 1: $q_2 = 2.5mL/min$ and $q_3 = 2.5mL/min$
- Case 2: $q_2 = 0mL/min$ and $q_3 = 2.5mL/min$
- Case 3: $q_2 = 2.5mlL/min$ and $q_3 = 0mL/min$
- Case 4: $q_2 = 0mL/min$ and $q_3 = 0mL/min$

Titration curves of all above-listed cases are shown in Fig. 2.2 and it can be seen from these plots titration curve becomes steep with the decrease in the buffer. For example titration curve for Case 4 is steeper than titration curve for Case 1. This variation in the steepness is significant with the change in the buffer flow, which results in the variation in the gain of the system.

The nonlinear system described in Eq. 2.20 is not completely observable (similar to the nonlinear model described in [28]). When we linearize the nonlinear model the minimal realization is just a first order, to which we add a delay to represent computer sampling and sensor delay and the apparent delay in the pump response. The transfer function of the linearized plants can be represented in a generalized form as below

$$P(s) = \frac{K_g}{\tau s + 1} e^{(-s/6)} \tag{2.22}$$

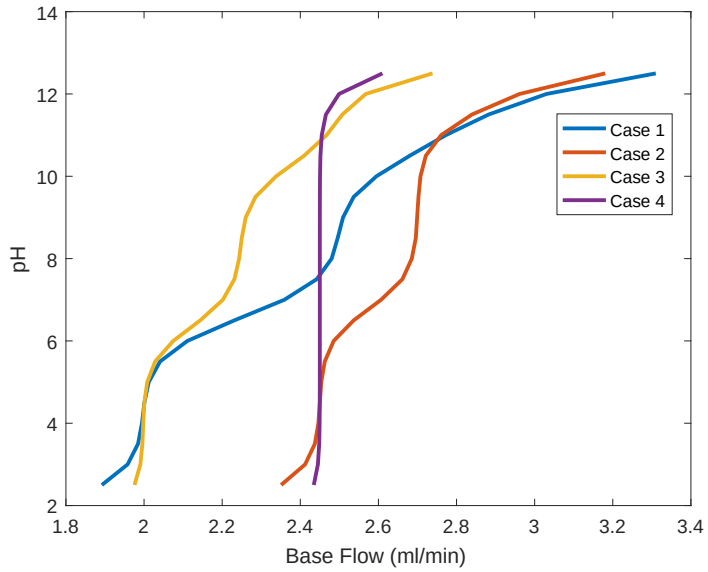

Figure 2.2: Titration curves of all buffer flow cases

where K_g is the gain and τ is the time constant of the linearized plant, respectively. The values of the gain of the linearized plant for all cases are listed in Table 2.2 and the values of the time constants are listed in the Table 2.3. The gain of linearized plants is shown in Fig. 2.3 and the time constant is shown in Fig. 2.4, visualizing their variation with pH and buffering capacity.

The gain values of the linearized plants are directly related to the slope of the titration curve. It can be seen from Table 2.2 and Fig. 2.3, that the gain of the linearized plant is a function of the operating pH and the buffering capacity of the liquid in the reactor. The gain variation with respect to operating pH and buffering capacity is large as expected from the titration curve plots. On the other hand, the time constant of the plant is directly related to the retention time. The variation in the time constant is minimal as compared to the process gain and the minimum time constant of all linearizations is 47 min. Consequently, for a controller design with the specification of settling time of 10 min or lower, the variation in the time constant has little impact on the loop performance and can be neglected in the formulation of the adaptive control problem.

This expectation is also supported by the comparison of the transfer functions of the

Table 2.2: Gain K_g of the linearized plants

	Gain			
pH	Case 1	Case 2	Case 3	Case 4
3.0	0.0193	0.0213	0.0994	0.1526
4.0	0.1282	0.1636	0.4123	1.5210
5.0	0.0498	0.1610	0.0704	35.9761
6.0	0.0103	0.0263	0.0128	69.6918
7.0	0.0075	0.0138	0.0174	69.7730
8.0	0.0392	0.0545	0.1095	69.6889
9.0	0.0484	0.3299	0.0564	35.9785
10.	0.0115	0.0994	0.0105	1.5188
11.0	0.0069	0.0170	0.0191	0.1468
12.0	0.0044	0.0084	0.0098	0.0098

Table 2.3: Time constants τ of the linearized plant

	Time Constant			
pH	Case 1	Case 2	Case 3	Case 4
3.0	53.1465	67.9129	71.0399	102.1428
4.0	52.9397	67.6015	70.9637	102.0510
5.0	52.8431	67.5333	70.8576	102.0418
6.0	52.2959	67.2452	70.1771	102.0409
7.0	50.9721	66.1652	68.9114	102.0408
8.0	50.3507	65.4839	68.5080	102.0407
9.0	50.2038	65.3668	68.3452	102.0398
10.0	49.7766	65.2938	67.6048	102.0306
11.0	48.9110	64.8451	66.4113	101.9388
12.0	47.7088	63.2002	65.5113	101.0275

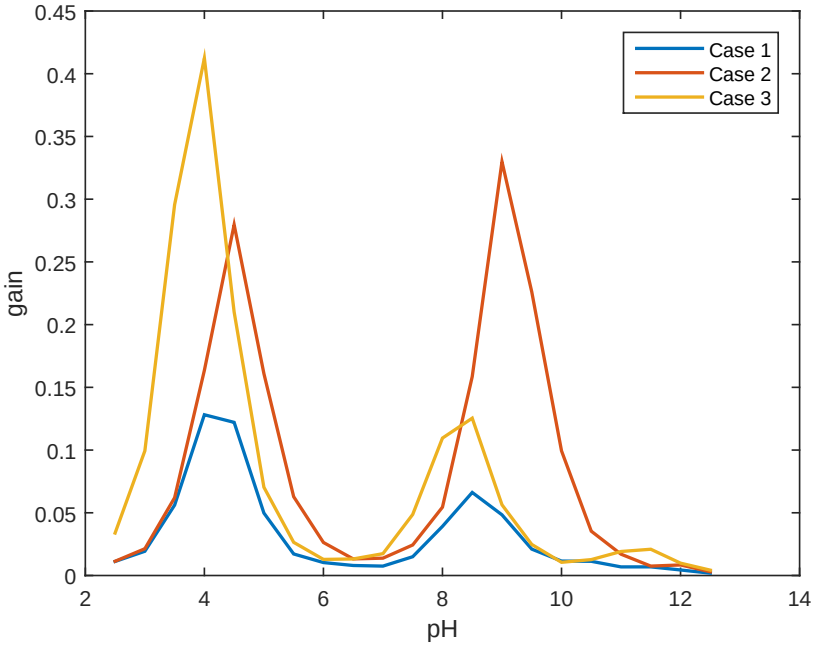

Figure 2.3: pH vs gain plot

linearized models with gain normalization at low frequency and at high frequency, as shown in Fig. 2.5 and Fig. 2.6. Thus, we expect that the adaptation of the controller gain alone will be sufficient to compensate for the significant gain variation of the plant, as long as the loop bandwidth (or crossover frequency) is clearly above or clearly below the retention dynamics (corner frequencies).

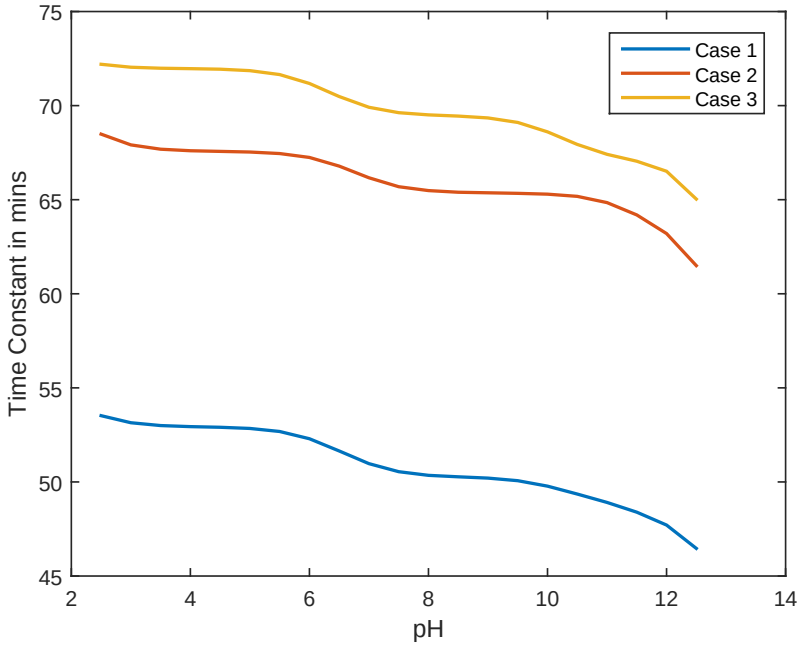

Figure 2.4: pH vs time constant

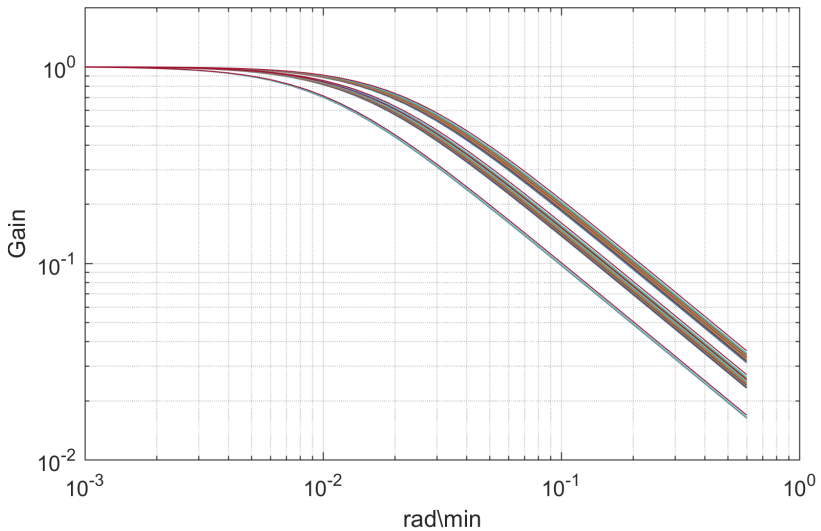

Figure 2.5: Bode magnitude plots of low frequency normalized plants ($\frac{G(s)}{G(0)}$); Other than the corner frequencies, all plants can be made to look similar at low frequency by scalar scaling

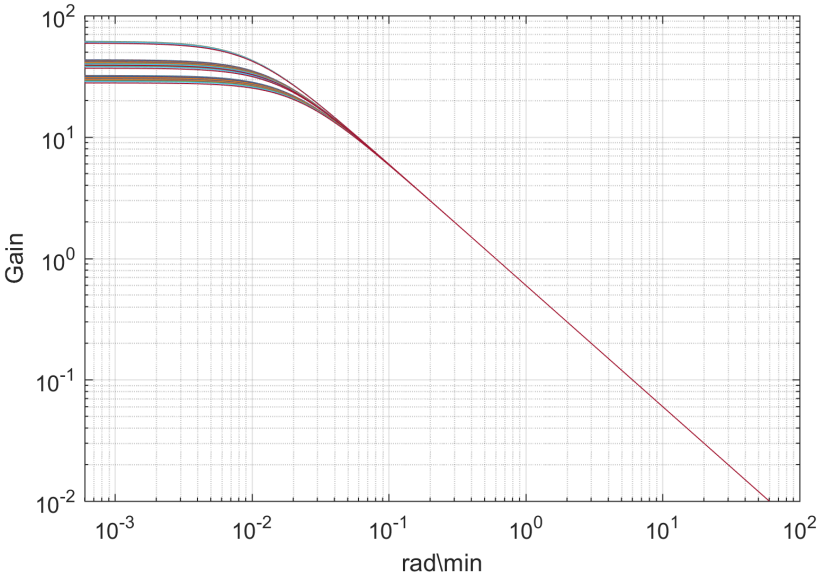

Figure 2.6: Bode magnitude plots of high frequency normalized plants ($\frac{G(s)}{|G(j0.6)|}$); Other than the corner frequencies, all plants can be made to look similar around an intended crossover frequency by scalar scaling. We conclude that simple gain adaptation is feasible, either for low or high frequency bandwidths.

Chapter 3

DIRECT CONTROLLER GAIN ADAPTATION FOR PH CONTROL

3.1 Direct adaptive pH Control algorithm

In this section we summarize the formulation of controller gain adaptation as an approximate $H\infty$ loop shaping problem [67] and discuss the necessary modifications for the practical implementation of this algorithm in the pH control problem. For the tuning of the PID parameters, we adopt the frequency loop shaping (FLS) approach, with an RSC metric described in [23].

Proportional integral derivative (PID) controllers are commonly used algorithms in the process industry. PID tuning is a very well researched topic and some of the commonly used methods are discussed in [6] [7] [50] and one such method is frequency loop shaping(FLS). In FLS, closed-loop design specifications are specified in terms of a target open-loop transfer function and PID parameters are obtained by minimizing the distance between the target loop and the actual open-loop transfer function. A weighted H_∞ norm called robust stability condition(RSC) metric provides a good measure of the distance between the actual and the target loop. Derivation of the RSC using the small gain theorem is discussed in Appendix A.

In a brief overview, in FLS the controller design specifications are expressed in terms of a target loop transfer function and PID parameters are obtained by minimizing the distance between the target loop and the actual open-loop transfer function. More specifically, letting G be the plant and C the controller, the FLS objective is to minimize the distance between the loop transfer function GC and the target loop L. A frequency-weighted version of this distance is obtained by the application of the small gain theorem, yielding the robust stability condition (RSC)

$$\|S(GC - L)\|_\infty < 1 \tag{3.1}$$

Where $S = 1/(1 + L)$ is the target sensitivity. The left-hand side of Eq. 3.1 can be interpreted as a particular closed-loop-relevant distance between the nominal and actual loops and $\|S(CG - L)\|_\infty$ is the FLS optimization objective. A desirable feature of this RSC metric is that it is normalized such that a value less than 1 guarantees closed-loop stability. Furthermore, while it is not explicitly a robust performance metric, small values of the RSC (e.g., 0.1-0.2) indicate a close matching between the nominal and the actual loop sensitivities.

Consider, next, a parameterization of the PID controller as

$$C(s) = K_p + \frac{K_i}{s} + \frac{K_d s}{(\tau s + 1)} \tag{3.2}$$

where K_p, K_i, K_d are the proportional, the integral and the derivative gains, respectively, and τ is the time constant of the filter used in the implementation of derivative control and its value is chosen a priori. For this PID parameterization, the RSC minimization problem is convex, and, in fact, linear in the parameters. Expression of the FLS as an RSC minimization of L_∞ for the PID tuning is given below.

$$\theta^* = arg \min_{\theta \in M} ||S(GC(\theta) - L)||_\infty \tag{3.3}$$

where θ represents PID parameters(K_p, K_i, K_d) and M is a constraint parameter set.

Clearly, the target loop L selection is an important component of FLS tuning and it should not violate the performance limitations imposed by right half-plane zeros and poles. It should also be reasonable to be approximated by a limited degree of freedom PID controller. Controller design methods like linear quadratic regular (LQR) or Glover–McFarlane H_∞ loop shaping [18] can be used to design higher order controllers for given specifications like bandwidth and the target loop can be constructed using this higher order controller and the plant transfer function. In this way, we can automate target selection process and when used in FLS, it approximates higher-order controller with a lower order PID controller.

The offline FLS algorithm for PID tuning can be formulated as a RSC minimization problem [62] [23]. The quality of the controller design can be assessed by looking at the

optimal RSC value if the value is less than 1 then the stability of the closed-loop system is guaranteed and lower values of optimal RSC implies the actual loop-performance closer to the target. The convergence of the FLS method to reasonable PID tunings, as compared to standard methods in the literature, e.g., [6] [7] [50], has been established in [23].

An extension of the offline FLS tuning to an online and adaptive implementation has been introduced in the paper[67], while the applicability and usage of the RSC metric in the performance monitoring of industrial process controllers has been discussed in [61]. The main idea in these applications was the estimation of the RSC values of Eq. 3.3 using plant input-output data. Letting (u, y) be the input-output pair of the plant and e be the error signal defined as $e = S(CG - L)u$, invoking the fact that $y = Gu$, we obtain $e = SCy - Tu$. Thus, the RSC can be expressed in terms of input-output data as follows

$$RSC = ||S(GC - L)||_\infty = \sup_{||u|| \neq 0} \frac{||e||_2}{||u||_2} \tag{3.4}$$

where $T = LS$ is target complementary sensitivity. The estimation of the RSC value in Eq. 3.4 can be approximated by the decomposition of the error signal e and the plant input u into frequency components by using two filter banks (FB) of band-pass filters F_i:

$$RSC \approx \max_i \frac{||SCF_i y - TF_i u||_2}{||F_i u||_2}$$

To improve the computational properties of the RSC estimate, we can further write an upper bound of the RSC in terms of the exponentially weighted norm $||x||_{2,\delta} = \{\int_{-\infty}^{\infty} e^{2\delta t}|x|^2(t)dt\}^{\frac{1}{2}}, \delta > 0$, for which it follows that

$$RSC \quad \leq \quad \max_i \frac{||SCF_i y - TF_i u||_{2,\delta}}{||F_i u||_{2,\delta}} \tag{3.5}$$

This approximation is similar to an FFT decomposition of the signal when the filter bank is composed of sharp bandpass filters. On the other hand, it does not suffer from the circular convolution problems of the FFT and is "exact" for a linear plant describing the input-output relationship (u, y). The significance of this observation is that the setup of the problem allows for the possibility of convergence of the adaptation to the matching

solution. In the ideal case of a linear plant controllable by a PI controller, this convergence can be achieved essentially irrespective of the data length or its frequency content. One can, therefore, expect the convergence of the tuning to a reasonably close value under small perturbations, resulting in a robust controller that can be easily quantified. Of course, the issue of persistence of excitation remains, as with any adaptive controller, which in our case we address by means of an external supervisory loop and an appropriate definition of the performance limitations.

We should also notice at this point that the computation of the fractions in Eq. 3.5 require that the denominators do not vanish, that is, the signal u is persistently exciting and wide-band. This assumption can be relaxed by allowing the combination of groups of filter outputs so that their total energy is bounded away from zero.

Finally, an advantage of the expression given by Eq. 3.5 is that the ratio of the exponentially weighted norms can be computed as the ratio of the respective squared signals, filtered by $1/(s+2\delta)$, and as such, it does not diverge for large intervals and does not require periodic resetting.

Next, and according to our model analysis, the process dynamics (pole, delay) change very little with the operating conditions and only gain of the system changes significantly. This observation enables us to restrict adaptation to a single parameter(controller gain) without sacrificing performance. For gain adaption, the PI controller can be expressed as follows

$$C(s) = K\frac{(s+a)}{s} = K\widetilde{C} \tag{3.6}$$

with the zero "a" estimated and fixed based on the preliminary data. The FLS tuning objective now is to determine the controller gain (K) so that open loop transfer function CG is close to target L in a weighted L_∞ sense. The FLS tuning from Eq. 3.3 now becomes

$$K^* = arg\min_{K\in M} ||S(GK\widetilde{C} - L)||_\infty \tag{3.7}$$

where $S = (1+L)^{-1}$ is the target Sensitivity and M is the set of controller gain values, i.e., the closed interval $M = [K_{min}, K_{max}]$, where K_{min} is the minimum controller gain and

K_{max} is the maximum controller gain. Block diagram of this controller is shown in Fig. 3.1

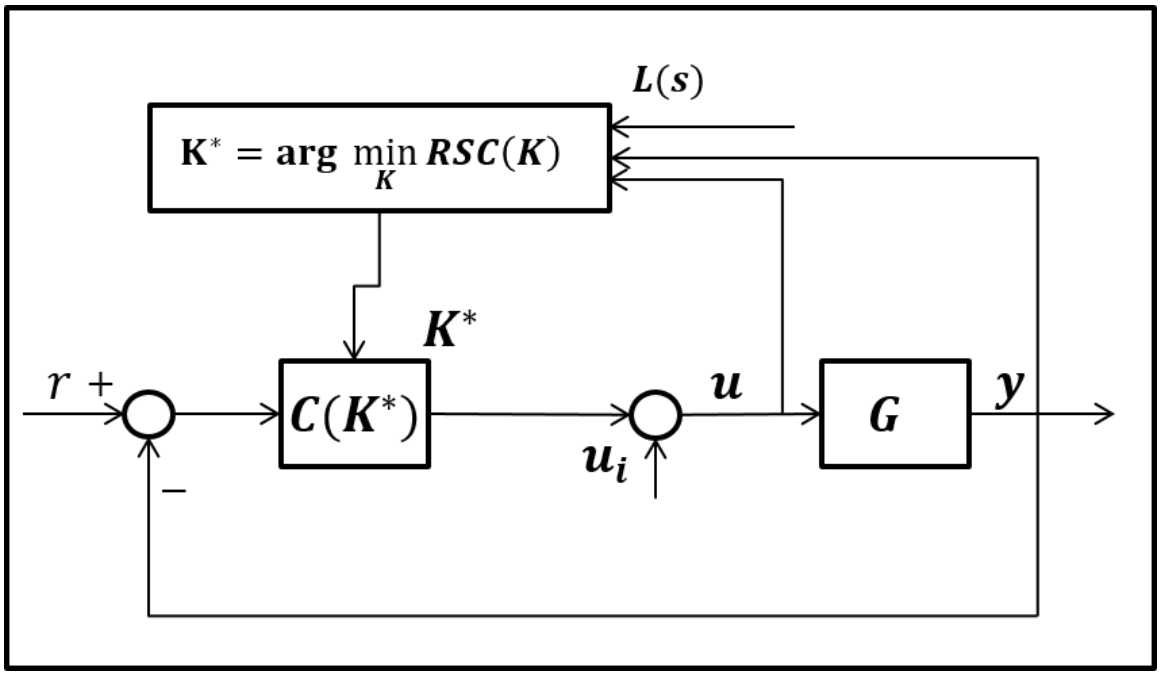

Figure 3.1: Block diagram of the closed-loop system with direct adaptive pH controller

For its online implementation, Eq. 3.7 is approximated by the minimization of the RSC estimate as described by means of a filter bank $\{F_i\}_i$ to generate a decomposition of the input and output signals and is given below.

$$K = arg \min_{K \in M} \max_{i} \frac{||KS\widetilde{C}F_i y - TF_i u)||_{2,\delta}}{||F_i u||_{2,\delta}} \tag{3.8}$$

The optimization problem in Eq. 3.8 is solved iteratively by computing the following at each time step k:

$$\min_{K \in M} \max_{i} \frac{J_{i,k}}{m_{i,k}} \tag{3.9}$$

$$\begin{aligned} J_{i,k}(K_k) &= \sum_{n=0}^{k} \lambda^{k-n} |z_{i,n} - w_{i,n}^T K_k|^2 \\ m_{i,k+1} &= \lambda m_k + |[F_i u]_{k+1}|^2 \end{aligned}$$

where $z_{i,n} = [TF_i u]_n$, $w_{i,n} = [S\widetilde{C}F_i y]_n$ and λ is forgetting factor, corresponding to the

discretized, exponentially weighted norm $(2, \delta)$ of Eq. 3.8. There are many optimization solvers readily available to solve the above optimization problem, one such solver is described in [67] and a brief summary of that solver is described below

$$\begin{aligned}
\hat{J}_{i,k+1} &= \lambda J_{i,k+1}(K_k) + (z_{i,k+1} - w_{i,k+1}K_k)^2 \\
J_{i,k+1}(\Delta K_{k+1}) &= \hat{J}_{i,k+1} - S_{i,k+1}\Delta K_{k+1} + \frac{1}{2}P_{i,k+1}\Delta K_{k+1}^2 \\
R_{i,k+1} &= \lambda R_{i,k} + 2z_{i,k}w_{i,k} \\
P_{i,k+1} &= \lambda P_{i,k} + 2w_{i,k}^2 \\
S_{i,k+1} &= \lambda R_{i,k} - P_{i,k+1}K_k
\end{aligned}$$

where $\hat{J}_{i,k+1}$ is a prior partial cost, $J_{i,k+1}(\Delta K_{k+1})$ is a partial cost functional at the time instance $k+1$ parameterized using $\Delta K_{k+1} = K_{k+1} - K_k$. $-S$ and P are the gradient and the Hessian of the functional J. A descent direction is computed using the following equation.

$$\begin{aligned}
\Delta \hat{K}_{k+1}^* &= \frac{\sum_{i \in I} \frac{S_{i,k+1}}{m_{i,k+1}}}{\sum_{i \in I} \frac{P_{i,k+1}}{m_{i,k+1}}} \\
\Delta K_{k+1}^* &= Proj_M(\Delta \hat{K}_{k+1}^*)
\end{aligned} \tag{3.10}$$

Where $Proj_M$ is the projection of $\hat{K}_{k+1}^*$ into the set M. The set I consists of all indices of prior partial costs that are 'close' to the maximum prior partial cost and is defined as follows.

$$I = \{i \in I | \hat{J}_{i,k+1} > 0.9(\max_j \hat{J}_{j,k+1})\}$$

To find a parameter update, the following line search algorithm is solved using the descent direction ΔK_{k+1}^*

$$\alpha^* = arg \min_{\alpha \in [0,1]} \max_i \frac{J_{i,k+1}(K_k + \alpha \Delta K_{k+1}^*)}{m_{i,k}} \tag{3.11}$$

Controller gain parameter is updated using the optimum α^* $\Delta K_{k+1} = K_k + \alpha^* \Delta K_{k+1}^*$.

For our problem here, we can further refine the algorithm in order to improve the speed of convergence and, thus, the transient performance, but including "sanity checks" to ensure the reliability of the estimates. Notice that, since we only estimate one parameter, the "theoretical" persistent excitation suggests that even a constant nonzero signal would be sufficient. However, this is misleading because it does not provide information on the linearized system around the intended crossover frequency. The latter is the required information for the selection of an acceptable controller and the RSC estimate is essentially the means to assess the reliability of the estimate for the desired closed-loop control. The refinements of the generic algorithm described in [67], specialized for pH control are listed below:

- For faster convergence, the covariance P associated with Eq. 3.9 is reset periodically if one of the following conditions is met.
  - If the set-point variation exceeds a threshold.
  - If the time elapsed since the last reset exceeds a threshold.
  - If there is a significant change in the pH reading (accounting for disturbances).
- The value of the covariance P depends on the level of excitation and represents confidence in the parameter estimate. The estimated parameter is accepted as an update in the controller only if the value of the sum of squares of P for the entire filter bank exceeds a threshold (determined indirectly by the level of noise and model variability).
- To avoid excessive bias in the parameter estimate, the plant input-output pair used in the adaptation algorithm is filtered using a band pass filter that attenuates frequencies of these signals outside the frequency range of interest.
- For this particular problem we perform adaptation under persistence of excitation and, therefore adaptation drifts can only occur under large perturbations. Nevertheless, the use of a dead-zone is always recommended in applications to avoid excessive

adaptation. It is interesting to observe here that a dead-zone threshold δ_{dzn} on the H_∞ norm of the loop mismatch error can be introduced by modifying the optimization cost in Eq. 3.9 as $\max[0, (J_{i,k}/m_{i,k}) - \delta_{dzn}]$. Since the cost is normalized as an RSC, one can even choose *a priori* the dead-zone level to a value of the tolerable error, e.g., 0.1.

We should point out that our intent is to design a controller that performs well under reasonable practical conditions, even at the expense of using considerable prior knowledge of the process and having increased design complexity. Furthermore, recognizing that there is always a possibility of failure in an industrial environment, we include monitoring conditions and tests to quantify the confidence in the controller tuning and enable the use of high-level monitoring schemes.

This refined algorithm was tested using the lab-scale experimental setup, described in the next section.

3.2 Experimental evaluation of the direct adaptive pH controller

In this section, we discuss the experimental evaluation of the proposed direct adaptive pH control algorithm. The experimental setup used is described in Chapter 2 and the block diagram of the lab setup is shown in Fig. 3.2. Our laboratory experimental setup used two peristaltic pumps, **Pump1** is used to control flow rates of the acid, the buffer stream1 and the buffer stream2 and peristaltic **Pump2** is used to control the base flow rate. Since we want to control pH of the liquid in the reactor by adjusting the flow rate of base flow **Pump2** and the pH sensor are interfaced with **Microcontroller1**(where control algorithm is implemented). The pH sensor used in this experimental setup has a quantization of 0.04 pH and the sampling time of 1 second. Flow rates of **Pump2** are controlled by varying analog voltage across its control terminal and to interface this pump with the **Microcontroller1** a MCP4725 12-bit digital to analog(DAC) converter is used. **Microcontroller1** communicates with the DAC using I^2C protocol and communicates with the pH sensor using UART serial. This experimental setup uses two Arduino

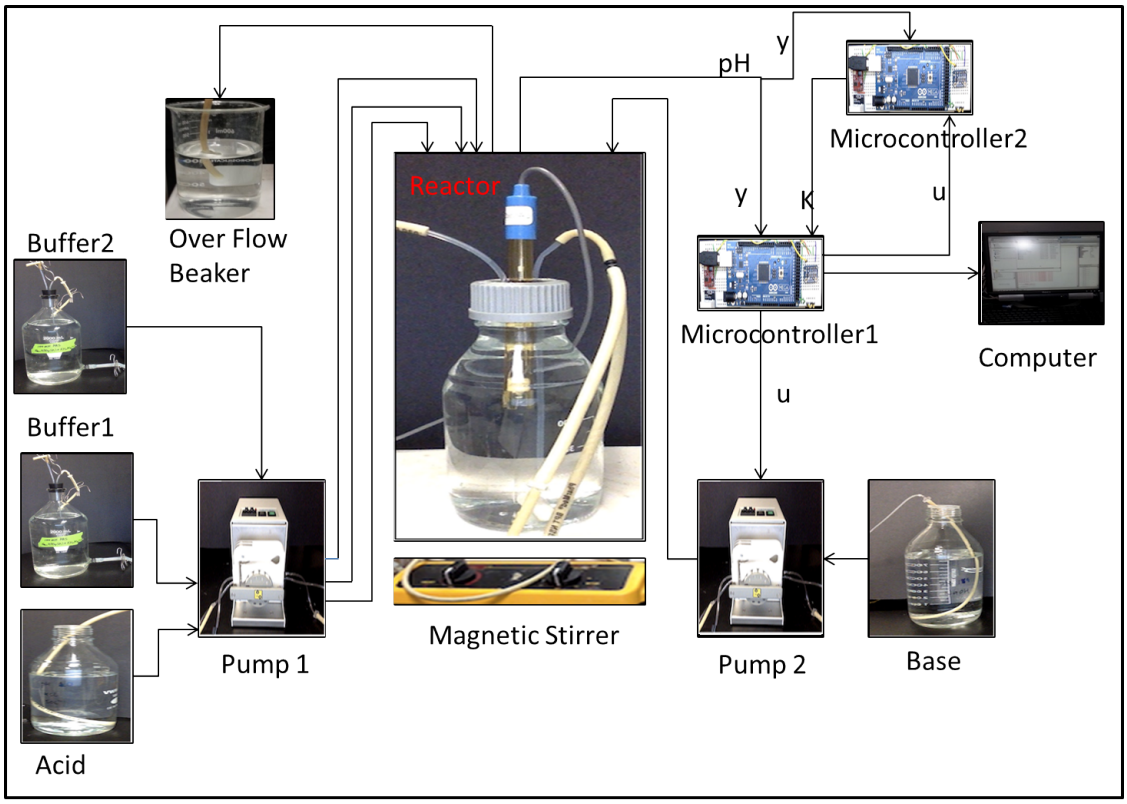

Figure 3.2: Block diagram of the lab-scale pH neutralization process CSTR

due microcontrollers one(**Microcontroller1**) to implement feedback control loop and other to implement the proposed adaptive control algorithm(**Microcontroller2**). Where, **Microcontroller1** acquires the pH value from the pH sensor, computes base flow rate using PI control algorithm and outputs control commands to the **Pump2**. It also transmits the sensor and the control values(base flow rates) to a supervisor PC for logging using UART serial communication. On the other hand, **Microcontroller2** receives plant's input(base flow rate) and output(pH) values from the **Microcontroller1**, computes the controller gain(K) based on the proposed direct adaptive control algorithm and sends the computed controller gain value to the **Microcontroller1**. Data transfer between **Microcontroller1** and **Microcontroller2** is also done using UART serial communication protocol.

The main motivation behind this experiment is to examine the behavior of the adaptive controller under realistic conditions and establish reasonable expectations as well as limitations of performance. It is shown that the linearized model of the plant, combined

with controller gain adaptation, is sufficient to achieve uniform performance across a wide range of operating points. At the same time, undesirable performance effects caused by the simultaneous lack of excitation and disturbances appear to be within practically tolerable limits.

The first step is to obtain the nominal plant model at the operating pH of 6 by fitting a linear model to the input-output data from a system identification experiment. This step provides an estimate of the plant dynamics, that undergo only small changes with the change of operating conditions. The latter was the result of the theoretical model analysis and was independently verified by performing identification at multiple operating points.

An important condition for the system identification to produce meaningful results is that the input signal used in the identification experiment should satisfy persistence of excitation condition. There are different ways to design such inputs and one of the common choice is a pseudo-random binary sequence (PRBS) [57] [35][14]. In our experiment, we identify the system around pH of 6 and for Case 1 of buffer flow combination using a PRBS input with the power spectrum that extends roughly up to the intended frequency crossover. The PRBS signal and process output are shown in Fig. 3.3(a). We employ a system identification algorithm, as described in [63] [64][55][71] [66] and [62], to identify a model of the process. We also use the estimation error to obtain an estimate of the uncertainty that will act as one of the constraints for the selection of an appropriate closed-loop bandwidth parameter, entering in the PID parameter tuning through the selection of the target loop.

The identified transfer function $\hat{G}_6$ is given by

$$\hat{G}_6(s) = \frac{7.630 \times 10^{-5}(-s + 1.53)}{(s + 4.26)(s + 0.018)} \tag{3.12}$$

and the identified model prediction of the response to the PRBS input is shown in Fig. 3.3(b).

Next, the nominal PI controller is designed for the nominal plant model with a target loop transfer function generated iteratively to maximize the closed-loop bandwidth subject to the estimated uncertainty constraint, as shown in Fig. 3.4(b). In general, the target

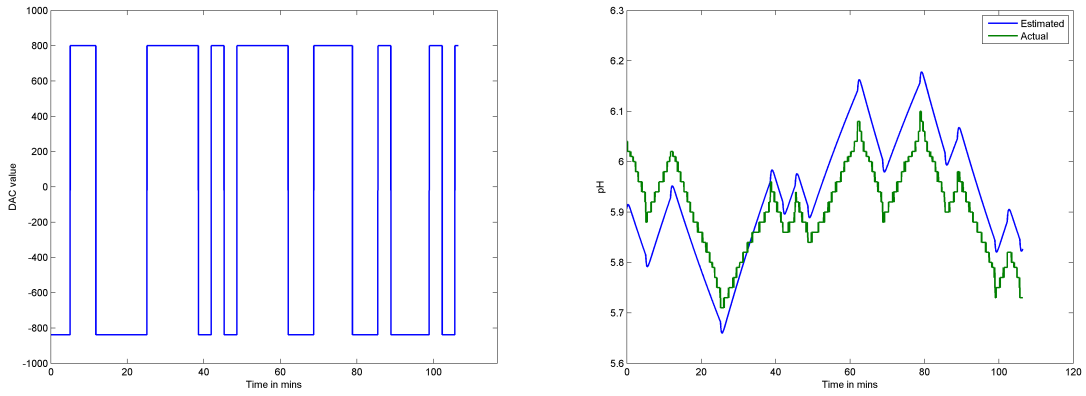

(a) (b)

Figure 3.3: System identification signals (a) input and (b) output(green trace) and predicted output(blue trace)

loop should also take into account limitations from the sensors and actuators, as well as bandwidth constraints from right-half plane zeros of the model.

A PI controller ($\hat{C}_6$)is designed for the plant $\hat{G}_6$ using an offline FLS algorithm [62] [23]. The target loop was chosen to achieve closed-loop bandwidth specification of 0.6 rad/min based on a linear quadratic regulator optimal loop with integrator augmentation and its transfer function is given below:

$$\hat{L}_6 = \frac{0.8273(s+4.28)(s+0.409)}{s(s+4.261)(s+0.018)} \tag{3.13}$$

The PI controller parameters of the nominal controller are obtained by minimizing an offline RSC and its transfer function is

$$\hat{C}_6 = \frac{2.124 \times 10^4 (s+0.273)}{s} \tag{3.14}$$

The Bode magnitude plots of the target loop and the actual loop transfer function is shown in Fig. 3.4(a) showing a fairly good matching.

To validate the designed controller, a coprime factor uncertainty estimate [63] [64] [66] [62][72] is obtained from the estimation error. A small gain condition for the co-prime factor

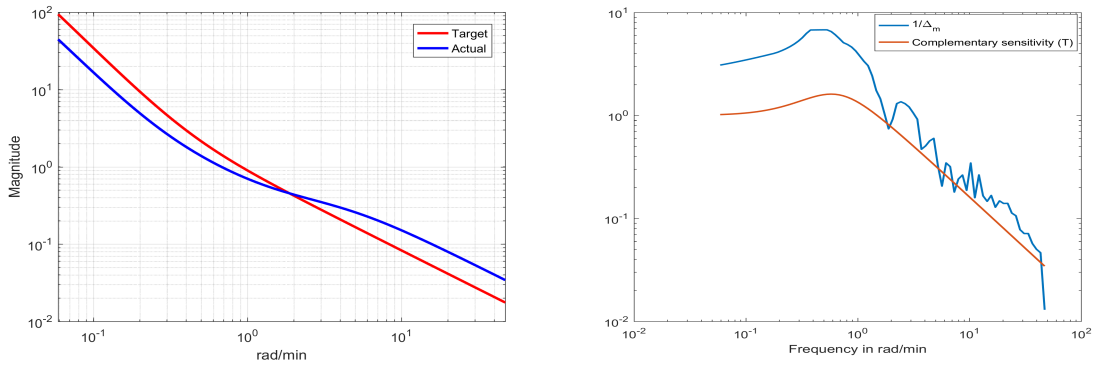

(a) (b)

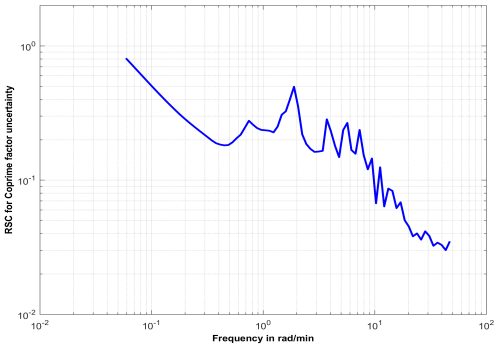

(c)

Figure 3.4: (a) Frequency response of target loop and identified loop transfer functions (b) complementary sensitivity plot (red) with its multiplicative uncertainty bound obtained in the identification step (c) RSC plot for the nominal controller; The actual loop and the target loop are close as expected. Multiplicative uncertainty provides an approximate bound on the complementary sensitivity and helps in the selection of a closed-loop bandwidth. For the chosen bandwidth of 0.6 rad/min the complementary sensitivity is at the at the constraint. A less conservative estimate, obtained using a coprime factor uncertainty computation, shows that the corresponding RSC (CFRSC) value less than 1 for all frequencies, thereby the designed controller is expected to yield robust closed-loop stability.

uncertainty estimate (CFRSC) is given by

$$CFRSC = \sigma \begin{pmatrix} \hat{C}_6 S M^{-1} \\ S M^{-1} \end{pmatrix} \sigma \begin{pmatrix} \Delta_N & \Delta_M \end{pmatrix} \tag{3.15}$$

where N, M are left coprime factors of the nominal plant(G_6) and Δ_N , Δ_M are their corresponding uncertainty estimates and S is the sensitivity of the loop with the controller $\hat{C}_6$. The use of CFRSC yields a less conservative result because the CF error is exactly

what is minimized by the least squares estimation. Any transformation of that error to multiplicative uncertainty is bound to produce a more conservative result. Fig. 3.4(c) shows a CFRSC value less than 1 for all frequencies, indicating the robust stability of the nominal controller ($\hat{C}_6$) with respect to the uncertainty arising from the estimation error. (A more precise statement is that the robust stability of the loop is not invalidated by the data, in the spirit of [58].)

For the direct adaptive control experiments, $\hat{C}_6$ was used as a base controller and the target loop used in its design ($\hat{L}_6$) was used as a target loop for the adaptation. Notice that here a fixed target loop was used throughout but, in general, nonlinear systems may require scheduling of the target loop as well, to reflect changing specifications or constraints, depending on the operating conditions.

The filter bank was constructed using 20 all-pass filters with corner frequencies spanning the logarithmic interval between $0.1BW$ to $10BW$, where BW is the bandwidth of target loop. The gain values of $[10, 10^6]$ were used as lower and upper limits of K respectively. A forgetting factor of 0.9999 was used and the covariance matrix was reset to its initial value every 25 minutes.

The closed-loop was tested for Cases 1 and 2 of the buffer flow described in the Section 2.2. Step changes from 6 to 9 and 6 to 3 are applied as set-points for the transition between operating points. To provide excitation for the adaptation and to assess the rate and the quality of convergence a small square wave was superimposed on the reference input (magnitude of 0.2 and period of 25 minutes). While this injected excitation is not intended to appear during normal operation, it is rather small and can be used if the supervisory or monitoring logic determines that the controller should be redesigned. A better choice would be a square wave with the fundamental frequency at the loop bandwidth, which is near the frequencies of interest. This choice, however, would not allow the easy visualization of adaptation convergence since the response would never approach the constant steady-state. As we also discuss later in the conclusion, the same excitation injected during set point

transitions is beneficial to the overall controller performance by helping the adaptation converge without causing significant errors.

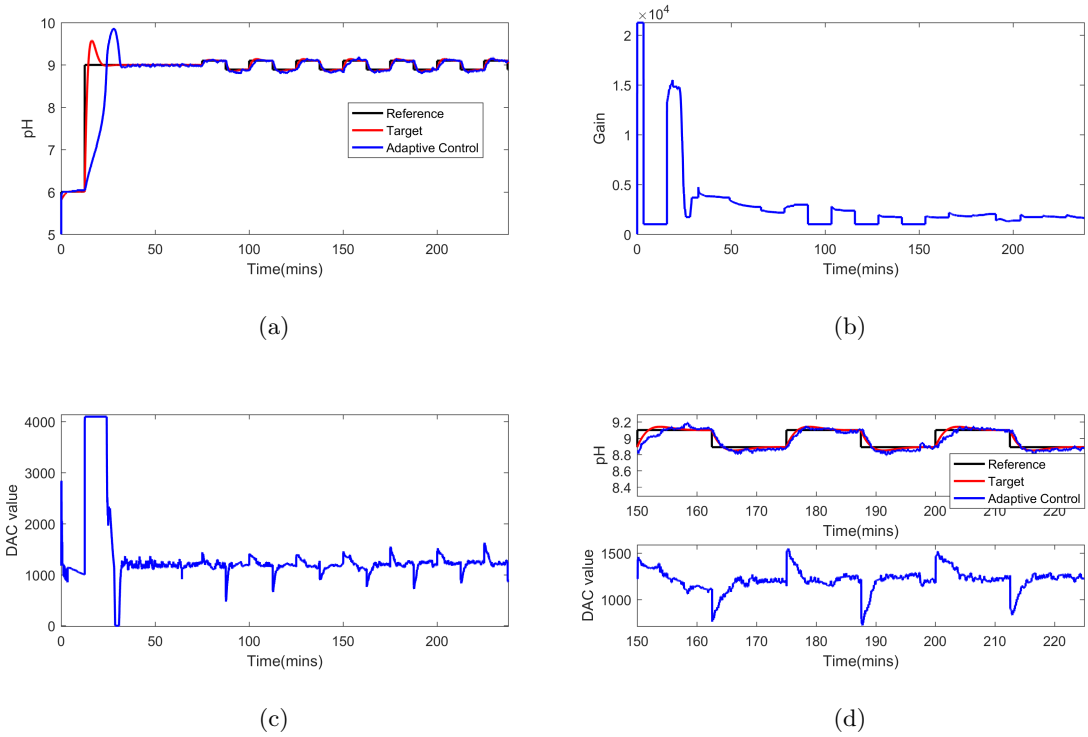

Figure 3.5: Closed-loop adaption results for Case 1 (a) plant output plot (b) controller gain plot (c) plant input plot (d) zoomed input-output plot; The proposed direct adaptive control adapts controller gain to compensate for the gain changes in the plant with operating points. The big step transition signal results in the large overshoot and it takes about two small square pulses for the controller gain convergence.

The experimental results with the direct adaptive pH controller are shown in Fig. 3.5 -3.8. We observe that the proposed controller is able to adapt reasonably well to the gain changes in the plant with the operating points and with the change in buffering capacity. Undesirable characteristics of the response include the rather large overshoot during the step change of the setpoint from 6 to 9 pH (Fig. 3.5). This is not unreasonable since even the nominal loop exhibits some overshoot (red trace), but the overshoot is exacerbated by the slow adaptation of the gain. In such transitions, the transient response offers very little information on the plant around the step point and the adaptation cannot be expected to converge very quickly.

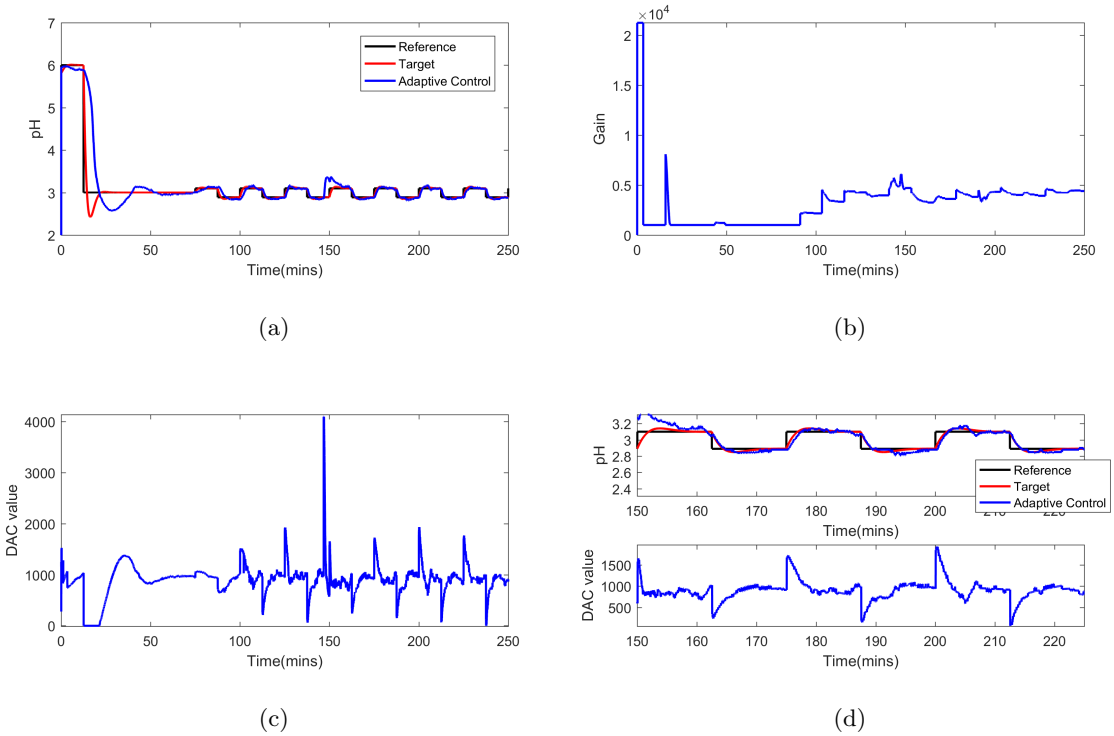

Figure 3.6: Closed-loop adaption results for Case 1 (a) plant output plot (b) controller gain plot (c) plant input plot (d) zoomed input-output plot; The proposed direct adaptive control adapts controller gain to compensate for the gain changes in the plant with operating points. The big step transition signal results in the large overshoot and it takes about two small square pulses for the controller gain convergence. The controller also rejects external disturbance at 150 mins

We also observe that the controller gain convergence time depends on the input and parameter saturation. As shown in Fig. 3.5 - 3.8, convergence was achieved in around 2-3 small pulses, after which the gain reaches steady state and the closed-loop system response is very close to the target response. In Fig. 3.6 and Fig. 3.8 we observe a spike after convergence. It is the result of an unintentional disturbance, which, nevertheless, verifies that the adaptive controller response remains reasonable. We conclude that using a single data-driven linear model (obtained using a system identification experiment) along with the proposed direct adaptive algorithm to update the gain, we achieve successful closed-loop pH control over a wide range of operating conditions including variations in the pH, as well as in the buffer flows.

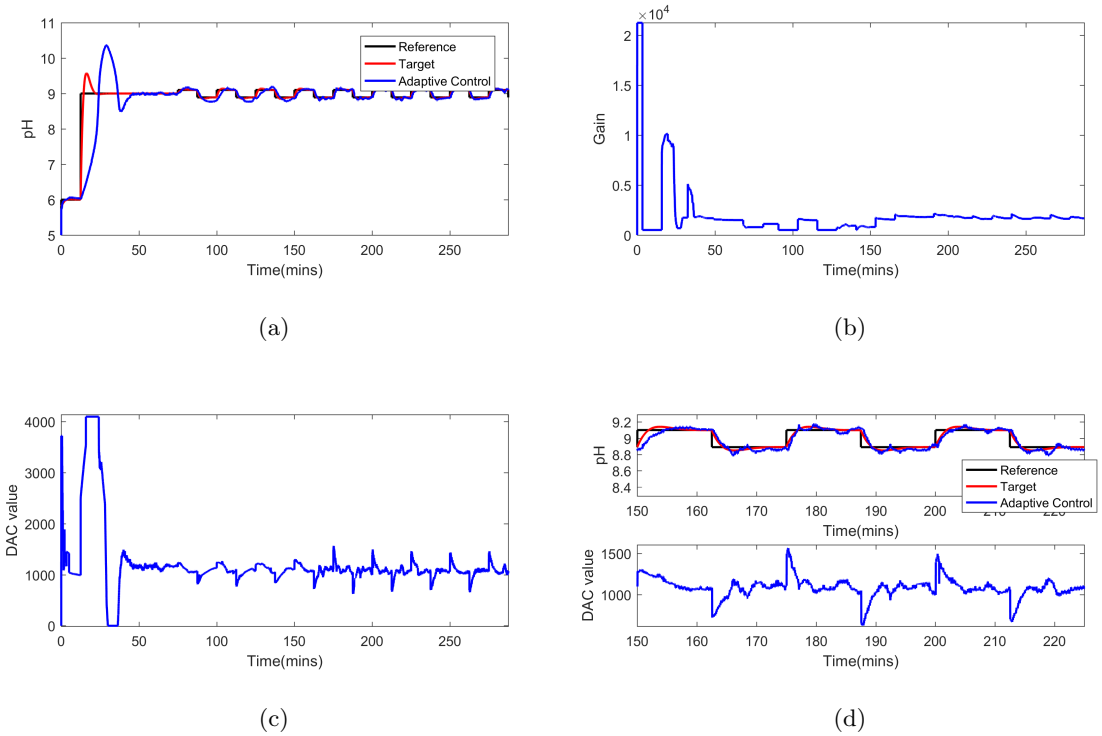

Figure 3.7: Closed-loop adaption results for Case 2 (a) plant output plot (b) controller gain plot (c) plant input plot (d) zoomed input-output plot; The proposed direct adaptive control adapts controller gain to compensate for the gain changes in the plant with operating points and buffer flow variation. The big step transition signal results in the large overshoot and it takes about two small square pulses for the controller gain convergence.

3.3 Direct adaptive pH control simulation results

The experimental models are qualitatively very similar to the simulations of the model derived from first-principles, even though it requires detailed modeling to achieve quantitative matching. This similarity allows us to investigate the behavior of the proposed adaptive controller under a much wider set of conditions using computer simulations, for example, those mentioned in Section 2.2. They are also used to test the proposed adaptive control algorithm for the variation in the excitation properties. The simulations are also used to examine the effectiveness of alternative schemes and the determination of sound principles for their practical implementation.

In this section we evaluate the proposed direct adaptive pH control algorithm using

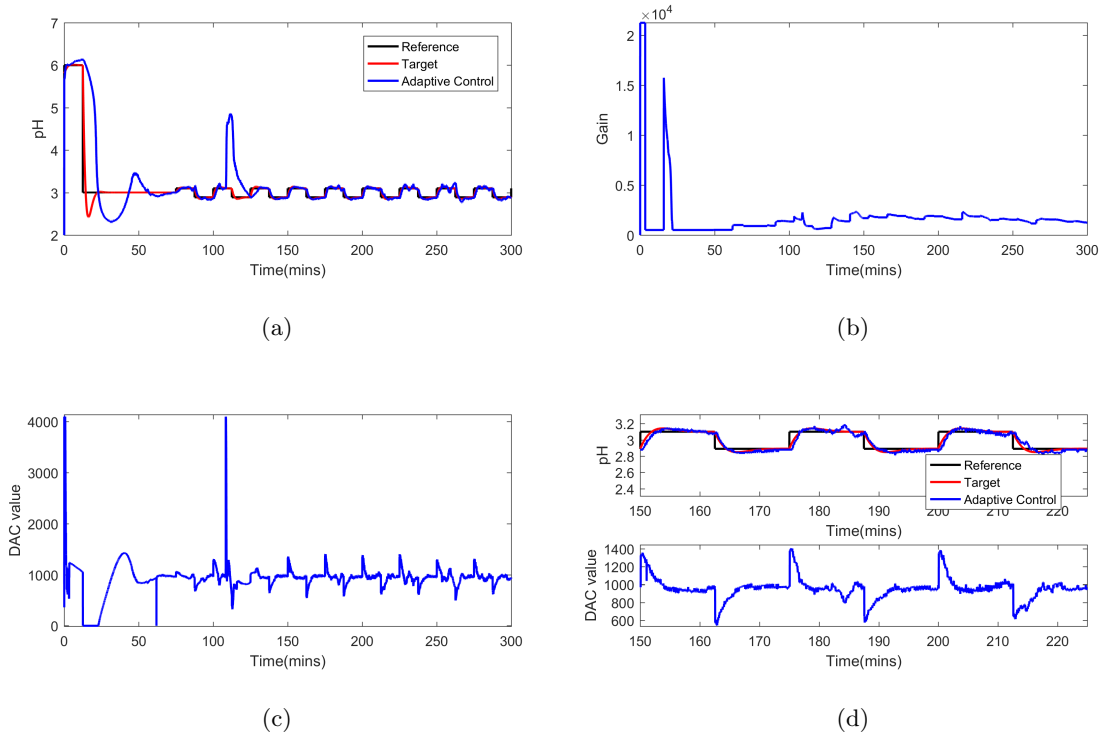

Figure 3.8: Closed-loop adaption results for Case 2 (a) Plant output plot (b) controller gain (c) plant input plot (d) zoomed input-output plot; The proposed direct adaptive control adapts controller gain to compensate for the gain changes in the plant because of buffer flow changes. There is a spike in the pH around 110th minute, which is the result of a significant unknown disturbance in the system, unrelated to our injected excitation. The response of the adaptive controller is reasonable and it quickly rejects this disturbance.

computer simulations. In subsection 3.3.1, we present results from a comparative study between adaptive control algorithms using H_∞ cost objective(system norm) against L_2 norm based cost objectives (signal norm) under different excitation conditions. In subsection 3.3.2, we present tracking results that validate the ability of the proposed algorithm to adapt controller parameters to compensate plant nonlinearities over a wide range because of set-point and buffer flow changes.

For our simulation studies, we use linearized plant at pH 6 (Case 1) as a nominal plant (G_6) and a PI controller (C_6) is designed for this plant as the nominal controller. To be consistent with the experimental setup we use offline FLS algorithm with the target loop L_6 that corresponds to the closed-loop bandwidth of 0.6 rad/min to tune the nominal

controller. Transfer functions of the nominal plant(G_6), the nominal controller(C_6) and the target loop(L_6) are listed below.

$$G_6(s) = \frac{0.000197}{(s+0.0191)} \times e^{-s/6} \tag{3.16}$$

$$C_6(s) = \frac{4206(s+0.434)}{s} \tag{3.17}$$

$$L_6(s) = \frac{0.83(s+0.434)}{s(s+0.0191)} \tag{3.18}$$

Details of the parameters used in the adaptation algorithm are discussed in the next section.

3.3.1 Comparative study

In this subsection, we evaluate the performance of the proposed FLS H_∞ cost function used in the adaptive control algorithm under different excitation signals against a L_2 cost function based FLS algorithm. The goal of this section is to study both adaptation algorithms under different excitation. For this study, we also consider two parameter adaptation version of the proposed FLS H_∞ direct adaptive algorithm where we independently adapt proportional and integral gains of PI controller.

For this study, we start at nominal pH 6 and go to the set point of pH 7.5 at the 25th minute and to provide the excitation for the adaptive control algorithms we inject sine wave signals with different frequencies at the plant input(u_i in Fig. 3.14) or at the reference(r in Fig. 3.14) for the duration of 325 mins. An example of one such reference signal (R_3) is shown in Fig. 3.9. After 350 minutes, both sine wave excitation and adaptation are turned off and a small square wave of 0.1 magnitude is applied at reference which is used in the performance evaluation of both algorithms in the time domain. To evaluate performance in the frequency domain we compare their H_∞ FLS distance(RSC measure described in Eq. 3.3) of the converged parameters. Specifically, we look at the bound of RSC value of the converged controller computed online using I/O data as shown in Eq.3.5. We also study offline RSC values of both algorithms, which is computed using converged controller

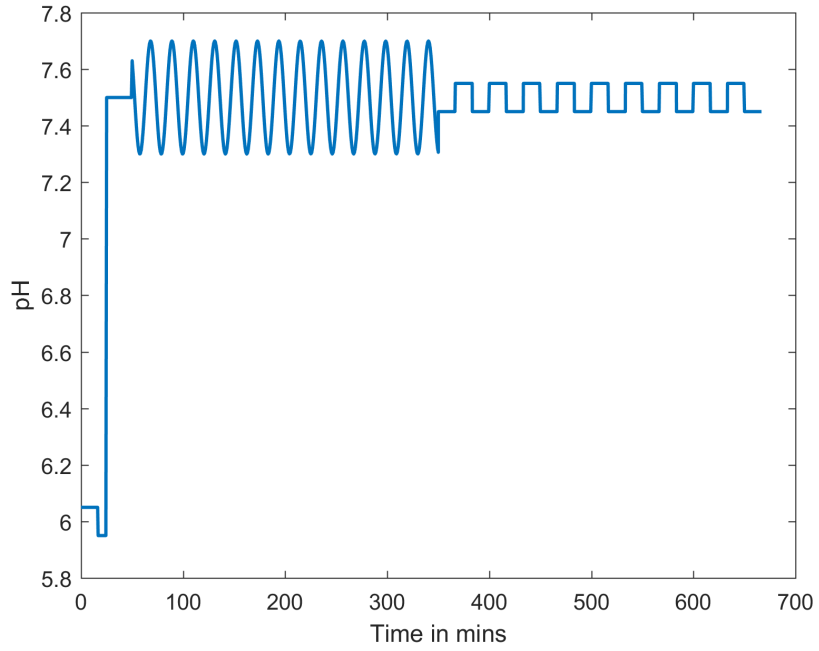

Figure 3.9: Sample test reference signal(R_3) used in the comparison study

parameters (K and θ) and linearized plant at pH 7.5 using Eq. 3.3. Details of parameters used in the adaptive control algorithms for this study are listed below.

- Two parameters
  - H_∞ cost function:

$$\theta^* = arg \min_{\theta} \max_{i} \frac{||(SF_i W^T y)\theta - TF_i u)||_{2,\delta}}{||F_i u||_{2,\delta}} \tag{3.19}$$

  - L_2 cost function:

$$\theta^* = arg \min_{\theta} ||(SW^T y)\theta - Tu)||_{2,\delta} \tag{3.20}$$

  Where $W = [1; \frac{1}{s}]$ represent regressors and $\theta = [K_p K_i]$, where K_p and K_i represent proportional and integral gain of the PI controller.

- One parameter
  - H_∞ cost function:

$$K^* = arg \min_{K} \max_{i} \frac{||(SF_i \widetilde{C} y)K - TF_i u)||_{2,\delta}}{||F_i u||_{2,\delta}} \tag{3.21}$$

- L_2 cost function:

$$K^* = arg\min_K ||(S\widetilde{C}y)K - Tu)||_{2,\delta} \tag{3.22}$$

Where $\widetilde{C} = \frac{s+a}{s}$ and K represent PI controller gain expressed in Eq. 3.6 form.

- Closed-loop bandwidth: $BW = 0.6rad/min$
- Forgetting factor (λ)=5×10^{-4}
- Filter Bank [F_i]: 20 filters logarithmically placed between $0.1 \times BW$ and $10 \times BW$
- Frequency of sine wave injected at plant input:
  - Ui_1: 18 rad/min
  - Ui_2: 0.6 rad/min
  - Ui_3: 0.3 rad/min
- Frequency of sine wave injected at reference:
  - R_1: 18 rad/min
  - R_2: 0.6 rad/min
  - R_3: 0.3 rad/min

These adaptive control algorithms are tested for all excitation signals. Controller parameter values(at 300th minute) for both two and one parameter adaption are listed in Table 3.1 and Table 3.3 respectively. Mean and variance plots of these parameters are shown in Fig. 3.11(a) and Fig. 3.10(a). RSC values computed online and offline for both two parameter and one paramter adaptation are listed in Table. 3.2 and Table 3.4 respectability. Their corresponding mean variance plots are shown in Fig 3.10(b) and Fig. 3.11(b). Time domain evaluation results for these cases are shown in Fig. 3.13 and in Fig. 3.12

It can be seen from the time domain results Fig. 3.12 and Fig. 3.13 both H_∞ and L_2 algorithms produce tracking performance close to the target for low frequency excitation(U_3

Table 3.1: Controller parameter values of adaptive control algorithms for two parameters adaptation

Excitation	H_∞		L_2	
	K_p	K_i	K_p	K_i
Ui_1	3708.4	1098	464.8882	1643.6
Ui_2	1841.6	648	4024.2	1644
Ui_3	2446.1	882	9371.2	1644
R_1	3715.6	1344	840.8206	1644
R_2	3715.6	1158	2709.6	1644
R_3	3715.6	1038	2511.5	1644

Table 3.2: RSC values of adaptive control algorithms for two parameters adaptation

Excitation	H_∞		L_2	
	RSC_{on}	RSC_{off}	RSC_{on}	RSC_{off}
Ui_1	0.4053	0.3245	0.8736	0.8512
Ui_2	0.5202	0.5129	0.5813	0.5034
Ui_3	0.4740	0.3002	1.3251	2.3052
R_1	0.4062	0.3275	0.7631	0.7267
R_2	0.4624	0.3212	0.6465	0.3473
R_3	0.3693	0.3362	0.5667	0.3479

Table 3.3: Controller parameter values of adaptive control algorithms for one parameter adaptation

Excitation	H_∞	L_2
Ui_1	3254.7	100
Ui_2	2671.8	2766.5
Ui_3	2194.9	2776.1
R_1	2285.6	100
R_2	2584.9	2722.7
R_3	2583.5	2786.2

Table 3.4: RSC values of adaptive control algorithms for one parameter adaptation

Excitation	H_∞		L_2	
	RSC_{on}	RSC_{off}	RSC_{on}	RSC_{off}
Ui_1	0.2876	0.2026	0.9526	1.2109
Ui_2	0.2369	0.0785	0.3503	0.0459
Ui_3	0.9763	0.2722	0.4497	0.0425
R_1	0.2812	0.2316	0.8079	1.2109
R_2	0.3522	0.1085	0.3909	0.0610
R_3	0.4198	0.1090	0.4594	0.0390

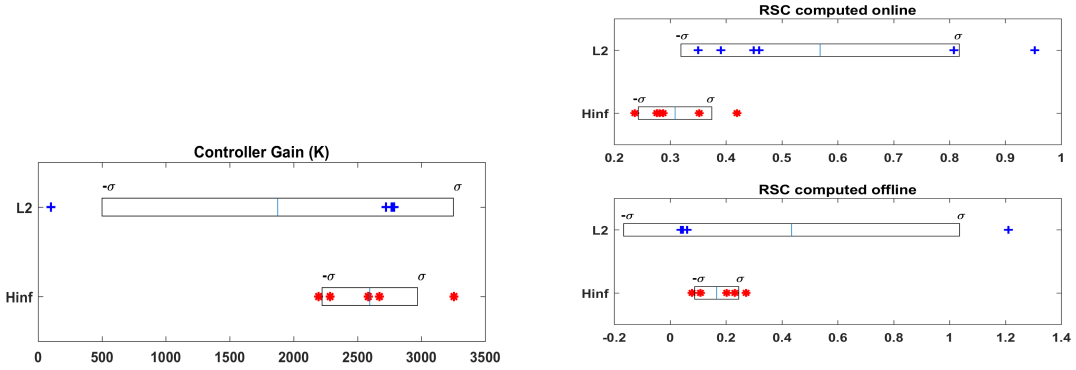

(a) (b)

Figure 3.10: Results for one parameter adaptation (a) controller gain(K) (b) RSC estimates; Variance in the controller gain for the H_∞ cost is far less than that of L_2 cost; RSC values computed online and offline for the H_∞ are far less as compared to of L_2 cost function

and R_3) and for the frequency of excitation at the bandwidth(U_2 and R_2). But, only H_∞ produces good tracking performance for high frequency excitation(U_1 and R_1). This fact can be further validated from both online and offline RSC values (Fig. 3.10(b) and Fig. 3.11(b)). It can clearly be seen from the RSC values H_∞ algorithm produces actual control loop that is close to the target(low RSC values) as compared to the L_2. It is seen in Fig. 3.10(a) and Fig. 3.11(a) variance of the controller gain in one parameter adaptation and the proportional gain in two parameter adaptation is low for the H_∞ as compared to L_2. However, variance in the integral gain high for H_∞ as compared to L_2 and this is

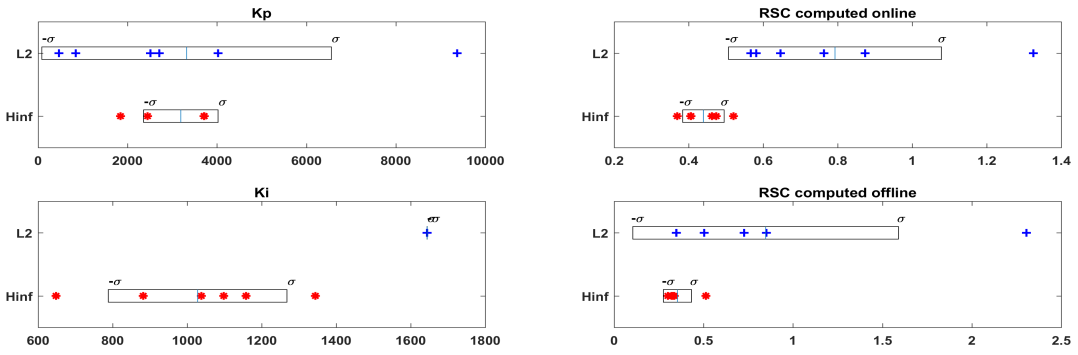

(a) (b)

Figure 3.11: Results for two parameter adaptation (a) controller parameters (θ) (b) RSC estimates; Variance in the controller proportional gain for the H_∞ cost is far less than that of L_2 cost and opposite for the controller integral gain; RSC values computed online and offline for the H_∞ are far less as compared to of L_2 cost function

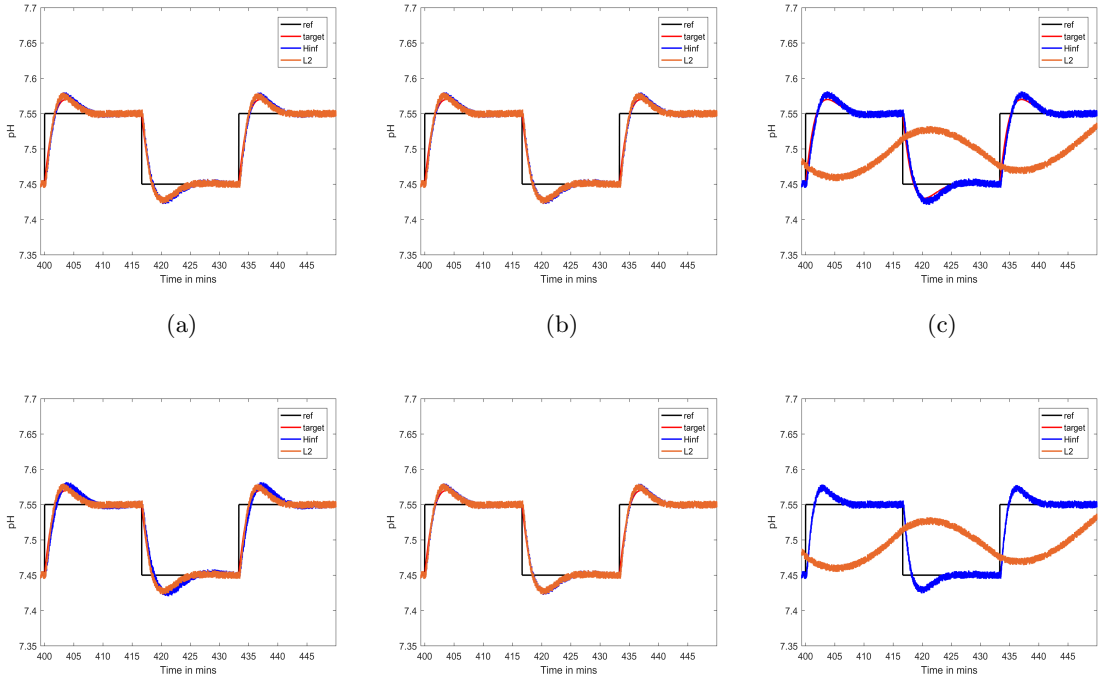

(a) (b) (c)

(d) (e) (f)

Figure 3.12: Tracking plots in time domain for one parameter adaption (a) for R_3 excitation (b) for R_2 excitation (c) for R_1 excitation (d) for Ui_3 excitation (e) for Ui_2 excitation(f) for Ui_1 excitation; For low frequency excitation (plots (a) and (d)) and for excitation at bandwidth (plots (b) and (e)) both H_∞ and L_2 produce results close to the target. For high frequency excitation (plots (c) and (f)) both H_∞ produces response close to the target and L_2 produces result that is completely off

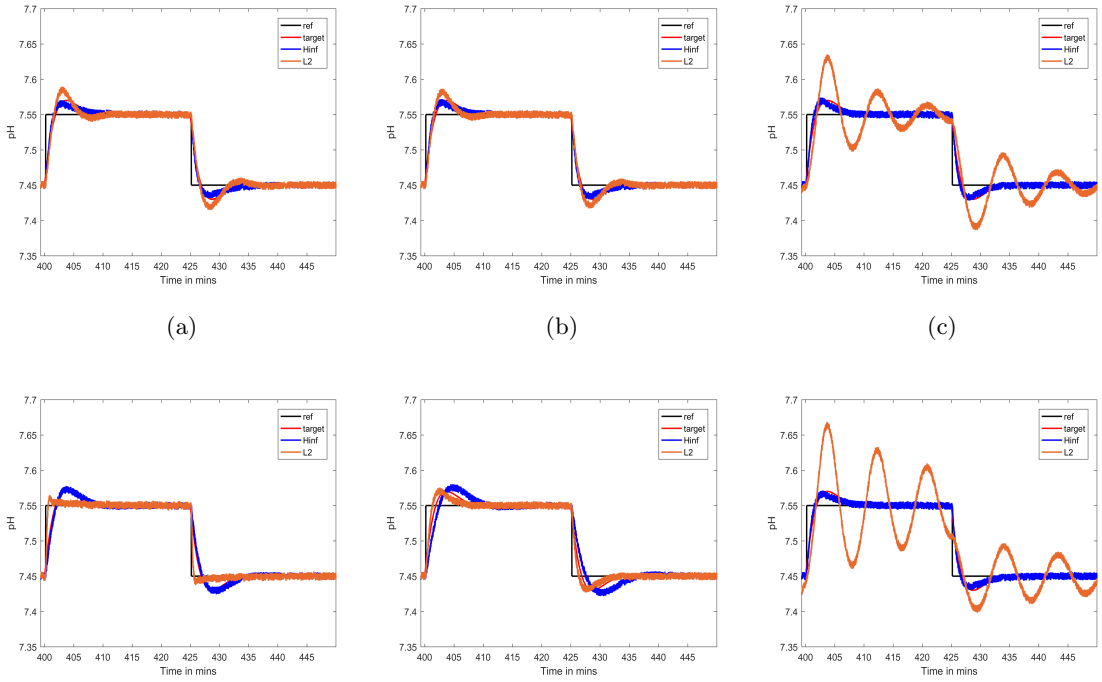

(a) (b) (c)

(d) (e) (f)

Figure 3.13: Tracking plots in time domain for two parameters adaption (a) for R_3 excitation (b) for R_2 excitation (c) for R_1 excitation (d) for Ui_3 excitation (e) for Ui_2 excitation (f) for Ui_1 excitation; For low frequency excitation (plots (a) and (d)) and for excitation at bandwidth (plots (b) and (e)) both H_∞ and L_2 produce results close to the target. For high frequency excitation (plots (c) and (f)) H_∞ produces response close to the target and L_2 produces result that is completely off

because L_2 algorithm's integral gain is stuck at the parameter constraint. These results conclusively prove H_∞ cost function's low susceptibility to the type of excitation. The proposed direct adaptive control algorithm is further tested for wider set-point changes and for buffer variation. Details of settings used in the testing along with results are discussed in the next subsection.

3.3.2 Performance evaluation of the direct adaptive pH controller

To test the proposed adaptive control for wider operating range we use C_6 (Eq. 3.17) as the nominal controller and L_6 (Eq. 3.18)as the target loop. To test tracking we simulate the transitions from the nominal(pH 6) to other operating points, namely pH 3, 4.5, 6, 9, 12. A small square wave with 25 mins period is also injected after the transition to assess the

speed of convergence. Results from the simulation show the adaptive controller performs well and the controller gain adaptation compensates for variation in the plant gain because of changes in the operating point and buffer flows, as anticipated. Some sample results from the simulations are shown below.

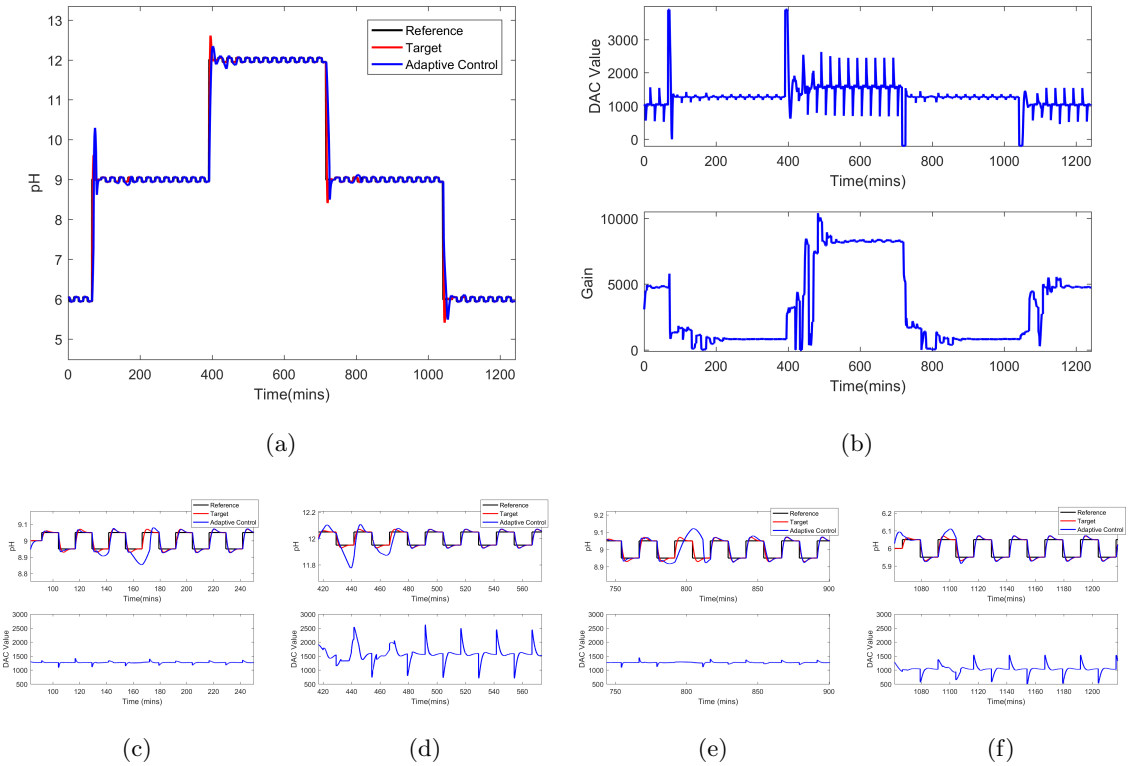

Figure 3.14: Direct adaptive pH control results for Case 1 (a) output plot (b) top plot- plant input, bottom plot- controller gain plot (c-f) zoomed in input-output plots after each big transition step; This simulation result is similar to the experimental result. Step transition signals result in huge over shoot and the controller gain adapts to the change in the system with pH operating point. The transient time is high because of input and parameter saturation.

Set-point transitions and adaptation convergence are shown in Fig. 3.14 and Fig. 3.15 . We observe the similarity with the experimental results and the fairly quick adaptation as it takes approximately 2-3 cycles of the square wave for the controller gain to converge. We also note a significant overshoot during the step change, this results from the inability to estimate the correct gain in such a short time.

Results for the buffer flow cases 2, 3 and 4 are shown in Figures 3.16, 3.17 and 3.18

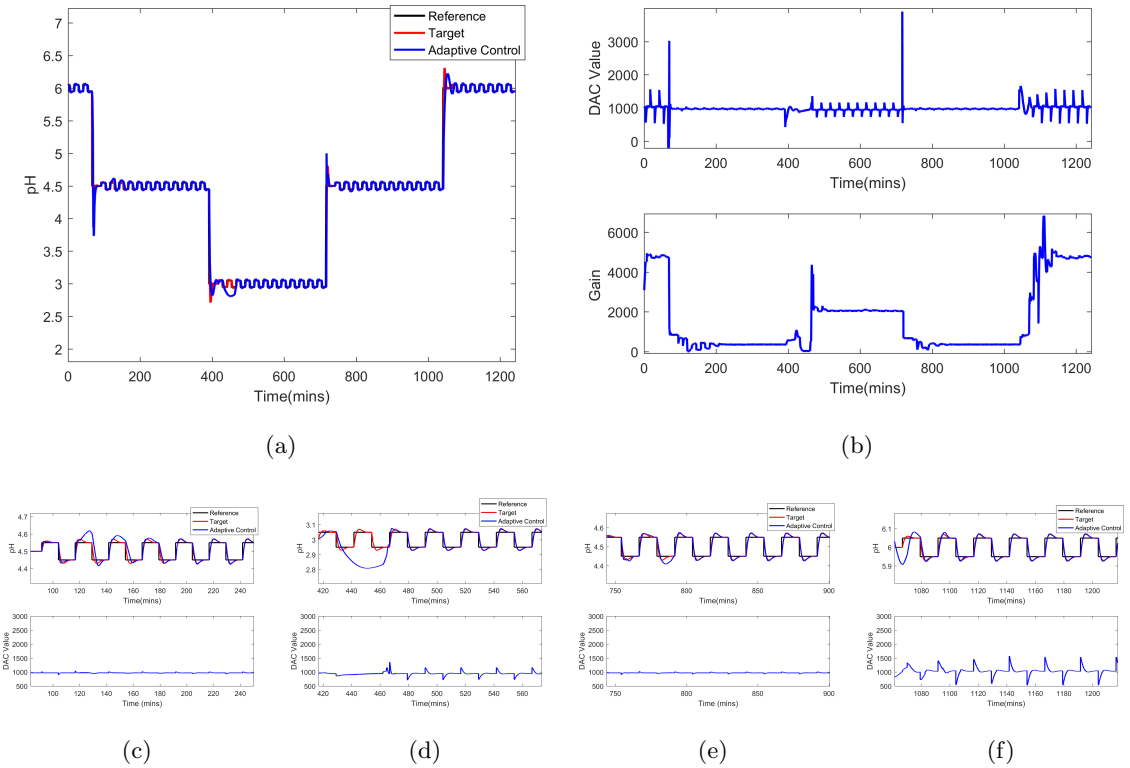

Figure 3.15: Direct adaptive pH control results for Case 1 (a) output plot (b) top plot- plant input, bottom plot- controller gain (c-f) zoomed in input-output plots after each big transition step; This simulation result is similar to the experimental result. Step transition signals result in huge over shoot and the controller gain adapts to the change in the system with pH operating point. The transient time is high because of input and parameter saturation.

respectively. In all these cases buffer flow is changed to their corresponding values at pH 6 and the step transition is applied after pH reaches the steady state. It can be seen from these plots, after set-point transition the gain of the controller is adapted to a steady state value that results in a performance closer to the target. As compared to the Case 1 the transient time is higher in these cases. One reason for the longer transient time is the controller parameter saturation. This phenomenon is clearly observed in Figures 3.16(e), 3.17(b),3.17(e) and 3.18(e).

Simulation results reinforce our conclusions from the experimental results, that the proposed direct adaptive control algorithm is able to achieve reasonable and uniform performance, while relatively weak excitation requirements (e.g., small square wave) can

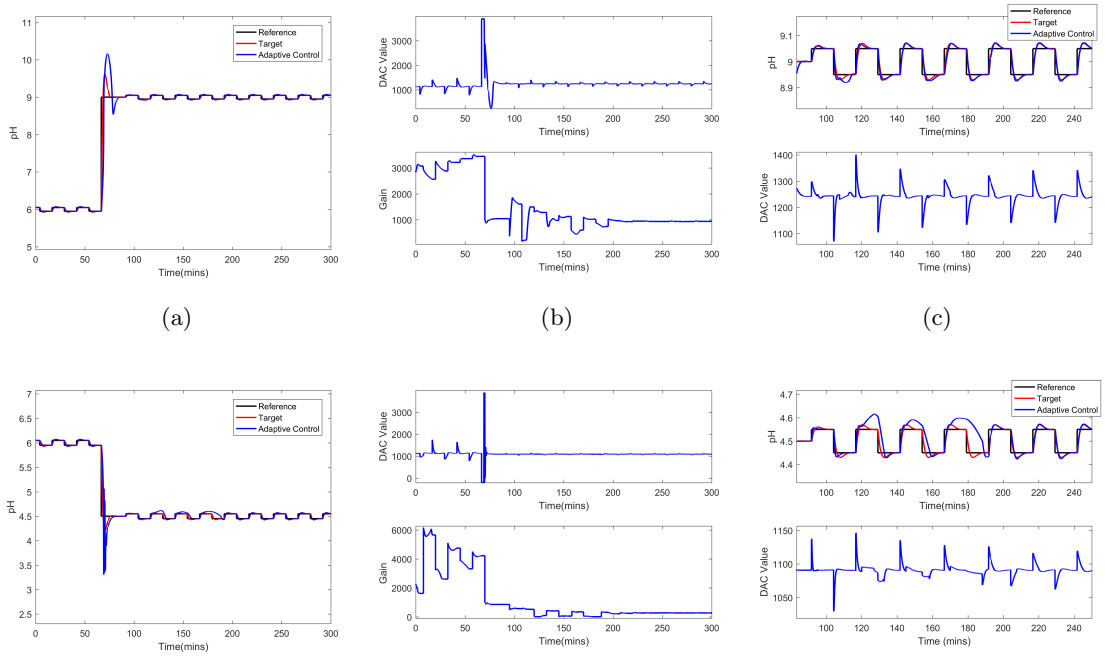

(a) (b) (c)

(d) (e) (f)

Figure 3.16: Direct adaptive pH control results for Case 2, (a) and (d) output plots, (b) and (e) top plots- plant input, bottom plots- controller gains, (c) and (f) zoomed in plots of the input output plot in (a) and (d) respectively after each big step; With the buffer flow changes the controller gain adaptation produces uniform performance

yield quick parameter convergence.

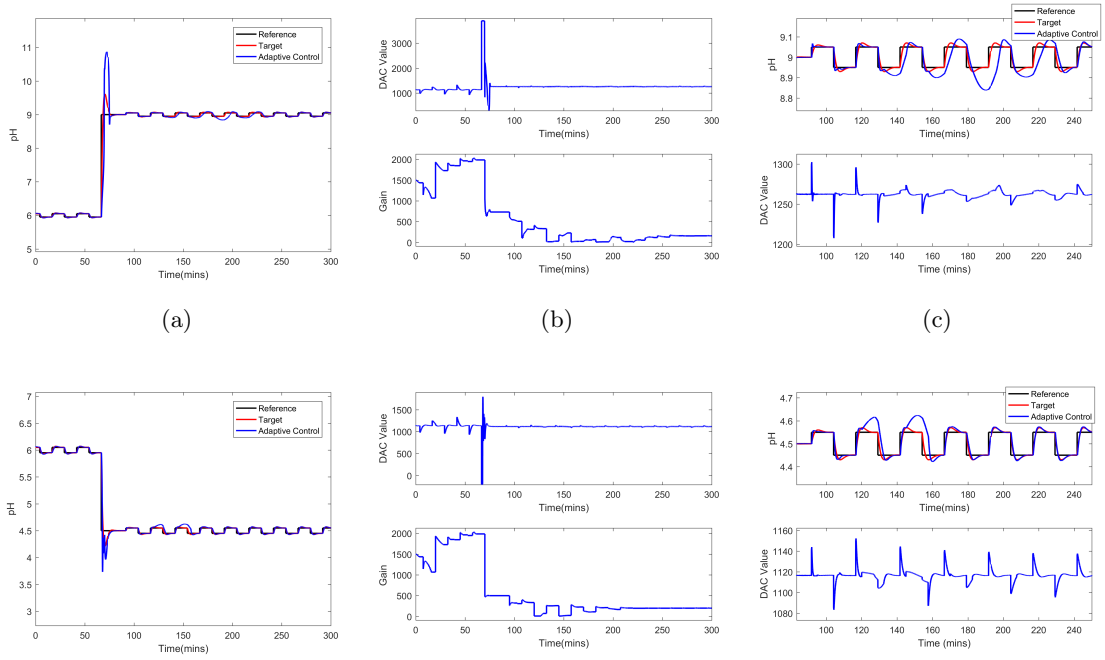

(a) (b) (c)

(d) (e) (f)

Figure 3.17: Direct adaptive pH control results for Case 3, (a) and (d) output plots, (b) and (e) top plots- plant input, bottom plots- controller gains, (c) and (f) zoomed in plots of the input output plot in (a) and (d) respectively after each big step; With the buffer flow changes the controller gain adaptation produces uniform performance

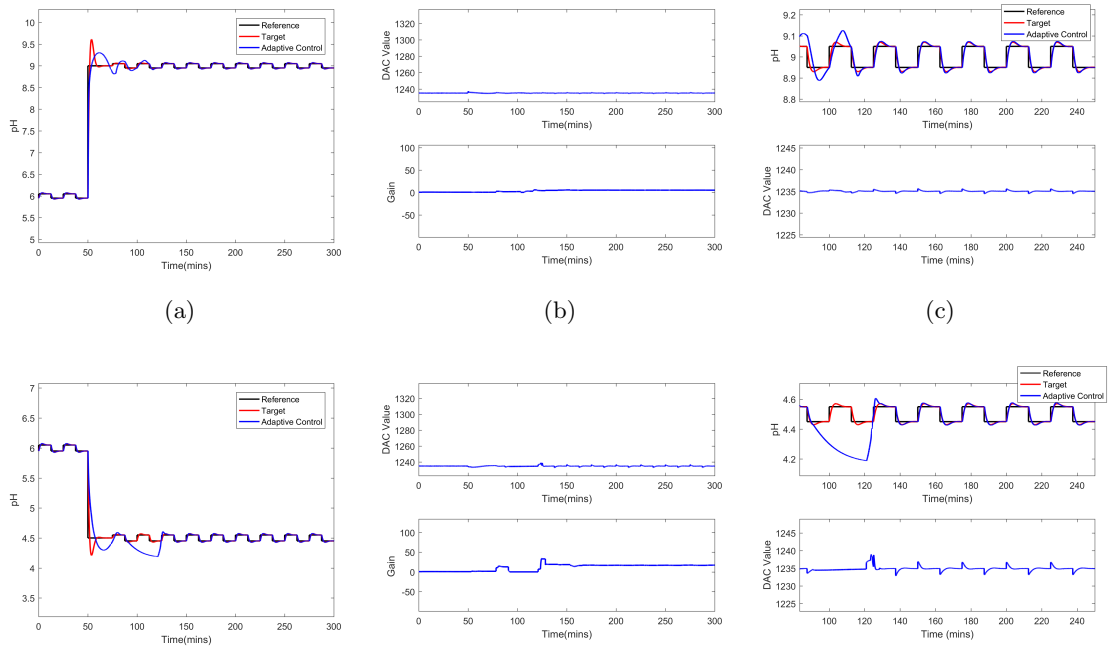

(a) (b) (c)

(d) (e) (f)

Figure 3.18: Direct adaptive pH control results for Case 4, (a) and (d) output plots, (b) and (e) top plots- plant input, bottom plots- controller gains, (c) and (f) zoomed in plots of the input output plot in (a) and (d) respectively after each big step; With the buffer flow changes the controller gain adaptation produces uniform performance

Chapter 4

MULTI MODEL ADAPTIVE PH CONTROLLER

4.1 Multi model adaptive controller algorithm with RSC metric

Interest in multi-model adaptive control (MMAC) has gained traction significantly in recent past. In this scheme, the controller used in the closed-loop system is selected from a bank of controllers based on metrics derived from the on-line data. As long as the possible controllers can be restricted to a discrete (and hopefully small) set, the multi-model adaptation can be extended to various controller structures and can adapt rapidly, as soon as the decision signal changes. On the other hand, MMAC is computationally expensive and may cause performance deterioration if the suitable controller is not present in the selected controller bank.

In a quick overview, MMAC uses the plant input-output data to estimate a performance or health metric, assessing the suitability of a controller in the loop. This metric is then used to rank the potential controllers and switching to the best candidate. Although the pH control problem does not necessarily fit the MMAC paradigm in the sense that a large number of controllers is needed to span the range of possible process gains, it is still a candidate application because the controllers are simple and controller bank can be restricted to only one parameter.

In the past, we have successfully used RSC metrics for the controller performance monitoring,[61] indicating that the same metric can be applied in an MMAC framework to the pH control problem. The key difference of this metric is the approximation of the H_∞ gain of the mismatch operator, instead of the more frequently mentioned 2-norm of the error signal. Our expectation, supported by simulations is that the proposed metric would translate into reduced sensitivity of the optimal solution to the input signal properties and a more uniform performance.

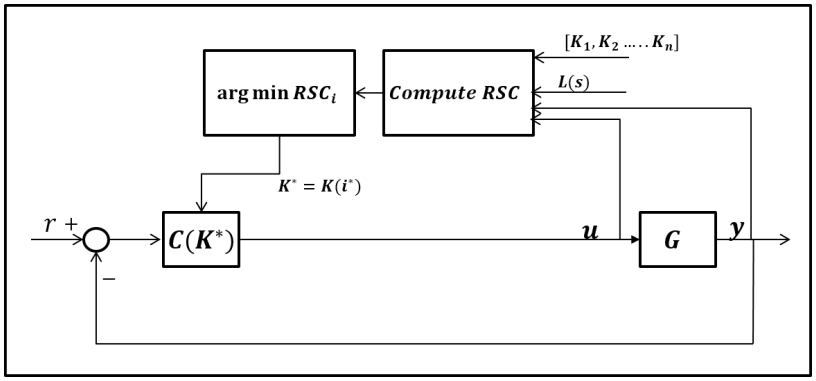

Figure 4.1: Block diagram of the closed-loop system with multi model adaptive pH controller

For the MMAC algorithm, we consider $[G_j]$, where $j = 1, 2 \ldots n$ be the bank of plants and $[C_j]$ be the corresponding controllers designed using an offline FLS algorithm using a target loop-shape L. The RSC estimate of the controller(C_j) computed using the plant's input-output data and it is described using the following equation.

$$RSC_j = \max_i \frac{||SC_jF_iy - TF_iu)||_{2,\delta}}{||F_iu||_{2,\delta}} \tag{4.1}$$

The objective of a multi-model adaptive control is to switch to a controller that results in a minimum estimate of RSC. Following equation describes controller section criteria of this algorithm.

$$C_{j^*} = arg \min_j \max_i \frac{||SC_jF_iy - TF_iu)||_{2,\delta}}{||F_iu||_{2,\delta}} \tag{4.2}$$

In our case of pH control, the controller structure is restricted to a PI parametrization and only its gain is adapted. Mainly, the bank of controllers is then formed by just varying the gain of the PI controller designed for the nominal plant model(some preselected operating point). It is desirable for an MMAC algorithm to avoid excessive switching during transients. A common approach is to introduce a switching threshold or a hysteresis logic, this provides trading off between transient performance for a less oscillatory behavior. The RSC-based MMAC algorithm with hysteresis for the pH control is described as follows:

- Design PI controller C_0 for the nominal plant G_0.

- Build the bank of PI controllers $[C_j]$ by varying the gain (K_j) of the nominal controller C_0.
- Initialize 'controller selected' to the nominal controller C_0.
- For each time step k
  - Compute RSC values for all controllers in the controller bank $[C_j]$

$$RSC_j(k) = \max_i \frac{||SC_jF_iy(k) - TF_iu(k))||_{2,\delta}}{||F_iu(k)||_{2,\delta}} \tag{4.3}$$

  - If $RSC_{selected} > (1+h)\min_j RSC_j(k)$, then switch to the controller C_{j^*}, where $RSC_{selected}$ is the RSC value of the currently selected controller, $j^* = arg\min_j RSC_j(k)$ and h is a hysteresis parameter $(h > 0)$.

The evaluation of the RSC metric (as all similar metrics) involves computation of exponentially weighted norms of signals and the forgetting factor computation provides an inherent trade-off between long and short-term memory. The former has noise immunity while the latter offers fast adaptation to rapidly changing conditions. The choice of an exponential weight (δ) is very important in the RSC computation. Smaller values of δ results in the RSC estimate close to actual(2-norm), but it has higher transient time. On the other hand, higher values of the δ have low transient time, but the RSC estimates have spikes and are far from actual 2-norm. An example plot of RSC computation with different exponential weights is shown in figure 4.2. Comparison between the estimated exponentially weighted norm and the actual 2-norm (Fig. 4.2) of the RSC indicates that $\delta = BW/10$, where BW is the bandwidth of target loop transfer function is a reasonable choice.

The RSC computation also needs to handle the possible lack of excitation condition. The disturbance threshold term described in [61] can be used in the RSC computation to avoid bias in the RSC values because of lack of excitation. To avoid bias in the parameter estimate because of disturbances or noise, the plant input-output pair used in the RSC estimation is filtered using a band pass filter that only allows signals in the frequencies of interest, namely around the loop crossover frequency.

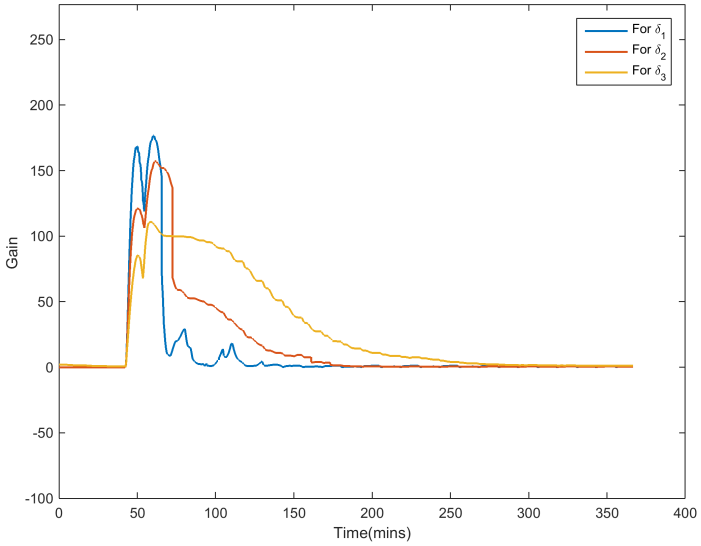

Figure 4.2: RSC plots for different exponential weights $\delta_1 = 2, \delta_2 = 10\delta_3$; Increase in the forgetting factor results in an exponentially weighted 2-norm estimate close to the 2-norm. However, increase in the forgetting factor also results in an increase in the transient time.

This MMAC algorithm is tested using computer simulations, we use same filter bank settings and the same setpoint signals used in the testing of the direct adaptive controller in Section 3.3. The controller gain bank $[K_i]$ of size 20 is formed by spanning gains between 0.01 times and 10 times of the nominal controller gain (gain of the controller C_6). The MMAC produces similar results as the direct adaptive controller and computer simulation results are presented in the next section.

4.2 Multi-model adaptive control test results

It can be seen in Fig. 4.3 and Fig. 4.4 after the set-point transition that the gain of the controller adapts to the steady state and the loop performance is closer to the target. As compared to direct adaptive control, MMAC controller gain convergence takes more time and however, faster convergence can be achieved by adjusting exponential weight(δ) used in the computation of the RSC. However, we observe a small performance degradation, because the controller gain required to match the target is not present in the bank of controllers (Fig. 4.3(e), 4.3(f)) and 4.4(f)).

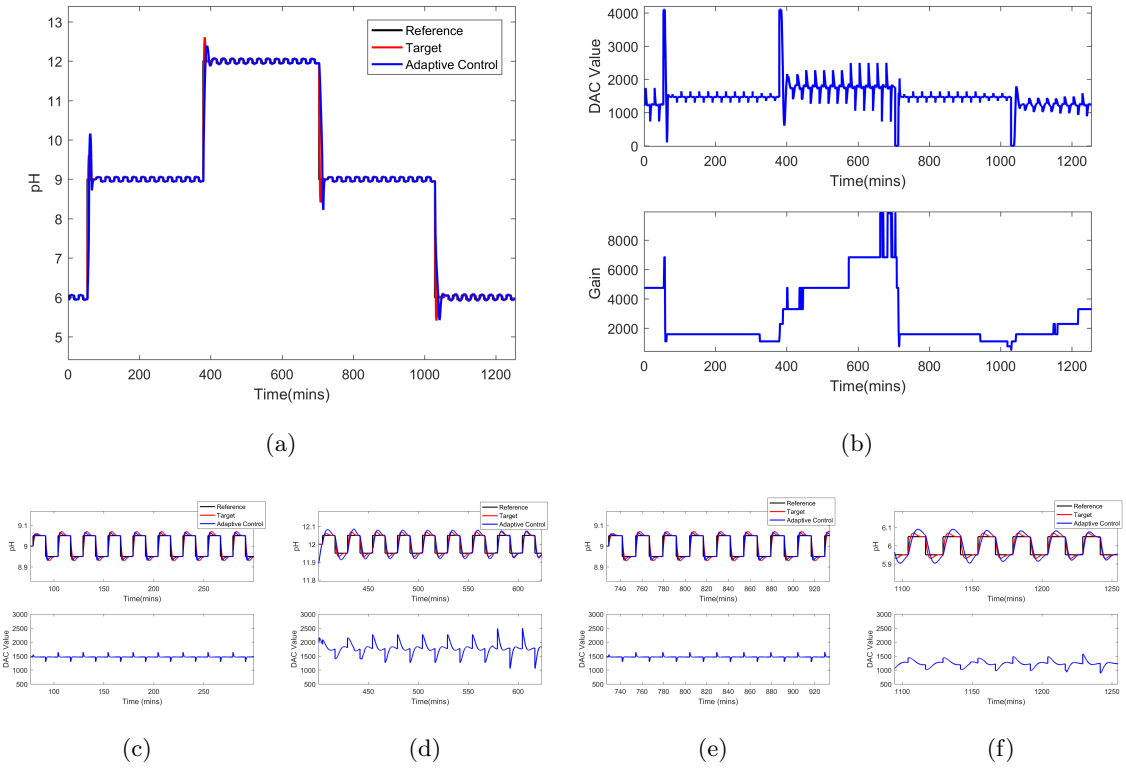

Figure 4.3: Multi-model adaptive pH control results for Case 1 (a) output plot (b) top plot - plant input, bottom plot controller gain (c-f) zoomed in plots of the input output plot after each big step transition; After transients the gain of the controller converges to a value that brings the actual loop close to the target loop. As compared to direct adaptive control, MMAC exhibits somewhat larger transient times and has some mismatch in the controller parameter because of the controller gain quantization.

It can be seen from Fig. 4.5 -4.7, the proposed multimodel adaptive control algorithm has similar performance as the direct adaptive algorithm. In some cases, like in Fig. 4.7(d) it can be seen that there is a mismatch between the target and the actual loop. This mismatch is a result of controller gain quantization. This mismatch can be minimized by increasing number of controller gains in the controller bank. However, larger controller bank results in an increase in the computational power required to implement an adaptive loop. In Fig. 4.7(e) mismatch between the actual and the target response is relatively high. This is because the controller gain hits saturation(lowest gain value of the controller bank). This phenomena also can be avoided by increasing the number and range of the controller gains used in the controller bank. It is also seen from the results that a step signal is not

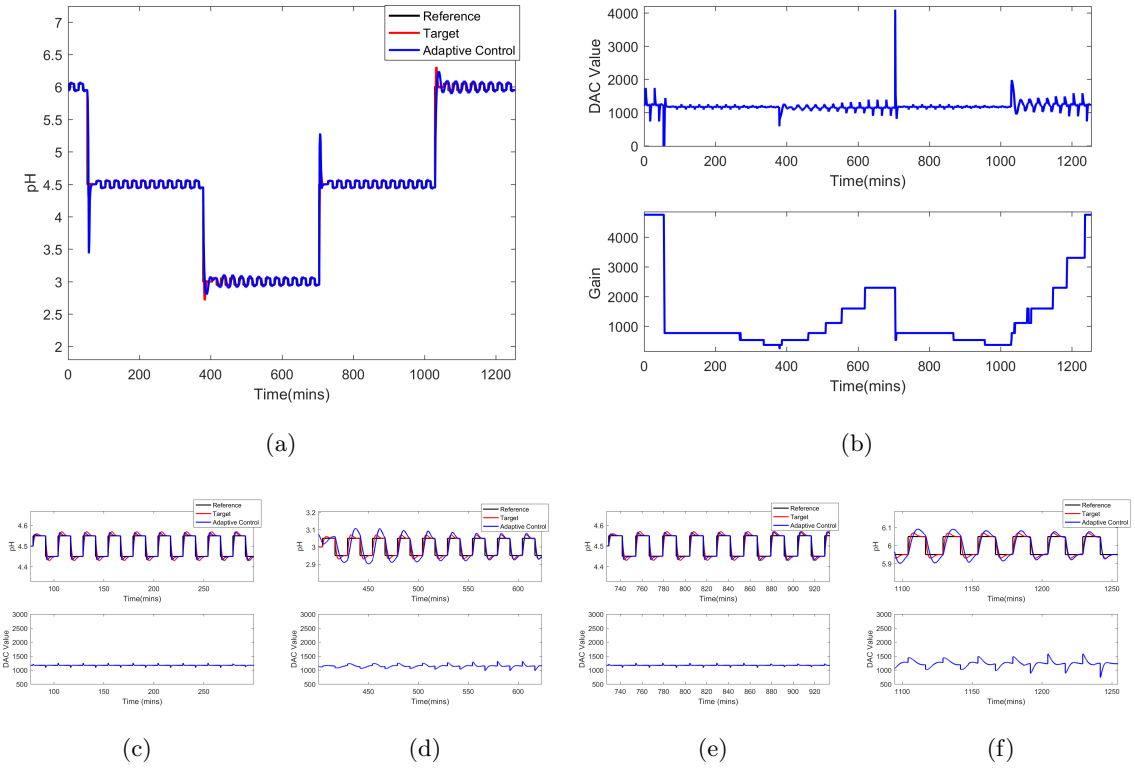

Figure 4.4: Multi-model adaptive pH control results for Case 1 (a) output plot (b) top plot - plant input, bottom plot controller gain (c-f) zoomed in plots of the input output plot after each big step transition; After transients the gain of the controller converges to a value that brings the actual loop close to the target loop. As compared to direct adaptive control, MMAC exhibits somewhat larger transient times and has some mismatch in the controller parameter because of the controller gain quantization.

ideal for the transition between set points.

The above results are representative to all the tested cases, demonstrating that the proposed MMAC algorithm performs reasonably well and achieves uniform performance across the operating range with a variation in buffer flows. Because of its large computational requirements that necessitate a different hardware configuration, it was not tested experimentally. However, it is anticipated its performance will be similar to the direct adaptive controller.

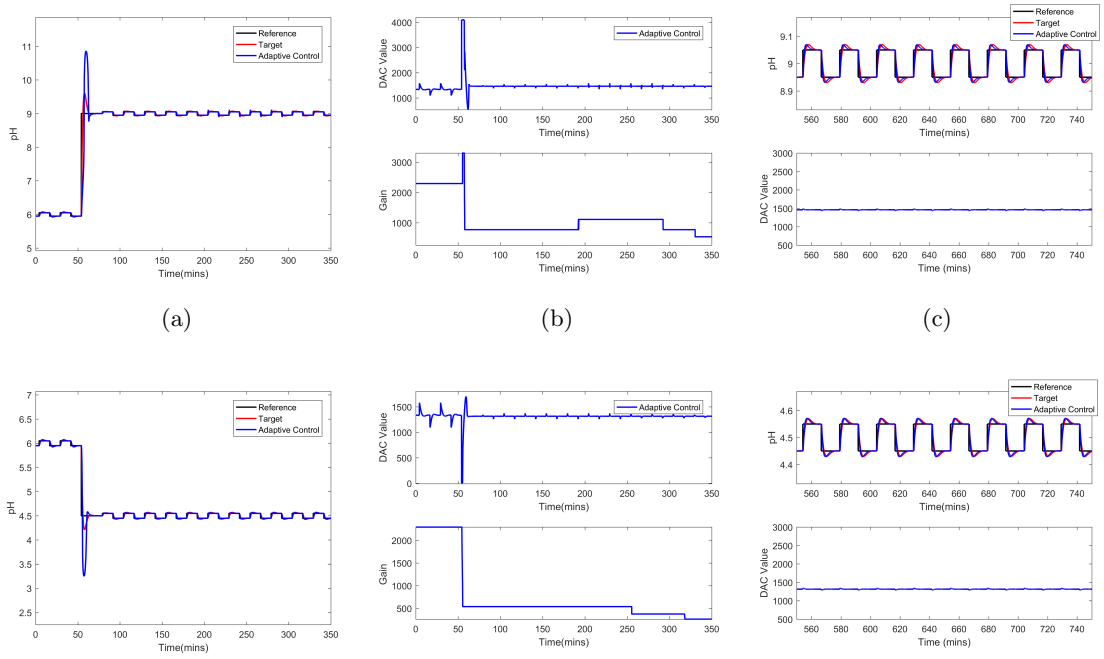

(a) (b) (c)

(d) (e) (f)

Figure 4.5: Multi-model adaptive pH control results for Case 2, (a) and (d) output plots, (b) and (e) top plots- plant input, bottom plots- controller gains(c) and (f) zoomed in plots of the input output plot in (a) and (d) respectively after each big step; With the buffer flow changes the MMAC results in a loop close to the target

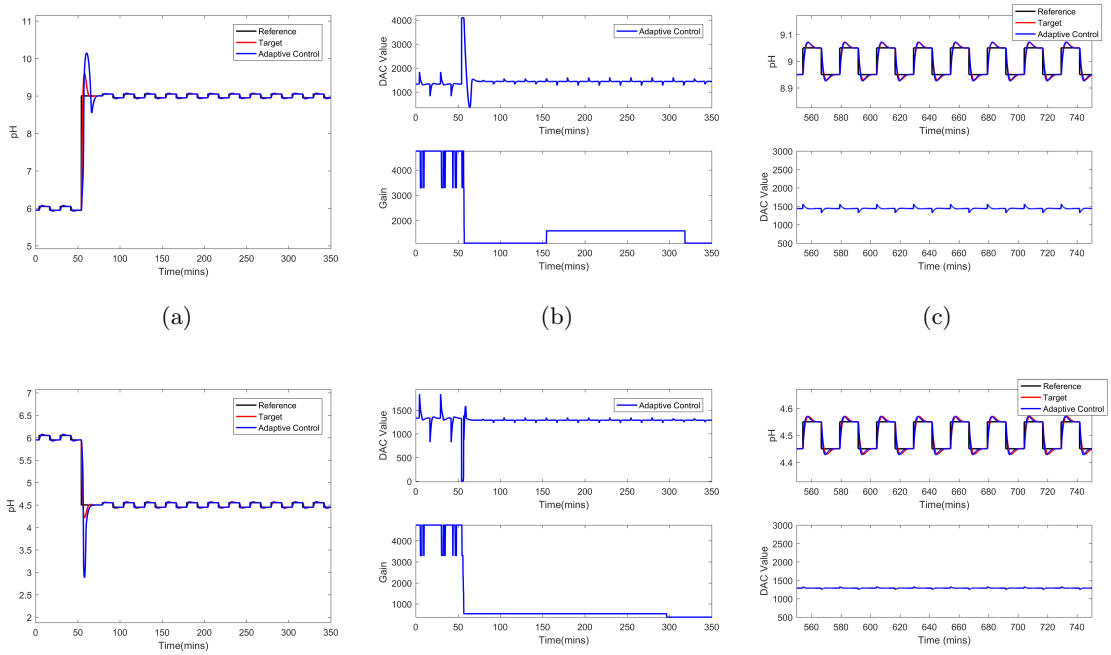

(a) (b) (c)

(d) (e) (f)

Figure 4.6: Multi-model adaptive pH control results for Case 3, (a) and (d) output plots, (b) and (e) top plots- plant input, bottom plots- controller gains(c) and (f) zoomed in plots of the input output plot in (a) and (d) respectively after each big step; With the buffer flow changes the MMAC results in a loop close to the target

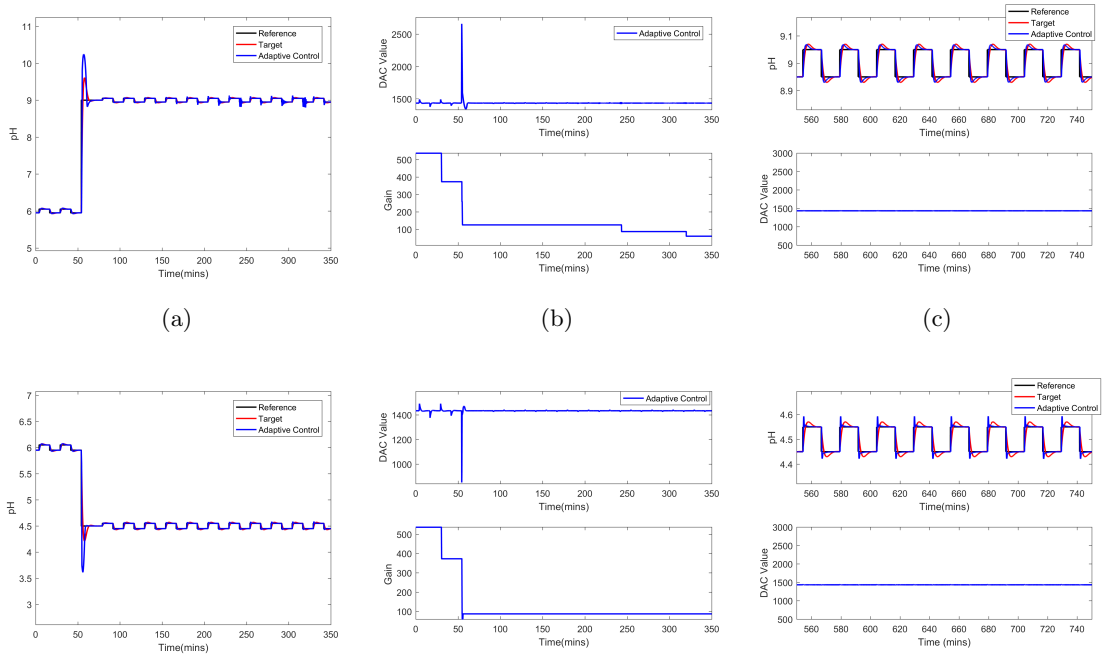

(a) (b) (c)

(d) (e) (f)

Figure 4.7: Multi-model adaptive pH control results for Case 4, (a) and (d) output plots, (b) and (e) top plots- plant input, bottom plots- controller gains(c) and (f) zoomed in plots of the input output plot in (a) and (d) respectively after each big step; With the buffer flow changes the MMAC results in a loop close to the target

Chapter 5

IMPLEMENTATION OF PH CONTROL IN MFC

This chapter focuses on the application of the proposed direct adaptive pH control algorithms to control pH of an MFC anode and study implications of pH control on its performance. Combined activated sludge anaerobic digestion model(CASADM) from [70] is used in this study. First, important details of CASADM model([70]) along with necessary changes for pH control are described. Second, the pH control algorithm implementation details are discussed. Finally, results of pH control along with results that support the improvement of MFC performance with pH control are presented.

5.1 CASADM model

Anaerobic digestion one of the commonly used technology in the improvement of wastewater treatment sustainability. In a typical wastewater treatment plant (WWTP) sludge produced from the primary sedimentation and the activated sludge (AS) processes are sent to the anaerobic digester (AD). In anaerobic digestion, first complex and particulate organic compounds are hydrolyzed to soluble fermentable substrates. Second, these substrates are then fermented by bacteria(acetogenic and acidogenic) to produce acetate, carbon dioxide (CO_2), and hydrogen gas (H_2). The products of fermentation are further consumed by methanogens to produce methane gas(CH_4). Anaerobic digestion not only reduces bio-solids from the sludge but also produces methane gas(CH_4), which can be further used to generate energy.

AD's performance is highly influenced by its solids retention time (SRT) for three reasons. Mainly, slow-growing methanogens, hydrolysis of complex and particulate organic substrates and rates of CH4 production. Extracellular polymeric substances (EPS) and soluble microbial products (SMP) are also important in AS and AD processes with their

fate also strongly depend on SRT. CASADM model helps to understand effects of sludge recycling on AD SRT along with COD removal and methane CH_4 production. A brief description of CASADM model is discussed below.

CASADM is a multi-species, dynamic mathematical model that is used to describe AS-AD processes in different configurations (hybrid and conventional). CASADM components are divided into solids and soluble groups. This model tracks five types of active biomass species of solids group –heterotrophic bacteria, ammonium-oxidizing bacteria(AOB), nitrite-oxidizing bacteria(NOB), fermenting bacteria, and methanogenic Archaea – along with EPS and inert biomass. Influent particulate COD (PCOD) is also one of the solid components. Soluble chemical components included in the model are acetate, soluble COD (SCOD) that excludes acetate, dissolved oxygen, utilization-associated byproducts (UAP), biomass- associated byproducts(BAP), ammonium (NH_4^+), nitrate (NO_3^-), and nitrite(NO_2^-). This model also includes two gas components mainly nitrogen (N_2) and methane(CH_4). CASADM assumes the only acetate is an electron-containing product produced during fermentation and balances the electron equivalents in fermentation reaction without H_2. This is because stoichiometric and kinetic relationships of H_2 production are not defined for SMP and EPS and the consumption of H_2 normally is so rapid that it does not accumulate to a significant level. In terms of mechanisms, CASADM includes hydrolysis of PCOD and EPS; aerobic biodegradation of SCOD, acetate, and SMP; two- step nitrification; denitrification; fermentation; and methanogenesis. To study pH effect on the AS-AD process we consider simplified CASADM model with one tank and important CASADM model settings used in this study are listed in Table 5.1. More details of this model can be found in [70].

In general, AS-AD process makes the output stream acidic and a sample profile of pH is shown in Fig. 5.1

To study pH control effects of CASADM model, a new flow of $1M\ NaOH$ is introduced in the input stream and its flow rate is manipulated to adjust the pH. For control purposes,

Table 5.1: CADADM parameters

Model parameter	Value
Influent flow rate(Q_{in})	1000 L/day
Tank Volume	15000 L
Nominal SRT	20 days
Influent concentrations	
SCOD	322.5 mg/L
PCOD	0 mg/L
Heterotrophs	50 mg/L
AOB	10 mg/L
NOB	1 mg/L
Fermenters	10 mg/L
Methanogens	1 mg/L
Inerts	50 mg/L
Ammonium	60 mg/L
Nitrate	0.2 mg/L
Dissolved oxygen	0.5 mg/L
Dihydrogen Phosphate	10 mg/L
Bicarbonate	200 mg/L
Acetate	5 mg/L

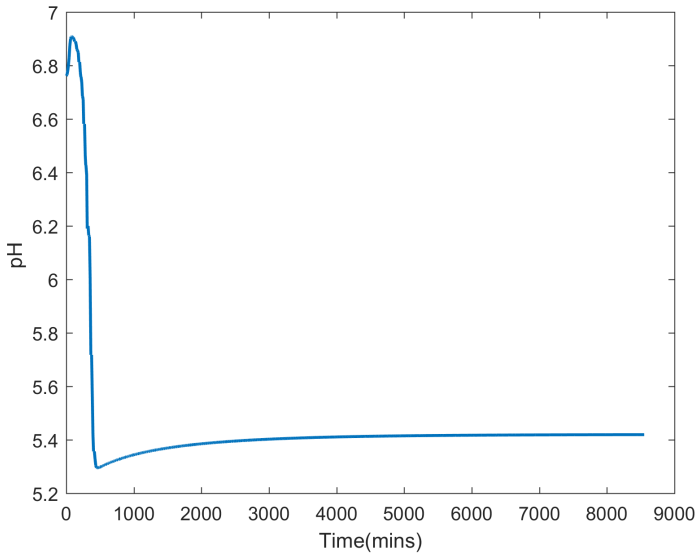

Figure 5.1: pH profile of CASADM model without pH control; It can be seen AS-AD process makes the stream acidic. However, presence of large quantities of buffer stabilizes pH around 5.4

pH is measured every 10 *seconds* and a white noise is added to the pH value to mimic sensor noise. Implementation details of adaptive pH control algorithm for CASADM model are discussed in the next section.

5.2 pH control implementation

This section uses the modified CASADM model to apply the proposed direct adaptive pH control algorithm. The proposed adaptive control requires a nominal plant model, which is obtained by injecting PRBS signal to control $NaOH$ flow around operating pH of 6 and fitting a linear model to the input-output data. Here $NaOH$ flow rate is the plant input and pH reading is the plant output. This step provides an estimate of the plant dynamics, that undergo only small changes with the change of operating conditions.

As described in experimental section of direct adaptive pH control, system identification algorithms from [63] [64][55] [66] and [62] are used to fit model to the data. Uncertainty estimates from the residuals of these algorithm are further used in the selection of specifications for the controller design.

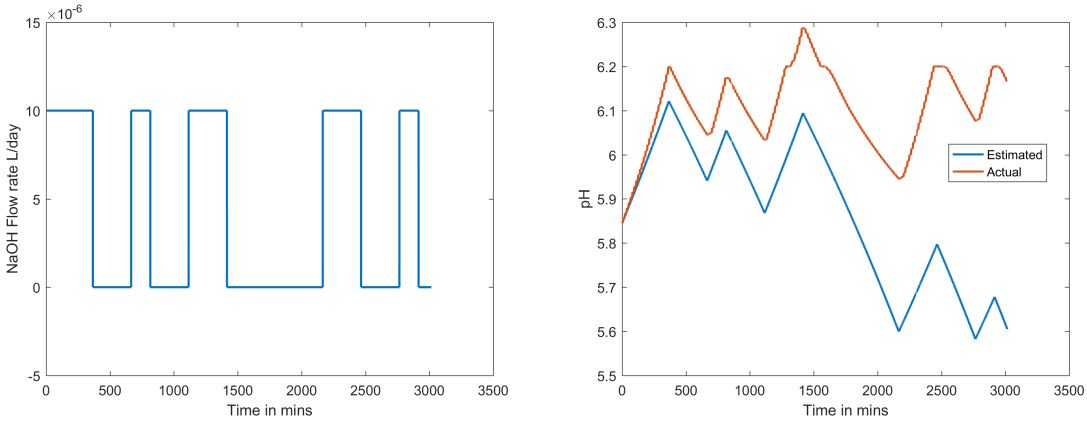

(a) (b)

Figure 5.2: System identification signals (a) input and (b) output(red trace) and predicted output(blue trace)

The identified transfer function $\tilde{G}_6$ is shown below

$$\tilde{G}_6(s) = \frac{3.815 \times 10^{-2}}{s} \tag{5.1}$$

Output responses of the identified model along with the actual output for the PRBS input is shown in Fig. 5.2(b). Because the plant is an integrator, the output of the identified plant drifts away from the actual plant. It can be seen from the multiplicative uncertainty plot bandwidth of $BW = 0.006 rad/min$ is a reasonable choice.

A PI controller ($\tilde{C}_6$) is designed for the plant $\tilde{G}_6$ using an offline FLS algorithm [62] [23]. The target loop was chosen to achieve closed-loop bandwidth specification of 0.006 rad/min based on a linear quadratic regulator optimal loop with integrator augmentation and its transfer function is given below:

$$\tilde{L}_6 = \frac{2.456 \times 10^{-6}(s + 1.134 \times 10^{-6})}{s^2} \tag{5.2}$$

The PI controller parameters of the nominal controller are obtained by minimizing an offline RSC and its transfer function is shown below

$$\tilde{C}_6 = \frac{6.4372 \times 10^{-5}(s + 1.135 \times 10^{-6})}{s} \tag{5.3}$$

Bode magnitude plots of the target loop and the actual loop transfer function are shown in Fig. 5.3(a) and plots are showing a fairly good match. To validate the designed controller,

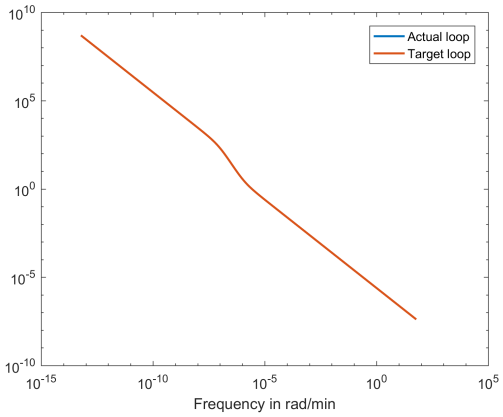

(a)

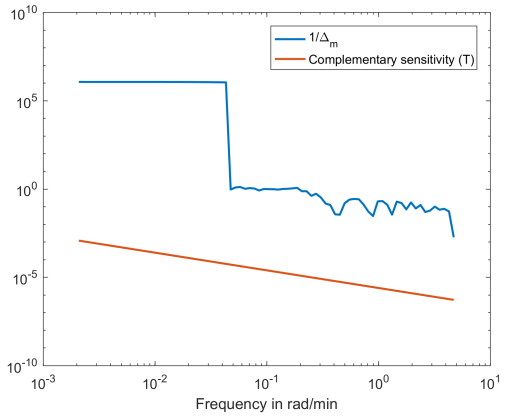

(b)

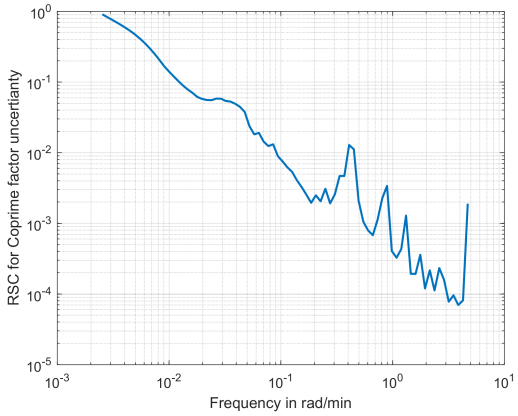

(c)

Figure 5.3: (a) Frequency response of target loop and identified loop transfer functions (b) complementary sensitivity plot (red) with its multiplicative uncertainty bound(blue) obtained in the identification step (c) RSC plot for the nominal controller; The actual loop and the target loop are close as expected. The multiplicative uncertainty provides an approximate bound on the complementary sensitivity and helps in the selection of a closed-loop bandwidth. For the chosen bandwidth of 0.006 rad/min the complementary sensitivity is at the at the constraint. A less conservative estimate, obtained using a coprime factor uncertainty computation, shows that the corresponding RSC (CFRSC) value less than 1 for all frequencies, thereby the designed controller is expected to yield robust closed-loop stability.

a coprime factor uncertainty estimate described in Section 3.2 is used. Fig. 5.3(c) shows an CFRSC value less than 1 for all frequencies, indicating the robust stability of the nominal controller ($\tilde{C}_6$) with respect to the uncertainty arising from the estimation error

For the direct adaptive control experiments, $\tilde{C}_6$ was used as a base controller and the

target loop used in its design ($\tilde{L}_6$) was used as a target loop for the adaptation.

The filter bank was constructed using 5 all-pass filters with corner frequencies spanning the logarithmic interval between $0.1BW$ to $10BW$, where BW is the bandwidth of target loop. The gain values of $[6.4372 \times 10^{-6}, 6.4372 \times 10^{-4}]$ were used as lower and upper limits of K respectively. A forgetting factor of 0.9999 was used.

Results from the closed-loop simulations along with its effect on MFC operation is described in the next section.

5.3 Results

This section presents pH tracking results of the proposed algorithm around pH 6. A square wave is injected at the reference to provide excitation for the adaptation. Tracking results from the simulations are shown in Fig. 5.4. It can be seen from the pH tracking results(Fig. 5.4(a)) it took about 300000 mins for the initial transients to die and this is because of the saturation in the plant input Fig. 5.4(b). This also results in the parameter saturation of the controller gain for this period and it can be noticed in Fig. 5.4(c). Overall the proposed pH control algorithm controls pH close to the set-point

To study the effect of pH control on CASADM operation all 44 state components of this model with pH control are compared against the model without pH control. It has been noticed most of the components look similar in both cases. This is because pH variation in the case without pH control is minimal(Fig. 5.1). However, a small improvement is noticed in the methane(CH_4) production. Plots of methane concentration for the cases with pH control and without pH control are shown in Fig. 5.5. The CASADM model used for this study has high resting time with majority activity carried during the start of the process. So increase in the methane production can also be attributed to initial transients in pH.

With this result, we conclude inclusion of pH control in CASADM improves methane production sightly. In the case of CASADM model with less buffer, pH of the process can drop significantly (instead of settling around 5.4) and pH control for this case can give more tangible benefits in terms of its efficiency.

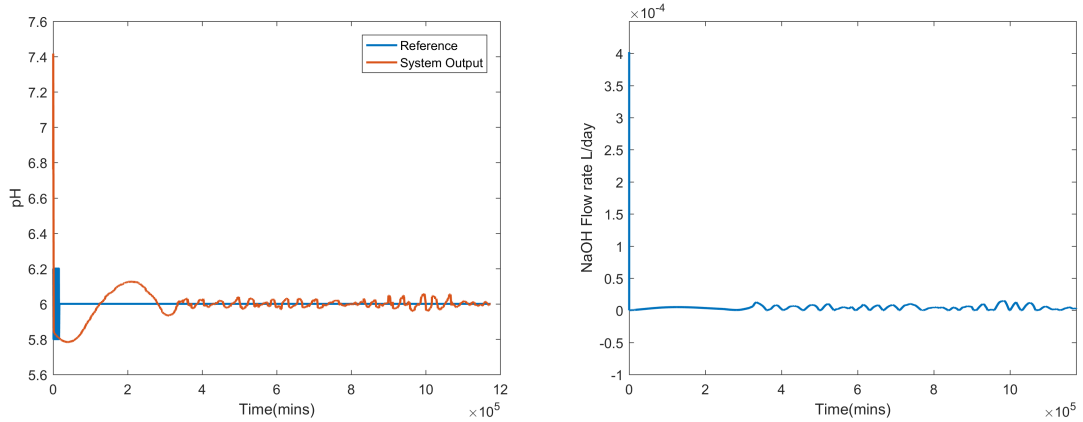

(a) (b)

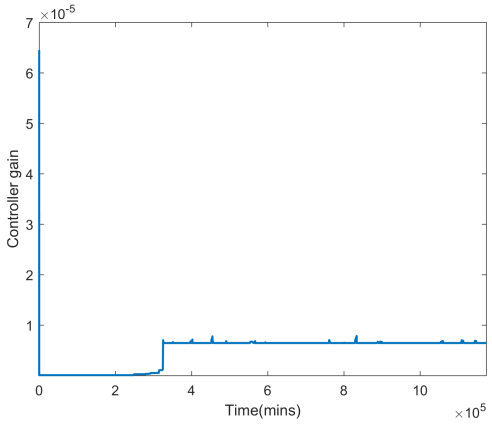

(c)

Figure 5.4: (a) Output pH plot(red) of the plant for a set point(blue) (b) input $NaOH$ flow plot (c) Controller gain plot; pH plot shows large transient time this is because of the saturation in the plant input. This also causes saturation in the controller gain during the initial transient

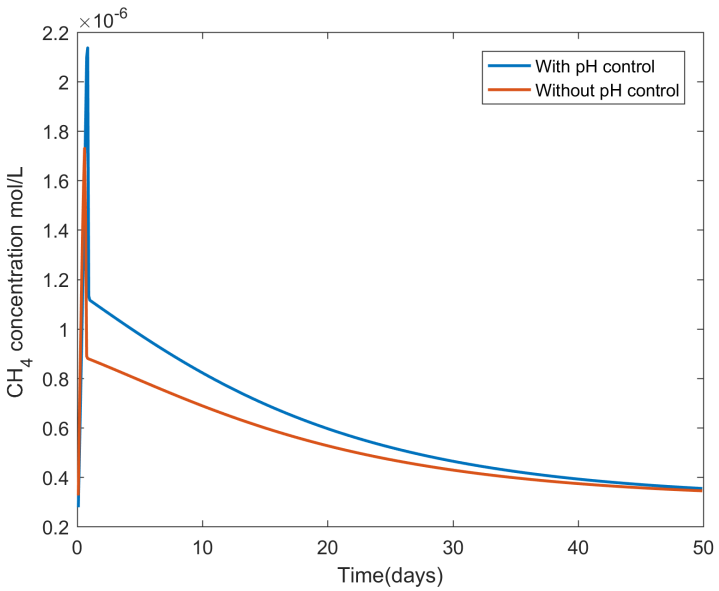

Figure 5.5: Plots of methane(CH_4) concentration in the reactor for the case without pH control (red) and for the case with pH controlled at 6 (blue); It can be seen CASADM model with pH controlled at 6 produces more methane as compared to a CASADM model without pH control

Chapter 6

GUIDELINES FOR INDUSTRIAL IMPLEMENTATION

One of the weaknesses in the usage of the proposed adaptive control algorithms for industrial implementations is in step set-point transitions where the gain changes dramatically and large overshoots are obtained. A potential common remedy is in restricting the rate of change in the set-point, e.g., with ramp transitions, to reduce the frequency content of the reference signal and allow more time for the adaptation to catch up. Ramp signal transition behaves similarly to a step signal transition with a pre-filter. Our simulations, however, indicate that at the end of the ramp the excitation presented to the estimator is not sufficient to identify the process gain at the new operating conditions, leaving the door open for subsequent poor performance. For this reason, and since the controller is already in a transient regime, we propose to include a logic in the supervisory loop to inject small amplitude excitation around the crossover frequency together with the ramp change in the set-point. The injected excitation can be stopped automatically when the gain estimates become reliable, based on the optimal RSC value. The implementation of such a strategy shows indeed a dramatic reduction in overshoot, as well as the convergence of the controller gain at the end of the transition between operating points, as shown in Fig. 6.1 and Fig. 6.2.

Unfortunately, the same remedy cannot provide adaptation convergence for changing buffer capacity. For this case, we can only include a supervisory logic that injects excitation whenever the RSC estimate used in the cost objective grows either due to disturbances or gain drifts. In both cases, the amplitude of the injected excitation and the associated variation of the pH are kept small so that they do not degrade the performance significantly.

In some cases of buffer flow changes, as in Fig. 1.3, the loop instability provides required excitation for the adaptation. The controller gain adapts to a value that stabilizes the

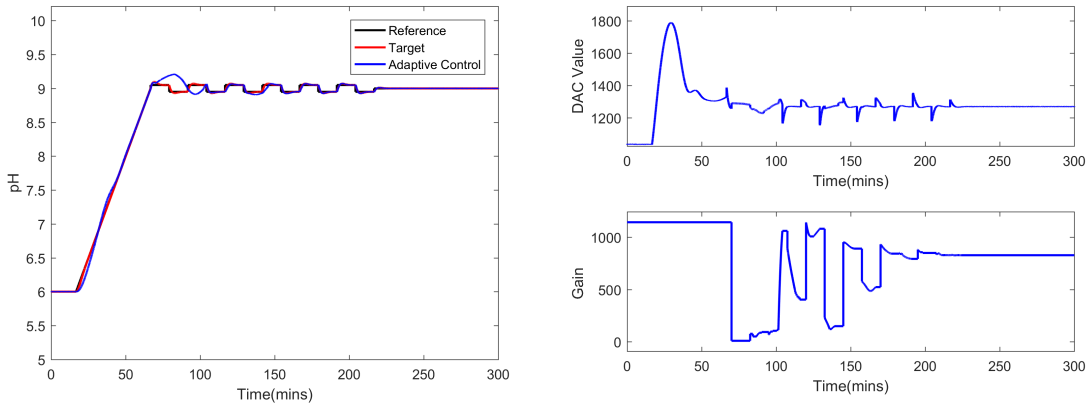

(a) (b)

Figure 6.1: Direct adaptive pH control for the ramp transition signal (a) output plot;output signals include reference (black trace), target loop (red), actual (blue) (b) top plot- plant input, bottom plot- controller gain; Overshoot in the output is minimal and the supplied excitation is sufficient for the convergence of the controller gain parameter.

closed-loop. Example of this phenomenon for direct adaptive control Fig. 6.3.

The optimal RSC value is a good signal in process performance monitoring for the supervisory control. All the performance monitoring guidelines explained in the paper [61] can be extended with proposed algorithms in the implementation of supervisory control using the optimal RSC value.

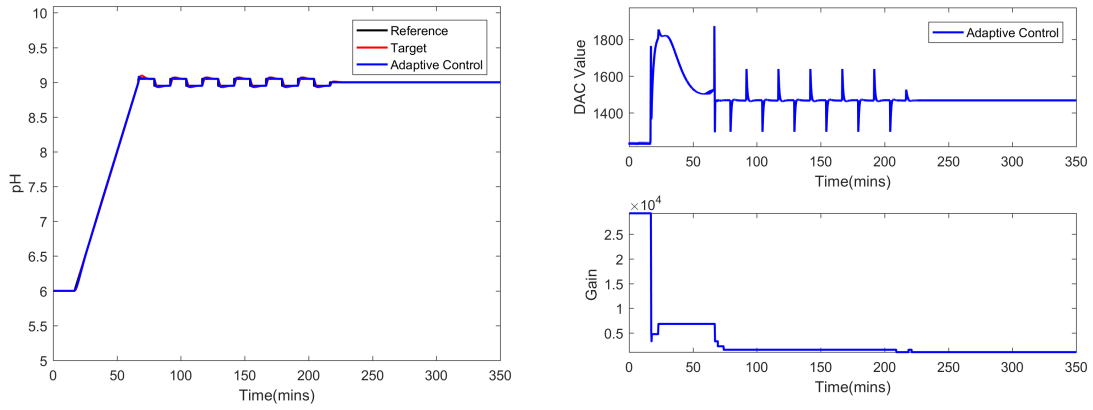

(a) (b)

Figure 6.2: Multi-model adaptive pH control for the ramp transition signal (a) output plot; output signals include reference (black trace), target loop (red), actual (blue) (b) top plot- plant input, bottom plot- controller gain; Overshoot in the output is minimal and the supplied excitation is sufficient for the convergence of the controller gain parameter.

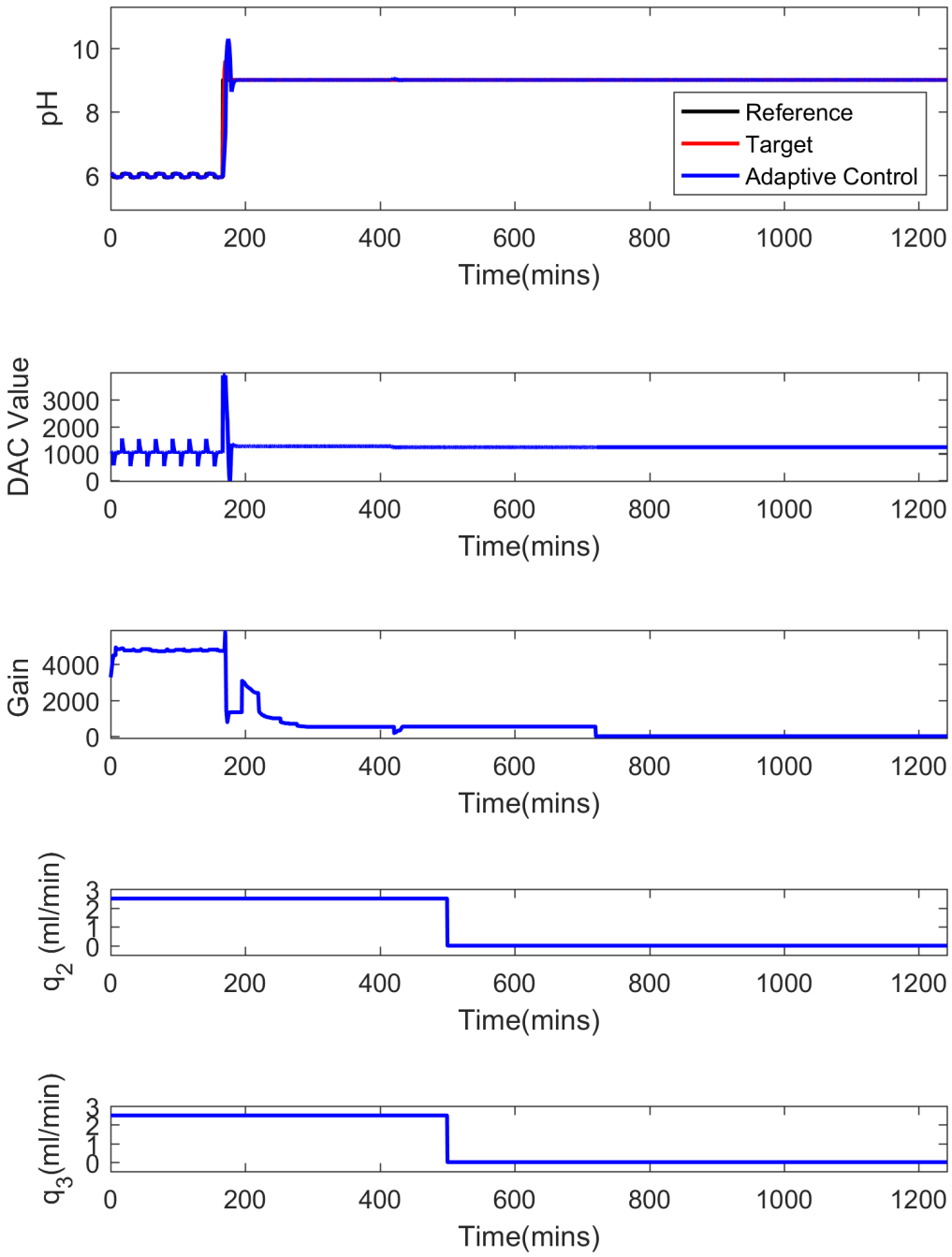

Figure 6.3: Direct adaptive pH control results for the buffer flow Case1 to Case 4 transition, establishing effectiveness of controller gain adaptation for buffer flow changes: top to bottom- plant output, plant input, controller gain and buffer flow plots; output signals include reference (black trace), target loop (red), actual (blue) ; As compared to Case 1, Case 4 has larger variation in the plant gain and the proposed direct adaptive control algorithm is able to adapt controller gain accordingly.

Chapter 7

LOW-COST POTENTIOSTAT

The main purpose of a potentiostat is to regulate the potential of a working electrode with respect to a reference electrode potential at a specified set-point. There are many analytical grade potentiostats readily available in the market, however, they are bulky and their unit cost is very high. To tackle this problem in this chapter we propose a new low-cost and portable potentiostat alternative. First, construction details of this potentiostat are discussed in detail. Second, the proposed potentiostat is tested for set-point tracking using a ferricyanide reactor. The same ferricyanide reactor is also used to obtain set-point tracking data for an analytical grade potentiostat. We study both set-point tracking test results by comparing their accuracy and speed. Using these results trade-offs between the proposed potentiostat and an analytical grade potentiostat are discussed. Finally, the proposed potentiostat is tested for its tracking performance when delivering high current using 1-ohm resistance and corresponding test results are presented.

7.1 Low-cost potentiostat construction

Schematic diagram of the proposed low-cost potentiostat is shown in Fig.7.1, we can divide it broadly into two groups mainly digital and analog. The digital side consists of an analog to digital converter (ADC), a digital to analog converter (DAC), a microcontroller (Arduino Mega) and a personal computer. Personal computer(PC) or equivalent is mainly used to send set-points to the microcontroller and to perform data acquisition, data storage, and data visualization tasks. The microcontroller receives potentiostat set-point from the PC and sends readings of the working electrode voltage, the reference electrode voltage and current between the anode and cathode back to the PC for the purpose of logging. The microcontroller and the PC communicate using UART serial communication with

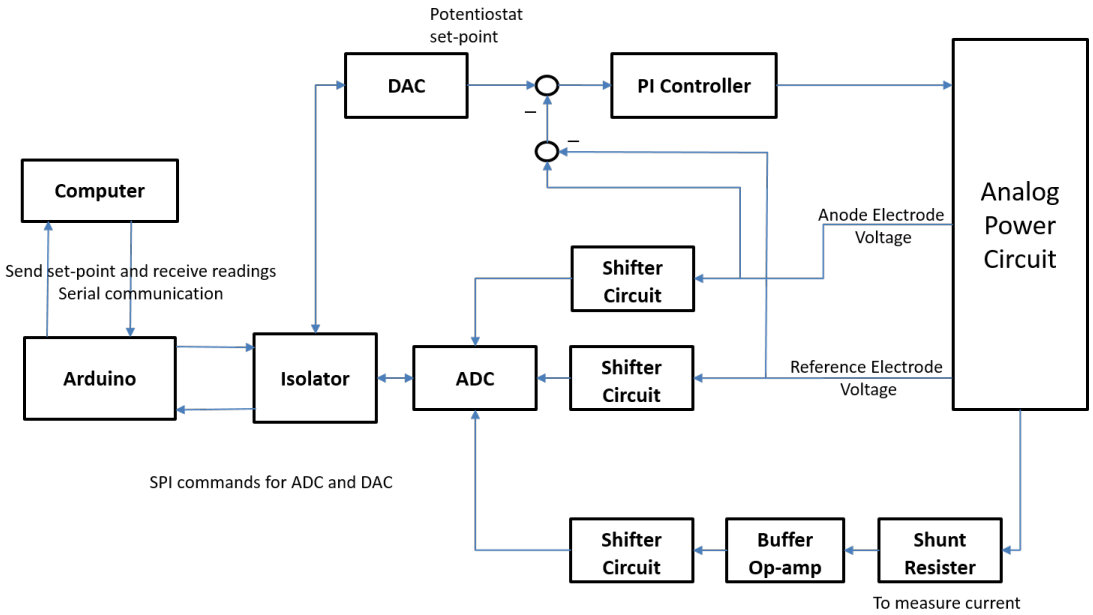

Figure 7.1: Schematic diagram of the proposed low-cost potentiostat

a baud rate of 115200. Both ADC and DAC are powered using the regulated voltage generated by the analog power circuit. Their main purpose is to interface analog side of the potentiostat with the microcontroller and they communicate with the microcontroller using SPI communication protocol. Because they are powered using different voltage levels(generated from the analog power circuit), SPI communication between the ADC/DAC and the microcontroller is digitally isolated using an isolator(IC ADUM7641). An integrated circuit(IC) ADS1248 is used as the ADC and another IC AD5752R is used as the DAC. The ADS1248 is a 24 bit ADC with 8 differential channels and it can support sampling rate up to 2000 samples/sec. The AD5752R is a 16 bit DAC with 2 channels and it can support sampling rate up to 10 mega samples/sec.

The analog circuit is divided into three parts, an analog power circuit, a PI controller and shifter circuits. The analog power circuit converts a unipolar voltage source into bipolar voltage source, it translates an anode set-point voltage to an equivalent signal that is capable of driving current between the anode and the cathode, and it also generates a regulated +5V voltage signal(used to power ADC and DAC). To keep the cost low, we used a single

unipolar voltage source and convert it to a bipolar voltage source by generating a floating ground. The floating ground terminal is created using a voltage divider(R7 and R8) circuit along with an op-amp(LM358N-IC1B) and power transistors(TIP125-Q2 and TIP122-T2), details of this can be seen in Fig. 7.2. The anode setpoint from the PI controller is converted to a signal that can drive high current between the anode and the cathode using a Darlington pair. This Darlington pair is chosen based on the unit impedance and current supply requirements. The current between the anode and the cathode is driven by either the PNP Darlington pair or the NPN Darlington pair (TIP122 or TIP125) depending on the polarity of the set-point. A shunt resistor of 1 ohm is used to measure the current between the anode and the cathode and a snippet of the power circuit is shown in Fig. 7.2. This analog power circuit also generates a regulated DV_{DD}(+5V) using LM7805 voltage regulator powered using V+ and floating ground. Finally, the anode(working electrode), the reference electrode and the current signals are sent to shifter circuits to bring them into the range of ADC for sampling.

Shifter circuits are mainly used to bring the voltage signals into the ADC range for sampling. In the proposed potentiostat we use a unipolar ADC with the range of 0 to 5V however, our voltage signals (working/reference electrode) are bipolar with the voltage between -2.5V to +2.5V. The shifter circuit brings signals from -2.5V - +2.5V range to 0V - +5V and the circuit diagram of the shifter circuit is shown in Fig. 7.3. This shifter circuit requires a reference voltage of +2.5V to do voltage translation and it is derived from the buffered DAC reference signal(which is +2.5V). To restrict all the signals going into the ADC strictly in the ADC range a rail to rail op-amp TLV2470C powered with 0V-5V is used.

A op-amp based PI controller regulate the potential of the working electrode with respect to the reference close to the potentiostat set-point. The PI controller generates anode set-point that minimizes the tracking error $e(S-(R-A))$, where S, R, and A are potentiostat's set-point, reference electrode voltage and anode voltage respectively. This PI

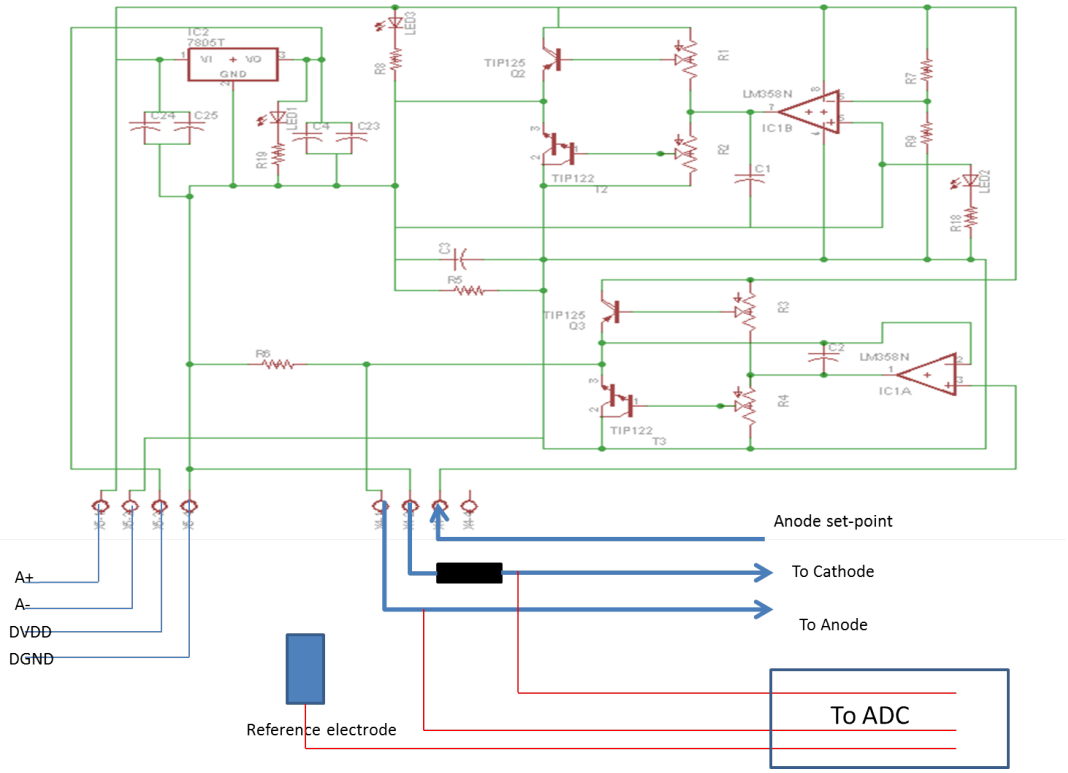

Figure 7.2: Circuit diagram of the analog power circuit

controller along with the summation block is built using op-amps and the circuit diagram of the PI controller with the summation block is shown in Fig. 7.4. The proportional gain(K_p) of the PI controller is chosen as 1 and the integral gain (K_i) of the PI controller is chosen as 83.22(justification for this choice is discussed in Section 7.2).

The proposed potentiostat is tested for set-point tracking and test results are discussed in the next section.

7.2 Test results

Now onwards, the potentiostat input means anode potential and the potentiostat output means anode-reference electrode potential. To analyze the dynamics of the system(input-output characteristics of a ferricyanide reactor), we performed some system identification experiments using pseudo-random binary sequence (PRBS) inputs and the anode voltage readings with respect to the reference electrode(anode-reference voltage) are

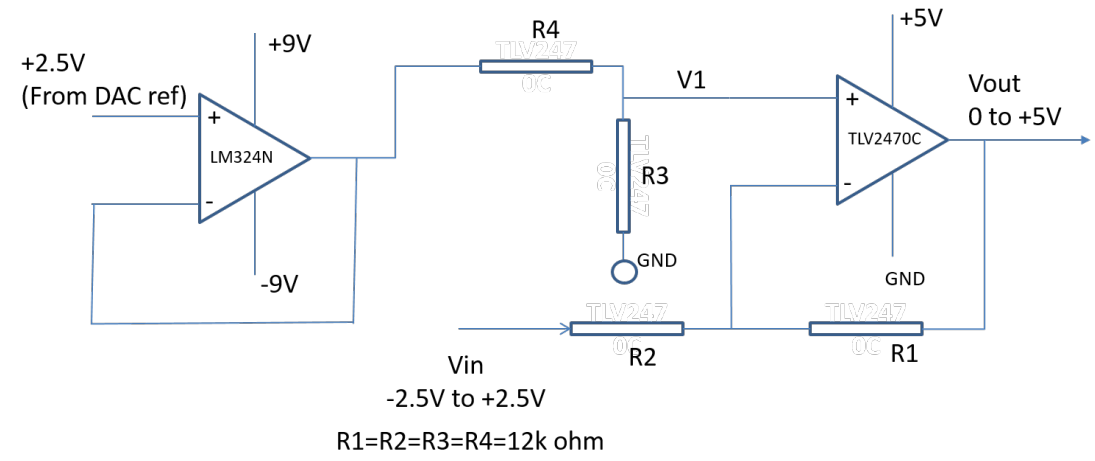

Figure 7.3: Circuit diagram of the analog shifter circuit

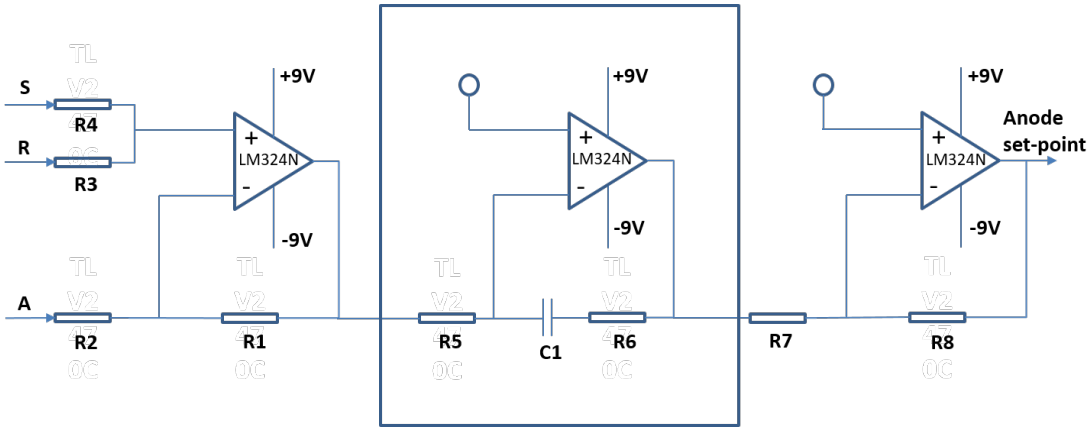

Figure 7.4: Circuit diagram of the analog PI controller

measured. Input-output plots of the data obtained using system identification experiments with various PRBS settings are shown in Fig. 7.5.

We fit a linear model for the a system identification data set. Input-output plot along with the estimated output plot is shown in Fig. 7.6.

Transfer function of the identified plant is listed below

$$P = \frac{0.88452(s + 1.916)}{(s + 1.917)} \tag{7.1}$$

The above transfer function has near left half plane pole-zero cancellation(can be approximated as a constant). This confirms there are very little dynamics between input(Anode set-point) and output(Anode-Reference) of the system, thereby it can

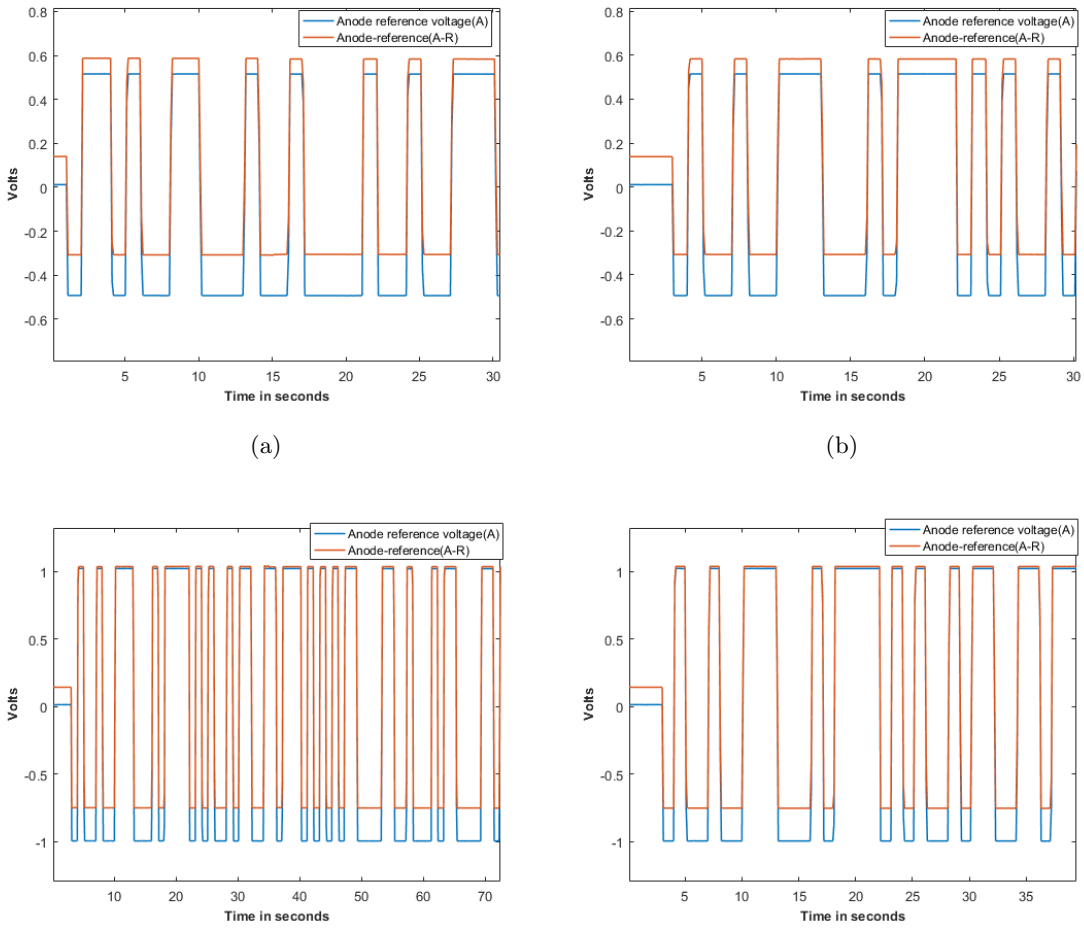

Figure 7.5: Input(Anode set-point)-output(Anode-Reference) plots from various system identification experiments

be confirmed that the proposed proportional and integral gains produce satisfactory performance.

The closed-loop system with the PI controller is tested for set-point changes and closed-loop set-point tracking plots are shown in Fig. 7.7. It can be seen from these plots the PI controller tracks the potentiostat set-point fairly well, however, there is a small bias in the anode-reference potential as compared to potentiostat set-point. Upon investigation, it is found this bias is a result of discrepancies in the shifter circuit used in the measurement of potentials and it can be fixed easily by calibrating measurements.

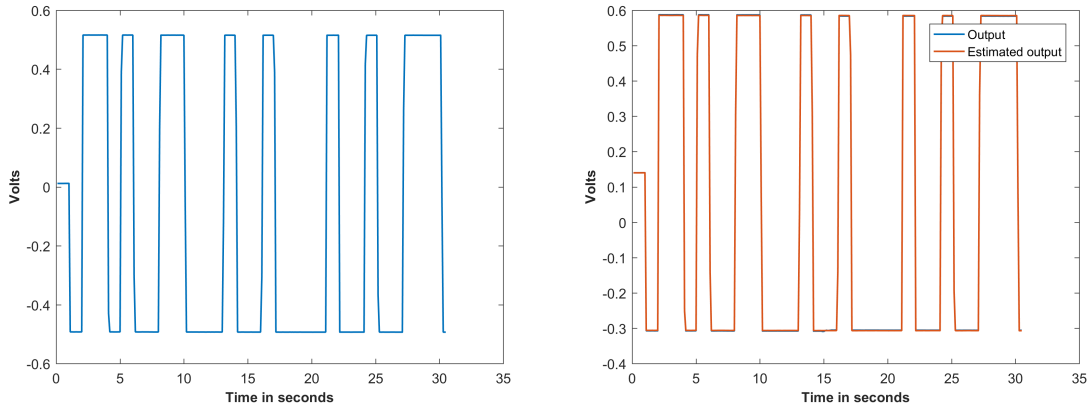

(a) (b)

Figure 7.6: System identification input-output plots with the estimated output generated using identified plant model

To test set-point tracking properties of the proposed potentiating under high current conditions we use 1-ohm resistor as load and reference and cathode potentials are kept constant. Results from these tests are shown in Fig. 7.8. It can be seen from these plots the designed potentiostat track set-point reasonably well. They also have a small offset, causes for these offsets and possible remedies are already discussed in the ferricyanide reactor set-point tracking case.

To evaluate the performance of our potentiostat, we compare the accuracy of potential measurements with an analytical grade potentiostat (Biologic-vmp3). Biologic-vmp3 is made to drive the same ferricyanide reactor with the same set-points used in the proposed potentiostat testing. Fig. 7.9 shows cathode potential plots of the proposed potentiostat and Biologic-vmp3 potentiostat at various potentiostat set-points.

It can be seen from the plots in Fig. 7.9 our potentiostat performs reasonably well in tracking set-points as compared to an analytical grade potentiostat. There is an offset in our potentiostat response, this is a result of the shifter circuit and a variation in the reference electrode potential over time. Some of the bias can be corrected by calibrating potentiostat measurements. Statistical analysis of the proposed potentiostat performance is discussed in the next paragraph.

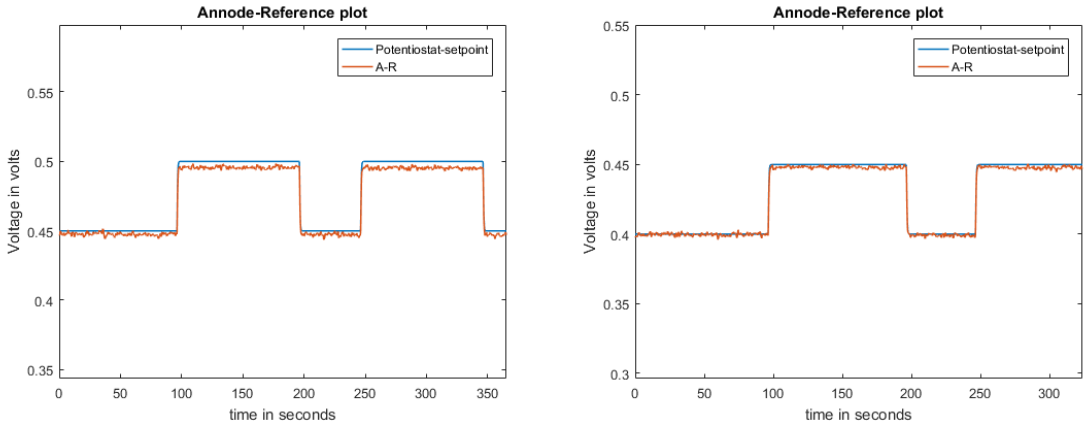

(a)

(b)

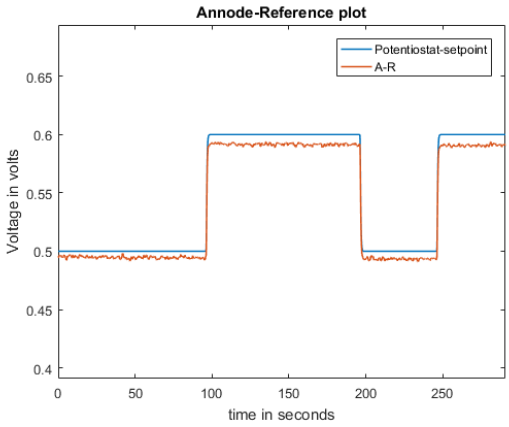

(c)

Figure 7.7: Potentiostat closed loop set-point tracking results; It can be seen for these plots the proposed potentiostat PI controller tracks set-points fairly well, however, there is a small bias in the output and this is a result of discrepancies in the resistor values used in the shifter circuits

This potentiostat used an analog to digital converter (ADC) with an effective resolution of 17 bits and a range of 0 to 2.048 V to measure potentials of the anode and the reference electrodes. This means ADC least significant bit (LSB) represents a voltage of $1.5625 \times 10^{-5}V$. If the ADC quantization error is modeled as a uniform random variable [-0.5LSB, +0.5LSB], then the standard deviation of an ADC voltage reading resulting from the quantization is $4.5105 \times 10^{-5}V$ and it is a theoretical lower bound on the standard deviation of actual voltage measurements. Table 7.1 shows the standard deviation of the

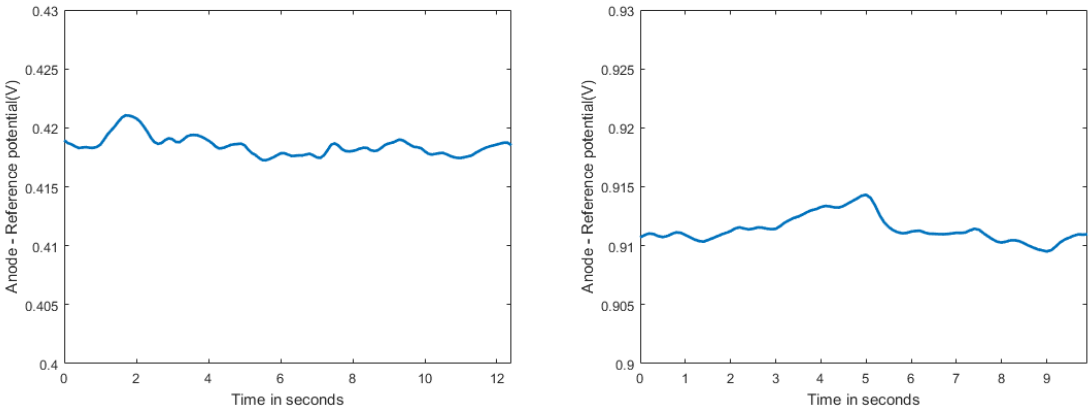

(a) (b)

Figure 7.8: Potentiostat closed loop set-point tracking results with 1 ohm resister as load(a) 0.5 V set-point (b) 1 V set point; It can be seen for these plots the proposed potentiostat PI controller tracks set-points fairly well

cathode potential readings, it can be observed their values are higher than theoretical value (standard deviation because of quantization); this is a result of the presence of external noise. Effect of external noise can be decreased by migrating our potentiostat's analog circuit to a better electrically insulated printed circuit board (PCB).

As compared to Biologic-vmp3 cathode potential measurements, the standard deviation of our potential is slightly higher this means the proposed potentiostat is less accurate as compared to Biologic-vmp3. Even though the analytical grade potentiostat is more accurate(standard deviation values of voltage readings of the analytical grade potentiostat are less than our potentiostat) and can sample potentials faster than the potentiostat we designed, the cost of the analytical grade potentiostat is significantly higher than the potentiostat we designed ($6000 vs $200). Also less accurate voltage measurements, not necessary means bad tracking performance as we only use them for the data logging not in the controller algorithm (PI controller is implemented using an analog circuit). Analog PI controller also enables us to use lower sampling rates without sacrificing performance and sampling rate of 1 $sample/sec$ is a reasonable choice for signal monitoring and logging purposes.

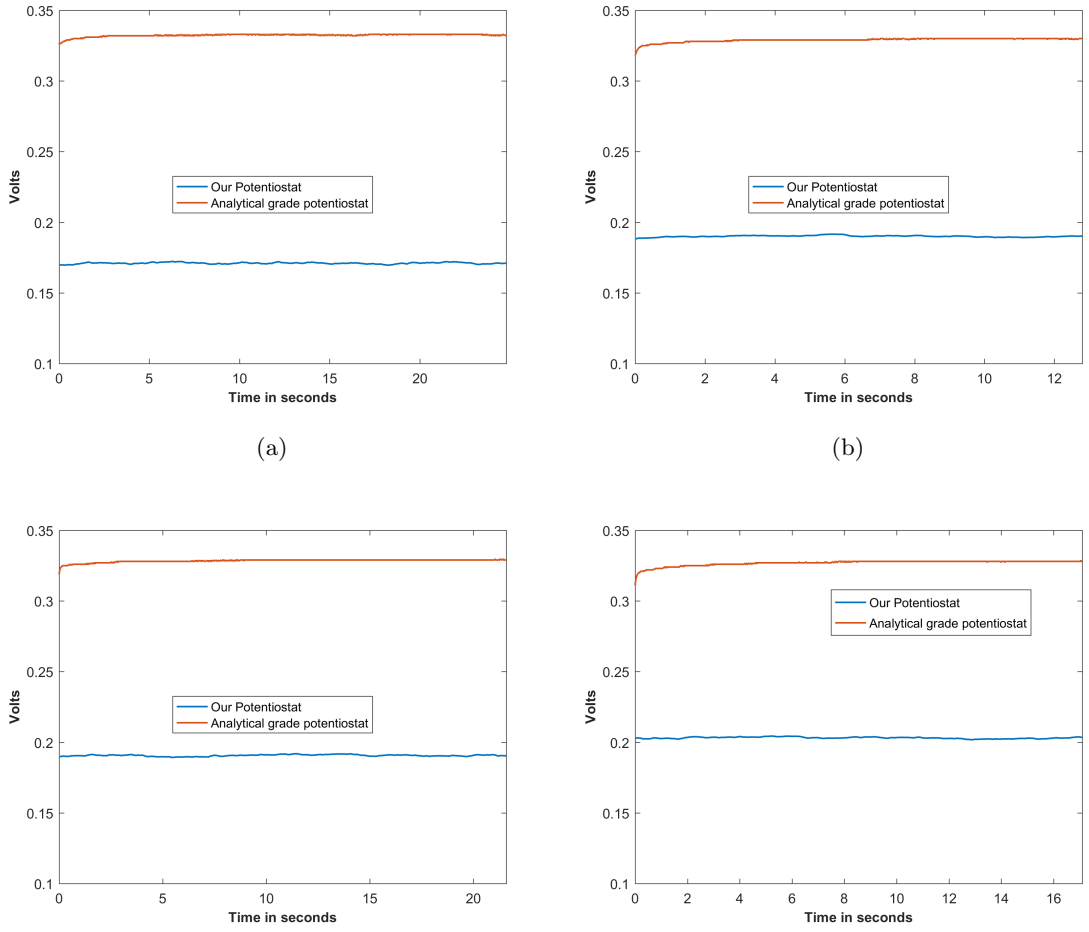

Figure 7.9: Cathode electrode potential plots (a) for the potentiostat set-point of 0.4 V, (b) for the potentiostat set-point of 0.45 V, (c) for the potentiostat set-point of 0.5 V, (d) for the potentiostat set-point of 0.6 V.

Table 7.1: Standard deviation of cathode potential measurements

Potentiostat set-point(V)	Our potentiostat(V)	Analytical grade potentiostat(V)
0.4	5.5575×10^{-4}	4.3489×10^{-4}
0.45	5.9654×10^{-4}	4.1844×10^{-4}
0.5	5.9194×10^{-4}	3.5317×10^{-4}
0.6	5.8798×10^{-4}	4.4608×10^{-4}

Chapter 8

CONCLUSIONS AND FUTURE DIRECTIONS

A pH neutralization process with high retention time is studied in detail and it is shown that only the gain of the plant changes significantly with the operating point and the buffering capacity. The gain change is so large that the usual process delays caused by pump actuators and sensor sampling can cause instability with a fixed or a scheduled controller that does not account for buffering changes, as shown in Fig. 1.3. To avoid an excessive performance degradation with a conservative controller gain selection, two formulations of adaptive control, a direct adaptive and a multi-model switching controller are investigated as solutions of the control problem.

In both cases, the PI controllers are tuned using a frequency loop shaping objective and the online optimization based on the approximation of a H_∞ robust stability condition from input-output data. It is shown from the results of the comparative study show the proposed H_∞ norm based adaptation is less susceptible to the properties of excitation signals as compared to the commonly used L_2 norm based adaptation. Lab scale experiments are used to develop a hardware implementation procedure for the proposed algorithm, where information from the system identification and uncertainty estimation is used in the selection of the target loop shape. Experimental and computer simulation results indicate that the two adaptive controllers can provide similar, practically acceptable performance over a wide operating range.

A CASADM model of an MFC is studied and modified to include base flow (for pH control). The proposed direct adaptive control algorithm is applied to perform pH control of this model and it is shown pH control helps in the improvement of methane production rate.

For an industrial implementation of these controllers, it is recommended that changes

of the set-point must be performed under a ramp constraint to avoid excessive overshoots. Furthermore, a supervisory loop should be included to provide a logic for the acceptance of the gain estimates and the injection of small amplitude excitation in case that they become unreliable due to noise or disturbances.

In this dissertation, we also show that, in the typical industrial environment, the proposed potentiostat performance is practically similar to an analytical grade potentiostat. The trade-offs between the proposed potentiostat and an analytical grade potentiostat are also discussed. Moreover, separation of analog, digital and processor hardware parts makes the potentiostat design flexible.

REFERENCES

[1] Al-Duwaish, H. and W. Naeem, "Nonlinear model predictive control of Hammerstein and Wiener models using genetic algorithms", in "Control Applications, 2001. (CCA '01). Proceedings of the 2001 IEEE International Conference on", pp. 465–469 (2001).

[2] Alvarez, H., C. Londoño, F. di Sciascio and R. Carelli, "pH neutralization process as a benchmark for testing nonlinear controllers", Industrial & engineering chemistry research **40**, 11, 2467–2473 (2001).

[3] Anderson, B. D., T. S. Brinsmead, F. De Bruyne, J. Hespanha, D. Liberzon and A. S. Morse, "Multiple model adaptive control. part 1: Finite controller coverings", International Journal of Robust and Nonlinear Control **10**, 11-12, 909–929 (2000).

[4] Anderson, B. D. O., T. Brinsmead, D. Liberzon and A. Stephen Morse, "Multiple model adaptive control with safe switching", International Journal of Adaptive Control and Signal Processing **15**, 5, 445–470 (2001).

[5] Arends, J. B., S. Van Denhouwe, W. Verstraete, N. Boon and K. Rabaey, "Enhanced disinfection of wastewater by combining wetland treatment with bioelectrochemical H_2O_2 production", Bioresource technology **155**, 352–358 (2014).

[6] Åström, K. J. and T. Hägglund, *PID controllers: theory, design, and tuning*, vol. 2 (Instrument society of America Research Triangle Park, NC, 1995).

[7] Åström, K. J. and T. Hägglund, "Advanced PID control", in "The Instrumentation, Systems, and Automation Society", (Citeseer, 2006).

[8] Bashivan, P. and A. Fatehi, "Improved switching for multiple model adaptive controller in noisy environment", Journal of Process Control **22**, 2, 390 – 396 (2012).

[9] Böling, J. M., D. E. Seborg and J. P. Hespanha, "Multi-model adaptive control of a simulated pH neutralization process", Control Engineering Practice **15**, 6, 663 – 672 (2007).

[10] Buchstaller, D. and M. French, "Robust stability for multiple model adaptive control: Part i - the framework", IEEE Transactions on Automatic Control **61**, 3, 677–692 (2016).

[11] Buchstaller, D. and M. French, "Robust stability for multiple model adaptive control: Part ii- gain bounds", IEEE Transactions on Automatic Control **61**, 3, 693–708 (2016).

[12] Chen, J.-y., N. Li and L. Zhao, "Three-dimensional electrode microbial fuel cell for hydrogen peroxide synthesis coupled to wastewater treatment", Journal of Power Sources **254**, 316–322 (2014).

[13] Du, Z., H. Li and T. Gu, "A state of the art review on microbial fuel cells: A promising technology for wastewater treatment and bioenergy", Biotechnology Advances **25**, 5, 464 – 482 (2007).

[14] Fairweather, A., M. Foster and D. Stone, "Battery parameter identification with pseudo random binary sequence excitation (prbs)", Journal of Power Sources **196**, 22, 9398–9406 (2011).

[15] Friedman, E. S., M. A. Rosenbaum, A. W. Lee, D. A. Lipson, B. R. Land and L. T. Angenent, "A cost-effective and field-ready potentiostat that poises subsurface electrodes to monitor bacterial respiration", Biosensors and Bioelectronics **32**, 1, 309–313 (2012).

[16] Fu, L., S.-J. You, F.-l. Yang, M.-m. Gao, X.-h. Fang and G.-q. Zhang, "Synthesis of hydrogen peroxide in microbial fuel cell", Journal of chemical technology and biotechnology **85**, 5, 715–719 (2010).

[17] Galán, O., J. A. Romagnoli and A. Palazoglu, "Real-time implementation of multi-linear model-based control strategies—an application to a bench-scale pH neutralization reactor", Journal of Process Control **14**, 5, 571 – 579 (2004).

[18] Glover, K. and D. McFarlane, "Robust stabilization of normalized coprime factor plant descriptions with H_∞ bounded uncertainty", Automatic Control, IEEE Transactions on **34**, 8, 821–830 (1989).

[19] Gnoth, S., A. Kuprijanov, R. Simutis and A. Lübbert, "Simple adaptive pH control in bioreactors using gain-scheduling methods", Applied Microbiology and Biotechnology **85**, 4, 955–964 (2009).

[20] Gomez, J. C., A. Jutan and E. Baeyens, "Wiener model identification and predictive control of a pH neutralisation process", IEE Proceedings - Control Theory and Applications **151**, 3, 329–338 (2004).

[21] Goodwin, G. C., S. F. Graebe and M. E. Salgado, "Control system design", Upper Saddle River p. 13 (2001).

[22] Grassi, E. and K. Tsakalis, "PID controller tuning by frequency loop-shaping", in "Decision and Control, 1996., Proceedings of the 35th IEEE Conference on", vol. 4, pp. 4776–4781 (IEEE, 1996).

[23] Grassi, E. and K. Tsakalis, "PID controller tuning by frequency loop-shaping: application to diffusion furnace temperature control", Control Systems Technology, IEEE Transactions on **8**, 5, 842–847 (2000).

[24] Grassi, E., K. S. Tsakalis, S. Dash, S. Gaikwad and G. Stein, "Adaptive/self-tuning PID control by frequency loop-shaping", in "Decision and Control, 2000. Proceedings of the 39th IEEE Conference on", vol. 2, pp. 1099–1101 (IEEE, 2000).

[25] Grassi, E., K. S. Tsakalis, S. Dash, S. V. Gaikwad, W. MacArthur and G. Stein, "Integrated system identification and PID controller tuning by frequency loop-shaping", IEEE Transactions on Control Systems Technology **9**, 2, 285–294 (2001).

[26] Gustafsson, T. K. and K. V. Waller, "Dynamic modeling and reaction invariant control of pH", Chemical Engineering Science **38**, 3, 389 – 398 (1983).

[27] Harris, S. and D. Mellichamp, "Controller tuning using optimization to meet multiple closed-loop criteria", AIChE Journal **31**, 3, 484–487 (1985).

[28] Henson, M. A. and D. E. Seborg, "Adaptive nonlinear control of a pH neutralization process", IEEE Transactions on Control Systems Technology **2**, 3, 169–182 (1994).

[29] Hespanha, J., D. Liberzon, A. Stephen Morse, B. Anderson, T. S. Brinsmead and F. De Bruyne, "Multiple model adaptive control. part 2: switching", International journal of robust and nonlinear control **11**, 5, 479–496 (2001).

[30] Hespanha, J. and A. S. Morse, "Supervision of families of nonlinear controllers", in "Proceedings of 35th IEEE Conference on Decision and Control", vol. 4, pp. 3772–3773 vol.4 (1996).

[31] Ioannou, P. A. and J. Sun, *Robust adaptive control* (Courier Corporation, 2012).

[32] Joshi, R., K. Tsakalis, J. MacArthur and S. Dash, "Account for uncertainty with robust control design: Part 1", Chemical Engineering Progress **110**, 11, 31–38 (2014).

[33] Joshi, R., K. Tsakalis, J. MacArthur and S. Dash, "Account for uncertainty with robust control design part 2", Chemical Engineering Progress **110**, 12, 46–50 (2014).

[34] Kulkarni, B. D., S. S. Tambe, N. V. Shukla and P. B. Deshpande, "Nonlinear pH control", Chemical Engineering Science **46**, 4, 995 – 1003 (1991).

[35] Landau, I. D. and G. Zito, *Digital control systems: design, identification and implementation* (Springer Science & Business Media, 2005).

[36] Liu, H., S. Cheng and B. E. Logan, "Production of electricity from acetate or butyrate using a single-chamber microbial fuel cell", Environmental science & technology **39**, 2, 658–662 (2005).

[37] Liu, H. and B. E. Logan, "Electricity generation using an air-cathode single chamber microbial fuel cell in the presence and absence of a proton exchange membrane", Environmental science & technology **38**, 14, 4040–4046 (2004).

[38] Liu, H., R. Ramnarayanan and B. E. Logan, "Production of electricity during wastewater treatment using a single chamber microbial fuel cell", Environmental science & technology **38**, 7, 2281–2285 (2004).

[39] Logan, B. E., B. Hamelers, R. Rozendal, U. Schröder, J. Keller, S. Freguia, P. Aelterman, W. Verstraete and K. Rabaey, "Microbial fuel cells: methodology and technology", Environmental Science & Technology **40**, 17, 5181–5192 (2006).

[40] Lusk, B. G., P. Parameswaran, S. C. Popat, B. E. Rittmann and C. I. Torres, "The effect of pH and buffer concentration on anode biofilms of thermincola ferriacetica", Bioelectrochemistry **112**, 47–52 (2016).

[41] Marcus, A. K., C. I. Torres and B. E. Rittmann, "Analysis of a microbial electrochemical cell using the proton condition in biofilm (PCBIOFILM) model", Bioresource Technology **102**, 1, 253 – 262, special Issue: Biofuels - II: Algal Biofuels and Microbial Fuel Cells (2011).

[42] McAvoy, T. J., E. Hsu and S. Lowenthal, "Dynamics of pH in controlled stirred tank reactor", Industrial & Engineering Chemistry Process Design and Development **11**, 1, 68–70 (1972).

[43] McCarty, P. L., J. Bae and J. Kim, "Domestic wastewater treatment as a net energy producer–can this be achieved?", Environmental Science & Technology **45**, 17, 7100–7106, pMID: 21749111 (2011).

[44] Modin, O. and K. Fukushi, "Production of high concentrations of H_2O_2 in a bioelectrochemical reactor fed with real municipal wastewater", Environmental technology **34**, 19, 2737–2742 (2013).

[45] Nishikawa, Y., N. Sannomiya, T. Ohta and H. Tanaka, "A method for auto-tuning of PID control parameters", Automatica **20**, 3, 321–332 (1984).

[46] Pandiaraj, M., A. R. Benjamin, T. Madasamy, K. Vairamani, A. Arya, N. K. Sethy, K. Bhargava and C. Karunakaran, "A cost-effective volume miniaturized and microcontroller based cytochrome c assay", Sensors and Actuators A: Physical **220**, 290–297 (2014).

[47] Peymani, E., A. Fatehi, P. Bashivan and A. K. Sedigh, "An experimental comparison of adaptive controllers on a pH neutralization pilot plant", in "India Conference, 2008. INDICON 2008. Annual IEEE", vol. 2, pp. 377–382 (2008).

[48] Popat, S. C., D. Ki, M. N. Young, B. E. Rittmann and C. I. Torres, "Buffer pK_a and transport govern the concentration overpotential in electrochemical oxygen reduction at neutral pH", ChemElectroChem **1**, 11, 1909–1915 (2014).

[49] Puig, S., M. Serra, M. Coma, M. Cabré, M. D. Balaguer and J. Colprim, "Effect of pH on nutrient dynamics and electricity production using microbial fuel cells", Bioresource Technology **101**, 24, 9594 – 9599 (2010).

[50] Rivera, D. E., M. Morari and S. Skogestad, "Internal model control: PID controller design", Industrial and engineering chemistry process design and development **25**, 1, 252–265 (1986).

[51] Rozendal, R. A., E. Leone, J. Keller and K. Rabaey, "Efficient hydrogen peroxide generation from organic matter in a bioelectrochemical system", Electrochemistry Communications **11**, 9, 1752–1755 (2009).

[52] Ruiz, Y., J. A. Baeza and A. Guisasola, "Enhanced performance of bioelectrochemical hydrogen production using a pH control strategy", ChemSusChem **8**, 2, 389–397 (2015).

[53] Sajjanshetty, K. S. and M. G. Safonov, "Unfalsified adaptive control: Multi-objective cost-detectable cost functions", in "53rd IEEE Conference on Decision and Control", pp. 1283–1288 (2014).

[54] Sastry, S. and M. Bodson, *Adaptive Control: Stability, Convergence and Robustness*, Dover Books on Electrical Engineering Series (Dover Publications, 2011).

[55] Shafique, A. B., R. Joshi and K. Tsakalis, "Control relevant system identification using multiple short data sets", in "2017 IEEE Conference on Control Technology and Applications (CCTA)", pp. 1728–1733 (2017).

[56] Shafique, A. B. and K. Tsakalis, "Discrete-time PID controller tuning using frequency loop-shaping", in "Advances in PID Control", vol. 2, pp. 613–618 (2012).

[57] Söderström, T. and P. Stoica, *System identification* (Prentice-Hall, Inc., 1988).

[58] Stefanovic, M. and M. G. Safonov, "Safe adaptive switching control: Stability and convergence", IEEE Transactions on Automatic Control **53**, 9, 2012–2021 (2008).

[59] Tan, C., H. Yang and G. Tao, "A multiple-model MRAC scheme for multivariable systems with matching uncertainties", Information Sciences **360**, Supplement C, 217 – 230 (2016).

[60] Torres, C. I., A. Kato Marcus and B. E. Rittmann, "Proton transport inside the biofilm limits electrical current generation by anode-respiring bacteria", Biotechnology and Bioengineering **100**, 5, 872–881 (2008).

[61] Tsakalis, K. and S. Dash, "Multivariable controller performance monitoring using robust stability conditions", Journal of Process Control **17**, 9, 702–714 (2007).

[62] Tsakalis, K., S. Dash, A. Green and W. MacArthur, "Loop-shaping controller design from input-output data: application to a paper machine simulator", Control Systems Technology, IEEE Transactions on **10**, 1, 127–136 (2002).

[63] Tsakalis, K. and K. Stoddard, "Integrated identification and control for diffusion/cvd furnaces", in "Emerging Technologies and Factory Automation Proceedings, 1997. ETFA'97., 1997 6th International Conference on", pp. 514–519 (IEEE, 1997).

[64] Tsakalis, K. and K. Stoddard, "Control oriented uncertainty estimation in system identification", in "17th IASTED Int. Conf. MIC, Grindelwald, Switzerland", (1998).

[65] Tsakalis, K. S., "Performance limitations of adaptive parameter estimation and system identification algorithms in the absence of excitation", Automatica **32**, 4, 549 – 560 (1996).

[66] Tsakalis, K. S. and S. Dash, "Identification for PID control", in "PID Control in the Third Millennium", pp. 283–317 (Springer London, 2012).

[67] Tsakalis, K. S. and S. Dash, "Approximate H_∞ loop shaping in pid parameter adaptation", International Journal of Adaptive Control and Signal Processing **27**, 1-2, 136–152 (2013).

[68] Voda, A. and I. Landau, "A method for the auto-calibration of PID controllers", Automatica **31**, 1, 41–53 (1995).

[69] You, S. J., Q. L. Zhao, J. Jiang, J. Zhang and S. Q. Zhao, "Sustainable approach for leachate treatment: electricity generation in microbial fuel cell.", Journal of environmental science and health. Part A, Toxic/hazardous substances & environmental engineering **41 12**, 2721–34 (2006).

[70] Young, M. N., A. K. Marcus and B. E. Rittmann, "A combined activated sludge anaerobic digestion model (CASADM) to understand the role of anaerobic sludge recycling in wastewater treatment plant performance", Bioresource technology **136**, 196–204 (2013).

[71] Zhan, C. Q. and K. Tsakalis, "System identification for robust control", in "American Control Conference, 2007. ACC'07", pp. 846–851 (IEEE, 2007).

[72] Zhou, K., J. C. Doyle, K. Glover *et al.*, *Robust and optimal control*, vol. 40 (Prentice hall New Jersey, 1996).

APPENDIX A

DERIVATION OF A RSC METRIC

This chapter discusses derivation of a RSC metric we used in the formulation of adaptive pH control.

Let G be the plant to be controlled by the controller C. The FLS algorithm objective is to find the controller C that minimizes distance between in loop transfer function GC and the target loop L. One way of repenting distance between GC and L is using RSC metric and the derivation of RSC metric with the use of small gain theorem is shown below.

Consider, a block diagram of the closed-loop system as shown in Fig. A.1. It can be rearranged into the block diagram shown in Fig. A.1(b). Reduction of the block diagram in Fig. A.1(b) into the block diagram convenient for the application of small gain theorem is shown in Fig. A.1(c).

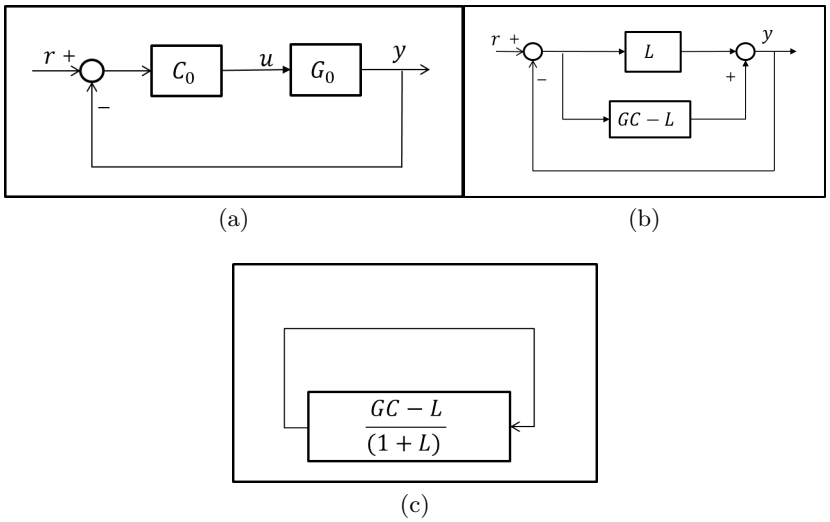

Figure A.1: Block diagrams of the closed-loop system

If $\frac{(GC-L)}{1+L}$ is stable, then the small gain theorem condition for the closed loop system described using the block diagram in Fig. A.1(c) is as follows.

$$\left\| \frac{(GC-L)}{1+L} \right\|_\infty < 1. \tag{A.1}$$

We call the left side of Eq. A.1 a RSC metric. The RSC term can be further simplified into the following equation.

$$RSC = \left\| S(CG - L) \right\|_\infty . \tag{A.2}$$

Where $S = 1/(1 + L)$ is target sensitivity.